MODULATION OF AVIAN IRIDESCENCE VIA MELANOGENESIS

Soraia Barbosa[1,2,†,*], Carina Bittner[3†], Roberto Arbore[1,2,4†], Pedro M. Araújo[1,2,5†], Paulo Pereira[1,2], Pedro Andrade[1,2], Csaba Fekete[6], Rita Afonso[1,2,7], Sandra Afonso[1,2], Maria F. Amorim[1,2,7], Cristiana I. Marques[1,2,7], Michaël P. J. Nicolaï[8], João Carita[9], Jindřich Brejcha[10], Ricardo J. Lopes[11], Joel M. Alves[1,2,12], Fernando Cruz[13,14], Jèssica Gómez-Garrido[13,14], Cristina Zamarreño[13,15], Marta Gut[13,14], Tyler Alioto[13,14], Muhammad Akhtar Ali[16,17], Andrea Hilpert[18], Anita Hech[18], Erdmann Spiecker[19,20], Benjamin Apeleo Zubiri[19,20], Shosuke Ito[21], Kazumasa Wakamatsu[21], Leif Andersson[16,22], Joseph C. Corbo[4], Nicolas Vogel[3,‡,*], Miguel Carneiro[1,2,‡,*]

[1]CIBIO, Centro de Investigação em Biodiversidade e Recursos Genéticos, InBIO Laboratório Associado, Universidade do Porto, Vairão, Portugal
[2]BIOPOLIS Program in Genomics, Biodiversity and Land Planning, CIBIO, Vairão, Portugal
[3]Institute of Particle Technology, Friedrich-Alexander-University Erlangen-Nürnberg, Erlangen, Germany
[4]Department of Pathology and Immunology, Washington University School of Medicine, St. Louis, MO, USA
[5]CFE – Centre for Functional Ecology: Science for People & Planet, Marine Resources, Conservation and Technology, Department of Life Sciences, Coimbra, Portugal
[6]Laboratory of Integrative Neuroendocrinology, HUN-REN Institute of Experimental Medicine, Budapest, Hungary
[7]Departamento de Biologia, Faculdade de Ciências da Universidade do Porto, Porto, Portugal
[8]Evolution and Optics of Nanostructures Group, Biology Department, Ghent University, Ghent, Belgium.
[9]Instituto de Tecnologia Química e Biológica António Xavier, Universidade Nova de Lisboa, Lisboa, Portugal
[10]Department of Philosophy and History of Science, Faculty of Science, Charles University in Prague, Praha, Czech Republic
[11]CE3C, Center for Ecology, Evolution and Environmental Change & CHANGE, Global Change and Sustainability Institute, Departamento de Biologia, Faculdade de Ciências, Universidade de Lisboa, 1749-016 Lisboa, Portugal
[12]Palaeogenomics and Bio-Archaeology Research Network, School of Archaeology, University of Oxford, Oxford, OX1 3QY, United Kingdom
[13]Centro Nacional de Análisis Genómico (CNAG), Baldiri Reixac 4, 08028 Barcelona, Spain
[14]Universitat de Barcelona (UB), Barcelona, Spain
[15]Universitat Autónoma de Barcelona (UAB), 08193 Bellaterra (Cerdanyola del Vallès), Barcelona, Spain
[16]Department of Medical Biochemistry and Microbiology, Uppsala University, Uppsala, Sweden
[17]School of Biological Sciences, University of the Punjab, Lahore, Pakistan
[18]Friedrich-Alexander-Universität Erlangen-Nürnberg, Institut für Mikroskopische Anatomie und Molekulare Bildgebung
[19]Friedrich-Alexander-Universität Erlangen-Nürnberg, Department of Materials Science & Engineering, Institute of Micro- and Nanostructure Research (IMN)
[20]Center for Nanoanalysis and Electron Microscopy (CENEM), IZNF, 91058 Erlangen, Germany
[21]Institute for Melanin Chemistry, Fujita Health University, Toyoake, Aichi, Japan
[22]Department of Veterinary Integrative Biosciences, Texas A&M University, College Station, TX, USA
[†]Co-first authors
[‡]Co-senior authors

***Correspondence**: miguel.carneiro@cibio.up.pt (M.C.), nicolas.vogel@fau.de (N.V.); soraiabarbosa@cibio.up.pt (S.B.)

Keywords: structural coloration, feather nanostructures, melanosomes, single-cell transcriptomics, photonic materials

Classification: Biological Sciences/Evolution; Physical Sciences/Biophysics and Computational Biology

Abstract

The iridescent colors of birds originate in nanoscale feather structures that interact with light. Although the physical principles governing avian iridescence are well-established, the molecular mechanisms assembling these nanostructures into photonic materials remain unknown. Here, we integrated genomic, cellular, and optical approaches to investigate the molecular basis of iridescent color formation in birds. We leveraged mutations that arose in the domesticated Indian peafowl and natural color variation in wild birds. In peafowl, we identified eight genes underlying gains, losses, and shifts of iridescence, whereas in two wild species, we used single-cell transcriptomics to profile asymmetric feathers in which iridescent and non-iridescent barbules develop on opposite sides of the same feather. We found that all peafowl mutations mapped to melanogenesis genes, showing that variation in this pathway can modify diverse geometric features of feather photonic nanostructures. Mutations altering melanin composition collapsed multilayered photonic systems and yielded non-iridescent tissues, whereas changes in melanosome abundance, elongation, or deposition timing generated multilayer architectures with variable periodicity and color. We further show in peafowl that transitions from non-iridescent to iridescent plumage were associated with single-nucleotide mutations in a melanogenesis gene, suggesting that, in species already capable of forming multilayered nanostructures, iridescence can be gained by relatively small genetic changes. Single-cell transcriptomes from wild species also supported extensive melanocyte-centered regulatory rewiring associated with iridescence, including changes in melanosome maturation, trafficking, and intercellular signaling. Together, these results show that the nanoscale order underlying iridescence is developmentally plastic and highly responsive to the melanogenic environment.

Significance Statement

Bird feathers can produce brilliant, shifting colors, but how these colors form during development has remained poorly understood. By comparing the genomes of color variants of domesticated peafowl and transcriptomes during feather development in wild birds, and combining these with chemical and optical analyses, we show that mutations in genes associated with melanogenesis can profoundly alter the amount, shape, and arrangement of the melanin granules inside feathers that interact with light and produce iridescence. These changes can switch feather appearance between dull and iridescent, or generate entirely new colors by restructuring how those granules are layered at the microscopic scale. Our results reveal a direct and flexible link between pigment production and the physical structures that generate iridescence in birds.

Introduction

From butterfly wings to bird feathers, animal coloration arises through two primary mechanisms: pigmentary and structural coloration (1–4). In birds, pigments generate hues ranging from blacks and browns to bright reds and yellows (5–9), and their genetic and biochemical underpinnings are increasingly well understood (*6–9*). However, some of the most visually striking feather effects—glossy blacks, bright blues, and iridescence—result from structural coloration (10–12). This form of coloration originates from the interaction of light with highly organized nanoscale features within feathers (10, 13), and evolves more rapidly than pigment-based colors (14–19). Notable examples include the elaborate plumage of hummingbirds and peacocks, whose eyespot feathers have become textbook examples of sexual selection. Structural colors are crucial to avian biology, supporting functions such as communication and camouflage (10, 20, 21), and serve as models for bioinspired technologies (22–24).

Iridescence in bird feathers is a form of structural coloration that produces brilliant colors that vary with the angle of observation or illumination (10, 25). Avian iridescence arises from multilayer nanostructures consisting of keratin and melanosome layers within feather barbules. Melanosomes are intracellular organelles produced by pigment cells (melanocytes) that synthesize and store melanin, and can vary in shape and internal structure, including rod- or platelet-shaped melanosomes, which can be either solid or hollow (10, 25–28). For example, many hummingbirds possess hollow melanosomes, sometimes with a platelet-like morphology,

whereas platelet-shaped melanosomes are also found in some starlings and birds-of-paradise. Here, we focus on the most widespread mechanism of avian iridescence, exemplified in peacock feathers, where high-refractive-index rod-shaped and solid melanosomes are embedded within a lower-refractive-index matrix of keratin and air (29–31). During feather growth, these components become organized into highly ordered multilayered nanostructures that reflect light through constructive interference (when reflected light waves reinforce one another), producing iridescent colors (4, 10, 25, 32). Variation in melanosome morphology and arrangement, as well as barbule geometry, accounts for much of the nanostructural and optical diversity of iridescent plumage (15, 25, 27, 29, 30, 33). Despite decades of optical and anatomical work clarifying the physical basis of avian iridescence, the developmental and molecular mechanisms that generate these nanostructures remain essentially unknown (2, 11). Although physicochemical self-assembly is thought to play an important role in their formation (26), the extent to which their assembly is also shaped by direct cellular patterning or other developmental processes remains unclear.

In this study, we investigated the molecular basis of avian iridescence using complementary systems and approaches. First, we studied eight color variants of the domesticated Indian peafowl (*Pavo cristatus*), in which Mendelian mutations cause losses and shifts in iridescence across the whole body, including the eyespot (**Fig. 1**; **fig. S1**). These color varieties, each a single mutational step from wild-type, offer a powerful system to link genotype, nanostructure, and optical phenotype. By combining genetic mapping, pigment chemistry, ultrastructural analyses, and optical measurements, we linked these mutations to changes in feather photonic nanostructures. We then examined the Black-shoulder mutation, another domesticated variant that confers a localized gain of iridescent coloration in males, which shows that minimal genetic changes in melanogenic genes can generate new photonic structures with iridescent color. Finally, to determine whether similar mechanisms operate in nature, we profiled asymmetric feathers from wild birds using single-cell transcriptomics, comparing iridescent and non-iridescent barbules developing within the same feather. Complementing the mutational insights provided by the peafowl system, these wild-bird analyses reveal how iridescent coloration is generated through the integration of multiple developmental processes, including melanogenesis, keratinization, and intercellular signaling. Our study provides molecular insights into the generation of iridescent colors of bird feathers, a phenomenon that is better understood from physical and anatomical perspectives.

RESULTS

Peafowl color variation maps to melanogenesis genes

Our current understanding of the anatomical organization of photonic structures in avian feathers provides a framework to hypothesize mechanisms through which structural coloration might evolve in birds. Modifications in melanin biosynthesis, keratin production, feather morphogenesis, or spatial signaling pathways that coordinate intracellular organization are all potential mechanisms that might affect the resultant plumage color (11, 34). However, progress in testing these hypotheses has been limited because iridescent traits rarely segregate within species, restricting the discovery of functionally relevant genetic variants (35, 36). Domesticated color mutants of the Indian peafowl offer a rare opportunity to directly interrogate the molecular determinants of structural coloration.

To investigate the molecular basis of color variation in peafowl, we began by generating a *de novo* reference genome (**table S1; figs. S2 and S3**). Using long-read Nanopore sequencing, 10x Genomics linked-reads, and Hi-C chromatin conformation capture data, we assembled a chromosome-scale genome (1.04 Gb, N50 = 93.07 Mb) with 96.2% completeness of single-copy avian orthologs. Gene annotation, assisted by transcriptome data from five tissues, identified 21,618 protein-coding genes. We further resequenced the genomes of 368 birds representing wild-type, color mutants known to be governed by single Mendelian loci, and color varieties likely arising from combinations of two or more mutations (mean depth = 10.1× ± 5.3 SD). For a subset of individuals representing wild-type and several mutant varieties (n = 27), we profiled gene expression in regenerating feather follicles using RNA-sequencing.

Genome-wide association studies (GWAS) recovered significant loci for eight Mendelian peafowl varieties (**Fig. 2A**), thus genetically characterizing the domesticated variants analyzed below for their ultrastructural, cellular, biochemical, and optical phenotypes. Each significant locus contained a strong candidate gene involved in melanosome biology, indicated in brackets below. Three of these varieties had lead variants on the Z chromosome (Cameo, Purple, and Violet), consistent with inheritance patterns observed by breeders. The eight genetically characterized varieties included White (*EDNRB2*), Ultramarine (*MITF*),

Cameo (*AP3S1*), Bronze (*HPS3*), Opal (*MLPH*), Charcoal (*LYST*), and Purple and Violet (*TYRP1*), whose candidate genes span diverse steps of the melanogenic pathway, including melanoblast differentiation, regulation of melanogenesis, melanosome biogenesis and trafficking, melanosome transfer to keratinocytes, and melanin biosynthesis (**Fig. 2B**).

Within each candidate region, we identified putative causal variants, including missense substitutions, premature stop codons, and exon deletions (**table S2**). In several cases, their functional relevance was supported by expression data or their overlap with evolutionarily conserved amino acid positions across avian species (**fig. S4**; **table S2**). Genotyping across our full cohort of samples revealed that four additional peafowl varieties result from combinations of these mutations (**table S2**), illustrating how epistatic interactions further expand color diversity. Collectively, these results show that variation in melanogenesis genes is associated with a wide range of effects on iridescent color phenotypes in bird feathers, and establish a basis for linking specific mutations to feather nanostructure and optical phenotype.

Photonic lattice geometry is highly sensitive to changes in melanogenesis

Next, we hypothesized that genetic variation in peafowl influences feather coloration by altering the organization of photonic nanostructures. To test this, we sampled six chromatic zones of the peacock eyespot (A1-A6; **Fig. 3A**) (27, 30, 37), and examined cross-sectional and longitudinal preparations of barbules from wild-type and the genetically characterized varieties using transmission electron microscopy (TEM). We quantified seven structural parameters that collectively describe the nanostructural organization of the barbule photonic lattice, encompassing melanosome geometry, air pocket dimensions, and lattice organization (**Fig. 3A; fig S5; table S3**). We related ultrastructural features to optics via angle-dependent reflectance spectroscopy, which measures how feather color changes when viewed or illuminated from different angles.

TEM imaging of wild-type feathers revealed that rod-shaped melanosomes formed a highly ordered photonic lattice, with their long axes aligned parallel to the barbule, with variation in layer spacing and number generating the distinct hues across the eyespot (**Fig. 3A; fig. S5**), as previously documented (27, 29, 37). In contrast, color mutants exhibited pronounced deviations from the wild-type ultrastructure (**Fig. 3A-C; figs. S5 and S6**), and we applied linear discriminant analysis (LDA), a statistical approach that identifies which variables best distinguish among groups, to determine which features most strongly contribute to these differences (**Fig. 3D; tables S4 and S5)**. This analysis revealed a clear separation between two main clusters along the first discriminant axis (LD1), which accounted for 90% of total variance (**Fig. 3D**). Melanosome length was the strongest contributor (*Lm*, $P = 6.1\times10^{-37}$) (**table S4**), which was inversely correlated with melanosome diameter (*Dm*) ($r = -0.76$), together defining the melanosome aspect ratio (rod-like versus spherical). Bronze, Cameo, and Charcoal mutants clustered on the negative LD1 axis, and TEM images revealed a collapse of the photonic lattice, with spherical and poorly ordered or disordered melanosomes replacing the aligned rods typical of wild-type iridescent feathers (**Fig. 3B and C; figs. S5 and S6**). Their reflectance spectra—measurements of the wavelengths of light reflected by the feather—were flat or displayed weak features (**Fig. 3C; fig. S7**), indicating a loss of constructive interference. Our results thus reveal a gradient among peafowl mutants in which progressive melanosome rounding or irregularity corresponds to increasing lattice disorder (strongly iridescent types < Bronze < Cameo < Charcoal) (**Fig. 3B and C**; **table S5**).

The Opal variety exhibited a partially ordered lattice with fewer layers, yielding weaker iridescence (**Fig. 3B and C; figs. S5-S7**). Violet, Purple, and Ultramarine mutants retained well-organized multilayered lattices (**Fig. 3C**; **fig. S5**) and clustered close to wild-type (**Fig. 3D**). Within this iridescent group, LD1 (62.8% of variance) was driven by melanosome diameter (*Dm*; $r = 0.94$, $P = 1.2 \times 10^{-14}$), with additional contributions from inter-melanosome spacing (*b*; $r = 0.54$, $P = 0.002$) and inter-layer distance (*a*; $r = 0.38$, $P = 0.04$) (**Fig. 3D**; **table S4**). LD2 (25.2% of variance) was shaped mainly by layer number (*N*; $r = 0.81$, $P = 7.3 \times 10^{-8}$). Comparative analyses relative to wild-type highlighted the phenotype-specific shifts (**table S5**). Opal differed most strongly in layer number (*N*; $P = 1.1 \times 10^{-4}$), whereas Purple and Violet diverged mainly in melanosome diameter (*Dm*; $P = 2.8 \times 10^{-6}$) and in inter-melanosome spacing within layers (*b*; $P < 3.0 \times 10^{-2}$). Ultramarine showed differences only in inter-melanosomal spacing (*b*; $P = 2.0 \times 10^{-2}$). The number of layers (*N*) also differed significantly in Violet ($P = 4.4 \times 10^{-2}$) and, although not significant overall, exhibited pronounced regional variation in Purple and Ultramarine (**figs. S5 and S6**).

These ultrastructural changes were closely associated with optical variation. A blue shift in peak reflectance from Purple to Violet to Ultramarine (**fig. S7**) is associated with decreasing inter-melanosome

spacing within layers, which shortens the optical path and shifts constructive interference toward shorter wavelengths. Across chromatic zones and iridescent varieties, layer number (N) was positively associated with color saturation (84%; $t = 5.7$, $df = 94$; $P = 1.3 \times 10^{-7}$), consistent with enhanced constructive interference in barbules with more layers (**fig. S8**). Thus, repetition (layer number) and periodicity (melanosome spacing) are tunable features of photonic lattices that vary predictably with mutations in melanogenesis genes and are associated with differences in hue, saturation, and spectral bandwidth in iridescent plumage. Our findings also reveal a continuum of nanostructural integrity among peafowl color variants, in which some mutations are associated with pronounced disruption of lattice organization, whereas others are associated with subtler changes in lattice geometry and color.

Cellular and biochemical basis of iridescence

Because the candidate genes identified in peafowl are associated with melanogenesis, we next investigated how these mutations affect melanin production and other melanogenesis-related cellular processes underlying iridescent feather development. To determine how such changes shape feather nanostructure, we analyzed regenerating feather follicles and mature neck feathers from wild-type and mutant birds. Longitudinal follicle sections were examined by light microscopy to assess melanin distribution in melanocyte and keratinocyte layers, as well as the melanocyte dendritic branching (**Fig. 4A**), which mediates melanosome transfer into keratinocytes that become the feather's structural matrix. In parallel, we performed chemical analysis of mature feathers to evaluate how mutations affect melanin biosynthesis and deposition (**Fig. 4B**; **table S6**). We focused on neck feathers because they can be induced to regenerate by plucking independently of the molting cycle and exhibit uniform coloration, providing a simplified and more tractable system than the complex color patterning of the eyespot and facilitating comparisons of cellular and biochemical phenotypes among varieties.

In wild-type follicles, melanosomes were abundant and efficiently transferred from melanocytes to keratinocytes through dendritic projections, producing a uniform pigment distribution (**Fig. 4A**). Biochemically, wild-type feathers had a high eumelanin-to-pheomelanin ratio (~10:1; **Fig. 4B**). The weakly iridescent (Bronze) and non-iridescent mutants (Cameo and Charcoal) showed diverse cellular and biochemical changes. In Charcoal follicles, dendrites and melanosome transfer were present, but melanosomes formed aggregates within melanocytes and keratinocytes (**Fig. 4A**). Despite appearing visually darkest, Charcoal contained 67% less total melanin than wild-type feathers ($t = 8.4$, $df = 6$, $P = 1.6\times10^{-4}$) and comparable levels to Violet and Purple (**Fig. 4B**), which appear far more vibrant, illustrating a disconnect between pigment abundance and perceived brightness arising from structural organization. Cameo and Bronze displayed disrupted melanin distribution, with clustered pigment deposits within keratinocytes indicating melanosome aggregation (**Fig. 4A**). In Cameo, pigment-free regions within melanocytes suggested the presence of large intracellular vacuoles. Importantly, across all three mutants, eumelanin content was markedly reduced, but the pheomelanin levels remained almost unaltered (**Fig. 4B**), hence reducing the eumelanin-to-pheomelanin ratio (~1.5:1–4:1). These compositional shifts coincided with the transformation of rod-shaped melanosomes into more spherical forms (**Fig. 3B and C**). Although the underlying genes act at distinct steps of melanogenesis, none are known to directly regulate melanosome morphology. The repeated emergence of spherical melanosomes is instead consistent with the possibility that altered melanin composition influences melanosome shape, either directly or by perturbing normal melanosome maturation. These changes in melanosome shape, in turn, were consistently associated with compromised photonic lattice integrity.

The Opal mutant showed a distinct cellular phenotype, characterized by melanocytes densely filled with melanin but lacking visible dendritic projections to keratinocytes, which receive few melanosomes (**Fig. 4A**). This suggests disrupted melanosome transfer. Biochemically, Opal feathers exhibited a large reduction in total melanin (–73%; $t = 11.4$, $df = 7$, $P = 8.9 \times 10^{-6}$; **Fig. 4B**), but unlike Cameo, Bronze, and Charcoal, this decrease affects both eumelanin and pheomelanin (**Fig. 4B**). This more balanced loss appears to preserve the rod-shaped melanosomes typical of wild-type, in contrast to the spherical forms that characterize other low-melanin mutants. Consequently, despite melanin levels comparable to Charcoal, the retention of rod-shaped melanosomes seemingly permits partial nanostructural organization, making Opal appear lighter and more vivid in color.

Hue-shifted iridescent variants (Purple, Violet, and Ultramarine) showed feather follicles with cellular organization comparable to wild-type, with only slight differences (**Fig. 4A**). Purple and Violet follicles contained a higher proportion of light brown melanosomes, indicative of delayed or incomplete maturation as expected from *TYRP1* mutations (38), whereas Ultramarine follicles exhibited dense pigmentation. All three

phenotypes maintained wild-type-like eumelanin-to-pheomelanin ratios (Purple: 9:1; Violet: 8.5:1; Ultramarine: 11.4:1) and retained the characteristic rod-shaped melanosomes (**Fig. 4B**).

Despite these similarities, these mutants fall into two distinct mechanistic categories. Purple and Violet feathers showed large reductions in total melanin content (Purple: –50%, $t = 6.7$, $df = 6$, $P = 5.3 \times 10^{-4}$; Violet: –72%, $t = 9.4$, $df = 6$, $P = 8.5 \times 10^{-5}$) (**Fig. 4B**), yet sufficient to support ordered multilayered structures (**Fig. 3C**). Both mutants also exhibited reduced inter-melanosome spacing (see above). Because *TYRP1* encodes a core enzyme in eumelanin synthesis and contributes to melanosome maturation rather than spatial organization (38), it is unlikely to directly regulate inter-melanosome packing. Instead, the packing changes are most plausibly an indirect consequence of the increased melanosome aspect ratios resulting from reduced melanosome diameter (*Dm*) in both mutants compared to wild-type (**Fig. 3B**). This is consistent with known effects of *TYRP1* on melanosome morphology (39). These observations suggest that variation in melanosome aspect ratio may represent an additional feature of melanogenesis associated with photonic assembly and optical performance. The observed differences between Purple and Violet feathers likely reflect an additional layer of interaction between melanosome abundance and melanosome shape.

In contrast, we found that Ultramarine feathers, likely caused by an *MITF* mutation, showed no significant change in pigment abundance (+0.06%, $t = 4.9 \times 10^{-3}$, $df = 5$, $P = 0.1$) (**Fig. 4B**), despite intense cellular pigmentation in the follicle sections (**Fig. 4A**). Analyses of melanosome morphology and pigment chemistry likewise revealed no detectable differences from wild-type (**Fig. 4B**; **fig. S6**), indicating that pigment quantity or composition cannot account for the observed optical properties. Our ultrastructural data show that the Ultramarine photonic lattice is densely packed, with significantly reduced inter-melanosome distance (*b*) (**Fig. 3C; figs. S5 and S6**). TEM images further indicated a unique organizational anomaly in Ultramarine, which is absent in wild-type and other mutants, consisting of clusters of disorganized melanosomes near the basal boundary of the photonic crystal and occasionally dispersed melanosomes within the medullary region of the barbule (**fig. S9**). The anomaly suggests a developmental mechanism in which photonic lattice assembly was prematurely arrested and melanosomes failed to integrate into the lattice within the appropriate temporal window. A loss of temporal coordination between melanosome delivery and lattice formation could also underlie the observed alterations in periodicity, possibly reflecting melanosome deposition during phases of altered keratin matrix viscosity. This interpretation aligns with several known functions of *MITF*, including its roles in regulating melanocyte differentiation and the timing of melanosome maturation (40).

Taken together, our biochemical, ultrastructural, and photonic analyses indicate that feather nanostructure is a developmentally plastic trait associated with melanosome availability and morphology, as well as with the temporal dynamics of pigment deposition during feather development.

Single mutations in melanogenesis genes can induce iridescent plumage

The Black-shoulder phenotype is another domesticated peafowl variant (41). Unlike the previously described mutations that modify existing iridescent colors throughout the body, Black-shoulder produces a localized gain of iridescence in males within plumage regions that are normally weakly iridescent or non-iridescent. In wild-type peacocks, the shoulders and upper back display a light-dark barred pattern with little iridescence, whereas Black-shoulder males replace this pattern with vivid green and blue plumage (**Fig. 5A**). This mutation also has strikingly sex-specific effects: Black-shoulder females are predominantly depigmented and lack the normal brown body plumage and iridescence, appearing nearly white to pale cream due to pheomelanin deposition (**Fig. 5A**). Thus, the same mutation produces a localized gain of iridescence in males but a reduction in melanin pigmentation and iridescence in females. The male phenotype offers an opportunity to investigate the molecular and developmental basis of the emergence of novel biological photonic structures.

To identify the causal variant, we conducted a GWAS comparing Black-shoulder ($n = 93$) and wild-type birds ($n = 256$, scored for wing color phenotype). This analysis revealed a significant association ($P = 5.0 \times 10^{-28}$) overlapping the *MC1R* gene (**Fig. 5B; fig. S10**), which encodes a receptor that regulates melanin synthesis via the cAMP pathway (42). We next assessed gene expression in regenerating wing covert feather follicles from Black-shoulder ($n = 4$) and wild-type ($n = 6$) males using RNA-seq. *MC1R* expression was similar between phenotypes (**Fig. 5C**), suggesting that functional differences arise from coding changes rather than changes in gene regulation, despite the patch-specific effects. Examination of the *MC1R* coding sequence revealed two mutations: a missense mutation (Trp251Arg and the GWAS lead variant) and a frameshift mutation (**table S2**). Genotyping showed that Black-shoulder males were either homozygous for one mutation

or compound heterozygous, indicating genetic heterogeneity underlying the same phenotype. The frameshift is predicted to disrupt *MC1R* function, whereas the effect of the missense mutation is less certain, although it alters an amino acid residue that is universally conserved among birds and likely to be functionally important (**table S2**). Because both alleles are associated with similar phenotypes, they may alter *MC1R* signaling in a similar manner, although the specific effects remain to be functionally tested. Allelic imbalance tests, which assess whether one gene copy is expressed more strongly than the other in heterozygote birds, showed no expression bias (**Fig. 5C**), reinforcing that the phenotype arises from altered protein function.

To understand the biochemical basis of this gain of iridescence, we analyzed melanin content as above. Chemical analyses of male wing covert feathers showed a ~1.7-fold increase in eumelanin in Black-shoulder relative to the wild-type ($t = 12.3$, $df = 3$, $P = 4.0 \times 10^{-5}$), whereas eumelanin in neck feathers and pheomelanin in either region showed no significant difference ($t < 0.4$, $df = 3\text{-}5$, $P > 0.4$; **Fig. 5D**). In light of what is known about *MC1R* function in mammals (43), this finding of increased eumelanin production in Black-shoulder males may seem surprising. Loss-of-function mutations in *MC1R* or mutations that reduce its activity in mammals are typically associated with red or lighter coat coloration and tend to affect pigmentation broadly across the body rather than in localized regions. This expected behavior is in fact observed in Black-shoulder females, which are lightly colored and retain pheomelanin pigmentation. The striking contrast between peacocks and peahens, therefore, suggests that *MC1R* can interact with sex-specific developmental programs to produce sexually dimorphic effects on pigmentation and iridescence. A growing number of studies in birds have reported similar effects of *MC1R* that differ from the canonical mammalian model (44–46) (see Discussion).

To determine the photonic basis of this gain of iridescence in the wings of Black-shoulder males, we next examined feather ultrastructure. TEM imaging showed organized rod-shaped melanosomes in dark bands of wild-type feathers, but light bands were sparsely pigmented and lacked discernible structure (**Fig. 5E**). In the feathers of male Black-shoulder, in contrast, melanosome density and layering were often increased toward feather tips, and the multilayered organization extended into regions corresponding to the wild-type light bands. Both features show an increase in ordered ultrastructure that underpins the enhanced photonic properties of Black-shoulder feathers (**Fig. 5E**). These findings suggest that increasing melanogenesis and melanin deposition beyond a threshold can trigger the formation of ordered multilayered nanostructures, even in feather barbs previously devoid of such structures. Thus, peafowl, and perhaps other birds, may possess a latent capacity to form photonic nanostructures that can be triggered by changes in the melanogenesis pathway.

Transcriptomic drivers of iridescence in nature

To investigate the developmental basis of naturally occurring iridescence and the formation of its underlying photonic structures, and to determine whether melanocyte-centered processes more broadly contribute to this trait in nature, we performed single-cell RNA sequencing (scRNA-seq) on regenerating feathers of the emerald dove (*Chalcophaps indica*) and mallard duck (*Anas platyrhynchos*). These species represent two additional avian orders and develop asymmetric feathers in their wings, where iridescent and non-iridescent barbules differentiate on opposite sides of the same feather (**Fig. 6A**). This within-feather design enables direct comparisons of cell composition and gene regulation between barbule types within an otherwise identical developmental context. TEM confirmed ordered nanostructures within iridescent barbules and their absence in non-iridescent ones (**Fig. 6A**; **fig. S11**). To identify molecular drivers of these differences, we microdissected regenerating follicles to isolate the sides expressing iridescent and non-iridescent colors and generated eight scRNA-seq libraries (two replicates per barbule type per species).

We identified 31,204 high-quality cells representing all major cell types in growing feathers (**Fig. 6B; figs. S12-15**). Melanocytes formed two transcriptionally distinct clusters corresponding to eumelanin- (melanocytes 1 or ML1) and pheomelanin-producing (melanocytes 2 or ML2) subtypes (see Methods). Using all cell populations, we compared iridescent and non-iridescent barbules to identify differentially expressed genes (DEGs) and differences in cellular composition. In the emerald dove, melanocytes exhibited the most noteworthy changes in both cellular composition and transcriptional profile (**Fig. 6C**). They were threefold more abundant in iridescent barbules (26.7% vs. 8.6%; $P = 1.7 \times 10^{-2}$) and showed the largest number of DEGs. This expression divergence was independent of cell-type abundance and more pronounced within the eumelanin-producing subtype ML1. In mallard, we saw no consistent compositional differences, yet ML1 again showed the largest transcriptional divergence in number of DEGs (**Fig. 6C**). We validated these findings with histological analysis of regenerating feathers and pigment quantification in mature feathers, which

confirmed increased cellular pigmentation and greater melanin deposition in the iridescent side (**Fig. 6A and D**). These results suggest that cellular and transcriptional changes in melanocytes are central to iridescent color development in wild birds, consistent with our findings in peafowl.

Because melanocytes showed the strongest transcriptional divergence, we first focused on their DEGs (**Data S1 and S2**). When the melanocyte subclusters were analyzed either separately or together, only eight genes were shared between both species (*CCZ1*, *CHN1, DCLK1*, *DCX*, *DLC1*, *FTH1*, *GPNMB*, and *NCALD*), indicating that iridescent coloration is produced by distinct gene sets in each lineage despite their convergent nanostructural architecture and optical function. None of the DEGs encoded melanin-synthesis enzymes; instead, expression changes implicated melanocyte signaling, ion homeostasis, melanosome dynamics, and dendritic transfer. In the emerald dove, v-ATPase subunits (*ATP6V1E1*, *ATP6V0A1*), the cation channel *TPCN2*, and the potassium channel *KCNJ13* showed differential expression, consistent with active tuning of melanosome pH and ion balance (processes essential for melanogenesis) in iridescent barbules. In mallard, *cAMP*-responsive effectors downstream of *MC1R* (a DEG in the dove) were elevated (*RAPGEF4* and *ARPP21*), along with trafficking and autophagy regulators (*UVRAG*) and cytoskeletal/adhesion genes involved in dendrite elaboration and vesicle transport (*TMSB4X*, *CHN1*, *KANK1*, *LPP*). Together with increased *GPNMB* and *CCZ1* expression (DEGs shared between both species), these signatures point to more active melanosome maturation and intracellular trafficking as a common feature of iridescent barbule formation. Intercellular signaling also shifted in iridescent feathers and was reflected in gene ontology (GO) enrichment (**fig. S16**): genes associated with GTPase–mediated and ephrin-receptor signaling were elevated in mallard iridescent barbules (*RAPGEF4, CHN1, EPHA7*); WNT-axis components were reduced in both species (*DAAM2* in mallard; *LGR4* in dove); and integrin signaling decreased in dove (*ITGA4*). Three of the genes shared by both species (*CHN1*, *DCLK1*, *DCX*) and several top-10 DEGs (*NBEA*, *VAT1*/*VAT1L*) were linked to neuronal and synaptic processes (GO analyses also confirm an enrichment of many neuron/synapse-related terms; **fig. S16**), raising the hypothesis that synaptic-like vesicular processes contribute to differences in melanosome transfer along melanocyte dendrites between barbule types. These data indicate extensive rewiring of melanocyte biology between iridescent and non-iridescent barbules, while expression of the core enzymatic machinery of melanogenesis remains largely unchanged.

To assess gene regulation beyond melanocytes, we examined DEGs in keratinocytes and mesenchymal cells (**Data S1 and S2**). Many were functionally linked to melanogenesis through their regulatory effects on melanocyte behavior (47, 48), indicating that altered cross-talk between pigment cells and neighboring tissues distinguishes iridescent from non-iridescent barbules. Among the 15 keratinocyte DEGs with well-characterized proteins, six have known connections to melanocyte regulation, including paracrine factors upregulated in iridescent barbules that enhance melanocyte recruitment and proliferation (*KITL* and *NRG1* in mallard) and adhesive molecules mediating keratinocyte-melanocyte communication (*COL17A1* in dove). Mesenchymal cell DEGs likewise showed transcriptional signatures of differential paracrine regulation with secreted factors known to be implicated in melanocyte differentiation, migration, and pigment output, including *NDP* and *BMP2* in dove and *ASIP* and *FST* in mallard. Finally, several DEGs may contribute to iridescence through effects on the keratin matrix and tissue mechanics (11). For example, keratinocyte DEGs included feather structural components encoded by keratin genes that were consistently downregulated in iridescent barbules (*KRT1L*, *KRTβL*, and *KRT6A*). Taken together, our findings suggest that multiple developmental processes contribute to the formation of feather photonic structures in nature, with melanogenesis-associated changes representing one important component (**Fig. 6E**).

Discussion

The formation of iridescent coloration requires an astonishing degree of structural precision. By analyzing nine peafowl color mutations, we connect genetic and biochemical variation to specific macroscopic optical properties. Some mutations produce whole-body losses or shifts in iridescent coloration, whereas Black-shoulder generates a notable, localized gain in iridescence restricted to particular feather tracts in males. Across these phenotypes, we genetically mapped mutations in melanogenesis genes that alter the composition, shape, and organization of photonic nanostructures, producing color shifts ranging from subtle hue differences to complete loss or gain of iridescence. To assess the formation of iridescent coloration in nature, we complemented the analyses of domesticated peacocks with single-cell transcriptomic studies of two wild species with asymmetric feathers, in which iridescent and non-iridescent barbules develop on opposite sides of the same feather. This within-feather comparison is informative because both barbule types develop in the

same feather and therefore share much of their broader developmental context. These comparisons likewise highlighted extensive changes in melanocyte biology associated with iridescence, particularly in pathways related to melanosome maturation, intracellular transport, and communication between melanocytes and neighboring cells. Although other cellular processes can influence feather nanostructures (11, 26, 35, 49)—and our single-cell data in wild species reveal signatures of some of these processes, including expression changes in genes encoding keratins—our findings in domesticated and natural systems suggest that melanogenesis is one important contributor to variation in iridescent color. We propose that melanogenesis may be effective at tuning iridescence because its multistage pathway, governed by dozens to hundreds of interacting factors (43), constitutes a broad mutational target in which even minor perturbations can induce substantial nanostructural and optical shifts, as illustrated by the peafowl mutants.

In contrast to comparative studies in several bird species, our analysis leverages the shallow genetic divergence among peafowl varieties that exhibit cellular, nanostructural, and optical changes arising from single mutational events. The genes identified in mutants that reduce or abolish iridescence, Cameo (*AP3S1*), Bronze (*HPS3*), and Charcoal (*LYST*), span several stages of melanogenesis, including melanosome biogenesis and trafficking, and melanosome maturation. Despite encoding genes with different functions, these mutants were consistently associated with changes in melanin composition, particularly the balance of pheomelanin and eumelanin. Whenever eumelanin declined while pheomelanin remained largely unchanged, the characteristic rod-shaped melanosomes of the wild type were replaced by a more rounded, spherical form, indicating that altered melanin composition may influence melanosome morphology without additional genetic changes directly specifying organelle shape. This observation has been previously described in mammals and other birds (50, 51), where shifts in the eumelanin-to-pheomelanin ratio have also been associated with changes in melanosome shape. In the three peafowl mutants described above, spherical melanosomes were in turn associated with disruption of the photonic lattice and replacement of ordered multilayers by haphazard arrangements that produce black or brown plumage. A useful contrast is provided by the Opal variety, which is controlled by a gene thought to mediate the transport of melanosomes from melanocytes to keratinocytes (*MLPH*). Despite greatly reduced overall pigment levels, Opal feathers exhibit a higher eumelanin-to-pheomelanin ratio that is close to the wild-type, retain rod-shaped melanosomes, and preserve a partially ordered lattice together with residual iridescence. These results suggest that melanosome shape, which is at least in part determined by melanin composition, is an important determinant of photonic ultrastructure organization. This may reflect the fact that rod-shaped melanosomes self-assemble more efficiently into ordered lattice arrangements than spherical ones, possibly through depletion attraction forces, which act more strongly on elongated particles, like rods, to promote their alignment and regular packing. More broadly, the association between melanin composition, melanosome shape, and lattice integrity observed across these single-gene peafowl variants may help explain why pheomelanin-rich feathers rarely display iridescence across birds (11, 25) and suggests that shifts in melanogenesis could lead to the rapid loss of iridescence.

In cases where photonic lattices are preserved, we identified several additional genes in peafowl that modify melanin abundance and produce subtler changes in rod-shaped melanosome morphology. These include *MITF*, a key transcriptional regulator of melanocyte development and melanogenic gene expression, and *TYRP1*, an enzyme involved in eumelanin synthesis. Variation at these loci was associated with shifts in reflected wavelength and color intensity through their effects on lattice periodicity and melanosome stacking, illustrating how changes in melanosome shape, density, and arrangement can shift or generate new iridescent colors without disrupting the lattice itself. Our observations in the Ultramarine variant further raise the possibility that the temporal coordination of melanosome delivery also influences lattice organization. Together, these observations suggest that feather nanoarchitecture is a developmentally plastic trait, shaped by the cellular and biochemical environment rather than strictly specified by fixed genetic programs. In this context, the Black-shoulder mutation that maps to *MC1R* illustrates how changes in melanogenesis, in this case in males alone, can trigger the appearance of iridescent plumage in feather regions that normally show little or no iridescence, suggesting that some birds may possess a latent capacity for gains and shifts in iridescent coloration through changes in melanogenesis. This developmental plasticity is consistent with models in which photonic lattices emerge in part through physicochemical self-organization, where melanosome properties (shape, size, and density) have the potential to bias the outcome of lattice assembly during feather development (26).

This study also has several limitations. First, although our results in peafowl suggest that feather nanoarchitecture is developmentally plastic and responsive to changes in melanogenesis, we did not directly observe the formation of photonic lattices during feather growth. Ultrastructural analyses across successive stages of feather regeneration in both wild-type and mutant backgrounds will therefore be necessary to determine how changes in melanin production, melanosome maturation, and the timing of pigment delivery influence lattice assembly, and to clarify the extent to which direct cellular patterning or other developmental mechanisms also contribute. Second, our conclusions are based on spontaneously occurring genetic variants and correlative comparisons from chemical, to ultrastructural, to optical phenotypes that suggest a strong causality, but that do not provide direct evidence. Direct experimental manipulation, such as feather follicle culture combined with genome editing or virally mediated gene perturbation *in vivo*, offers a means to dissect the contribution of individual genes or pathways to feather formation. Paired with developmental time series and quantitative analyses of lattice assembly, such approaches could reveal how melanogenesis and other molecular processes (e.g., keratinization) shape photonic structure formation during barbule development. Third, the functional and mechanistic effects of the *MC1R* alleles associated with Black-shoulder plumage remain partially unresolved, and further work will be required to determine their effects on melanogenesis. In several birds, the relationship between *MC1R* and melanogenesis appears to be more heterogeneous than the mammalian model would predict, often regulating pigmentation in a spatially restricted manner within individual feathers or body regions (44–46). For example, in turkeys, an *MC1R* allele predicted to strongly impair receptor function causes increased dark pigmentation restricted to the wings rather than generalized pheomelanic plumage (46), closely resembling the peafowl Black-shoulder mutation. In chickens, *MC1R* contributes to the spatial organization of pigmentation within feathers rather than simply to overall melanin production across the body, with local inhibition of *MC1R* by *ASIP* generating alternating dark and light regions within feathers called barring (44), similar to the pattern seen in the wings of wild-type peacocks. In pigeons, the recessive Smoky mutation, caused by a large 500-bp deletion that most likely abolishes *MC1R* function, does not eliminate major eumelanic pattern elements such as the wing and tail bars, indicating that at least some aspects of avian eumelanin production are controlled by *MC1R*-independent pathways (45). The sex-specific and patch-specific effects of Black-shoulder make it a good system for dissecting how *MC1R* function is modified by hormonal and developmental context. Clarifying this will be informative not only for understanding iridescence gain in peacocks but also for understanding how birds regulate melanogenesis more generally. Finally, our study focuses on the most widespread class of avian iridescence, in which rod-shaped melanosomes form multilayered photonic structures. It therefore remains unclear to what extent similar melanogenesis-associated mechanisms, and the same degree of developmental plasticity, also contribute to other forms of iridescent coloration based on hollow or platelet-shaped melanosomes.

METHOD DETAILS

Ethics statement

All experimental procedures involving animals were carried out in compliance with Directive 2010/63/EU on the protection of animals used for scientific purposes. These procedures were reviewed and approved by the Animal Welfare and Ethics Committee of CIBIO/BIOPOLIS (approval reference: 2018_01 and 2019_03).

Genome sequencing of the Indian peafowl

Sampling and DNA isolation. A draft reference genome sequence of the Indian peafowl (*Pavo cristatus*) was generated from a phenotypically wild-type male. Whole blood was collected using a sterile needle and transferred into a heparin-free capillary. The sample was snap-frozen in liquid nitrogen and stored at -80°C until DNA extraction. High-molecular-weight genomic DNA was isolated from 5 µl of blood using a modified salt-based protocol (52), followed by a purification step using AMPure XP magnetic beads (Beckman Coulter) at a 3× beads-to-sample ratio. DNA quantity, purity, and integrity were assessed with a NanoDrop spectrophotometer, a Qubit dsDNA BR Assay Kit (ThermoFisher Scientific), and Agilent Genomic DNA ScreenTape (Agilent).

Nanopore long-read sequencing. Sequencing libraries were prepared using the Oxford Nanopore Technologies (ONT) 1D Sequencing Kit (SQK-LSK109). Briefly, 1.0 µg of high-molecular-weight genomic DNA underwent DNA repair and end-repair using the NEBNext FFPE DNA Repair Mix (NEB) and the NEBNext UltraII End Repair/dA-Tailing Module (NEB). Sequencing adaptors were ligated, and the libraries were purified using 0.4× AMPure XP Beads (Beckman Coulter) and eluted in the provided buffer (SQK-LSK109). Sequencing was performed on a GridION Mk1 (ONT) using R9.4.1 FLO-MIN106D flow cells, with data collected over 72 hours. Run quality parameters were monitored in real time using MinKNOW (v4.2.5).

Data from eight flow cells were base-called using *Guppy* (v3.2.6+afc8e14 for seven flow cells; v3.2.10+aabd4ec for one flow cell). Reads were filtered to remove those with: (1) an average Phred quality score ≤7; (2) lengths <1 kb; (3) low complexity sequences exceeding 40%; or (4) matches to the control sequence (lambda phage, 3.5 kb). Additionally, contamination was assessed using *Kraken* (v0.10.5-beta) (53), and reads matching *Spirometra erinaceieuropaei*, Human gammaherpesvirus-4, cloning vector pCA-DEST2303, or *Mycoplasma hyorhinis* (the four contributing to ~0.01% of reads) were excluded. After filtering, 4,599,390 ONT reads totaling 43.2 Gb (33× coverage) with an N50 of 16.6 kb were retained for downstream analysis.

Linked-read sequencing. The linked-read library was prepared using a Chromium Controller (10x Genomics) and the Genome Reagent Kits v2 (10x Genomics), following the manufacturer's protocol. In brief, 10 ng of high-molecular-weight genomic DNA was partitioned in GEM (Gel Bead-in-Emulsion) reactions containing unique barcodes (Gemcode) and loaded onto a Chromium controller chip. The droplets were recovered, isothermally incubated, and fractured. The intermediate DNA library was then purified and size-selected using Silane and Solid Phase reverse immobilization (SPRI) beads. An Illumina-compatible paired-end sequencing library was prepared following 10x Genomics recommendations and validated using an Agilent 2100 BioAnalyzer with the DNA 7500 assay (Agilent). Sequencing was performed on an Illumina NovaSeq 6000 platform using paired-end reads (2 × 151 bp).

The resulting reads were preprocessed for scaffolding using *LongRanger Basic* (v2.2.2), which performed basic read and barcode processing, including read trimming (removing the first 16 base pairs of read one if they match a valid barcode), barcode error correction, barcode whitelisting, and attaching barcodes to read IDs (producing barcoded reads). Additionally, the original linked read data was processed for use as a standard paired-end library during assembly. All reads were filtered for contaminants by mapping with *gem-mapper* (54) (allowing up to 2% mismatches) against a contamination database that included phiX, UniVec sequences, *E. coli*, the complete mitochondrial sequence of Indian peafowl (NC_024533.1), and the four contaminants detected with *Kraken* (as described above). A total of 262,153,402 paired reads, corresponding to 78.6 Gb (~60× coverage), successfully passed the quality filters and were used for genome assembly.

Chromatin conformation capture sequencing (Hi-C). A Hi-C library was prepared using the Arima High Coverage Hi-C kit (Arima Genomics), following the manufacturer's instructions. Sequencing was performed on an Illumina HiSeq 4000 platform using paired-end reads (2 × 151 bp). A total of 317,826,943 pairs of reads

were aligned against the draft assembly using *Juicer* (v1.6) (55). This process yielded 261,213,953 Hi-C contacts, which were used for subsequent scaffolding.

Contig construction and scaffolding. The Indian peafowl reference genome sequence was assembled using a combination of data sources and multiple iterative steps.

1. Hybrid assembly:
   A hybrid genome assembly was generated with *MaSuRCA* (v3.4.1) (56, 57), using the Illumina linked-read data (60× coverage, treated as paired-end reads) and the pre-processed Nanopore reads (33× coverage) to create mega-reads. These mega-reads were assembled with *Flye* (v2.5) (58). Default parameters were used in *MaSuRCA*, with adjustments to the following settings: USE_LINKING_MATES = 0, MEGA_READS_PASS=0, JF_SIZE = 26200000000, and FLYE_ASSEMBLY=1.
2. Correction and scaffolding with linked reads:
   Barcoded 10x linked reads were used to correct and scaffold the assembly. Misassemblies were identified and resolved with *Tigmint* (v1.1.2) (59), followed by scaffolding with *ARKS* (v1.0.3) (60) and *LINKS* (v1.8.5) (61), as per a published pipeline (http://protocols.faircloth-lab.org/en/latest/protocols-computer/assembly/assembly-scaffolding-with-arks-and-links.html).
3. Hi-C scaffolding:
   The genome was further scaffolded using the Hi-C data with *Juicer* (v1.6) and the *3D de novo assembly (3D-DNA)* pipeline (v180114) (62).

Curation of the chromosome-level assembly. The *JuiceBox Assembly Tools* (*JBAT*) (v1.11.08) (63) were used for visual inspection and revision of the contact map. The putative misassemblies were revised and corrected. The decisions were made by taking into account breaks in synteny against the chicken chromosomes (GRCg6a) based on a pairwise alignment obtained with *nucmer* (64) and inspected with *Dot* (https://github.com/dnanexus/dot). Small scaffolds potentially containing inversions or translocations were examined within the super-scaffolds. Inversions or translocations detected in the dot plot were manually corrected using JBAT, ensuring changes maintained or improved consistency with the Hi-C contact map. Despite the ~35 million years of divergence between chickens and Indian peafowl, broad synteny across the majority of the genome is expected. However, intra-scaffold rearrangements consistent with the Hi-C contact map were left unchanged, as they could represent real species-specific differences. After completing the review, the assembly was finalized by exporting the modified assembly files and generating new FASTA files using the *run-asm-pipeline-post-review.sh* script from the *3D-DNA* pipeline. Finally, this revised assembly was sealed and closed by placing the debris scaffolds into gaps by running *run-asm-pipeline-post-review.sh* with options -s seal and -i 15000. The completeness of the final genome assembly was assessed using *BUSCO* (v5.8.2) (65) and the single-copy avian ortholog genes in the *aves_odb10* database. Summary statistics for the final assembly are provided in **table S1** and **figs. S2 and S3**.

Genome annotation of the Indian peafowl

RNA sequencing. RNA-seq data from five tissues of the same male individual used for the reference genome sequence were generated to support gene annotation. Total RNA was extracted from brain, lung, testes, skin, and kidney tissues and quantified using the Qubit RNA BR Assay Kit (Thermo Fisher Scientific). RNA integrity was assessed with the Agilent RNA 6000 Pico Kit on a Bioanalyzer 2100 (Agilent). RNA-seq libraries were prepared using the KAPA Stranded mRNA-Seq Kit for Illumina platforms (Roche), following the manufacturer's protocol with 500 ng of total RNA as input. Library size and quality were evaluated using the High Sensitivity DNA Bioanalyzer Assay (Agilent). The RNA-seq libraries were run on an Illumina HiSeq 4000 platform using paired-end reads (2 × 101 bp).

Repeat identification. Repeats in the reference genome assembly were annotated using *RepeatMasker* (v4.0.7) (http://www.repeatmasker.org) with a custom repeat library available for chicken.

Gene model inference. Gene annotation was performed by integrating transcript alignments, protein alignments, and *ab initio* gene predictions.

1. Transcript alignments based on RNA-seq data:

The multi-tissue RNA-seq reads were aligned to the genome using *STAR* (v.2.7.2a) (66) and transcript models were built for each tissue separately with *Stringtie* (v2.0.1) (67). These models were combined using *TACO* (68), and curated junctions to be used during the annotation process were identified with *Portcullis* (69) after mapping with *STAR*. *PASA* (v2.3.3) (70) was used to assemble transcripts, incorporating 2,104 Indian peafowl nucleotide sequences retrieved from NCBI (July 2020). Coding regions in the transcripts were identified with *TransDecoder program* (https://github.com/TransDecoder/TransDecoder), part of the *PASA* package.

2. Protein alignments:
   Complete chicken, human, and turkey proteomes were downloaded from UniProt (July 2020) and aligned to the genome using *spaln* (v2.4.7) (71).
3. *Ab initio* predictions:
   Ab initio gene predictions were performed on the repeat masked assembly with three different methods: *GeneID* (v1.4), Augustus (v3.2.3) (72), and *Genemark-ES* (v2.3e) (73) with and without RNA-seq junction evidence. The gene predictors were run with trained parameters for the human genome except for *Genemark* that runs in a self-trained manner.
4. Consensus gene models:
   EvidenceModeler (EVM; v1.1.1) (74) integrated all transcript, protein, and *ab initio* data to produce consensus coding DNA sequence (CDS) models. Untranslated regions (UTRs) and alternative splicing forms were annotated through two rounds of *PASA* updates.
5. Functional annotation:
   Functional annotation of the proteins was conducted using *Blast2GO* (75). First, a *BLASTp* (76) search was performed against the *nr* database (accessed February 2021). Second, protein domains were identified with *InterProScan* (77). The results were combined in *Blast2GO* to generate the final functional annotations.

ncRNA annotation. Non-coding RNAs (ncRNAs) were annotated through the following steps. First, the *cmsearch* tool (v1.1; from *Infernal*) (78, 79) was used to scan the genome against the RFAM RNA family database (v12.0) (80). Transfer RNAs (tRNAs) were identified with *tRNAscan-SE* (v1.23) (81). To detect lncRNAs, *PASA* assemblies not annotated as protein-coding genes were screened to identify expressed, non-translated sequences. Assemblies longer than 200 bp and not covered >80% by small ncRNAs were classified as lncRNAs. lncRNA transcripts were clustered into genes based on shared splice sites or significant sequence overlap. Summary statistics of the genome annotation are given in **table S1**.

Whole-genome resequencing and genetic mapping

Sampling of peafowl color varieties and DNA isolation. Blood samples or growing feathers were collected from 352 captive-raised Indian peafowl for whole-genome sequencing (**table S7**). Each individual was scored for the body color and wing phenotype, since they segregate independently. Color phenotypes were scored based on visual inspection, sometimes supplemented by genotype information provided by breeders for individuals known to be heterozygous for specific recessive mutations based on crossing records and studbook data. Samples included wild-type individuals and 20 distinct color varieties. Nine of these varieties are known to result from Mendelian mutations and therefore are determined by a single locus in the genome: Bronze, Cameo, Charcoal, Midnight, Opal, Purple, Ultramarine, Violet, and White/Pied. From segregation analyses in crosses, three of these varieties are known to be sex-linked and located on the Z-chromosome (Cameo, Purple, and Violet). For the remaining varieties (Brown, Chestnut, Hazel, Indigo, Ivory, Jade, Peach, Prussian-blue, Raw-umber, Sonja Violet, and Taupe), the inheritance patterns are either unknown, poorly supported, or attributed to combinations of two or more mutations. To investigate and take into account potential introgression from green peafowl (*Pavo muticus*) that might interfere with genetic mapping, four samples from green peafowl and 12 Spalding individuals, hybrids between Indian and green peafowl, were also collected.

Whole blood was collected as described earlier, but stored in 96% ethanol until DNA extraction. For birds where blood collection was not feasible, naturally molting feathers were plucked and similarly stored in ethanol. Genomic DNA was extracted from blood samples using a modified salt-based protocol, and from feathers it was extracted using the QIAamp UCP DNA Micro Kit (Qiagen). Potential RNA contamination was

removed by treating DNA extracts with RNase-A (Roche). Following DNA isolation, DNA quality and purity were assessed using spectrophotometry (Nanodrop) and fluorometric quantitation (Qubit dsDNA BR Assay Kit, ThermoFisher Scientific).

Illumina sequencing and read mapping. Genome-wide polymorphism data for genetic mapping was generated using whole-genome Illumina sequencing. Sequencing libraries were prepared for each of the 368 individuals (Indian peafowl, green peafowl, and their hybrids). For blood samples, which have higher DNA quality and larger quantities, libraries were constructed using the TruSeq DNA PCR-Free Library Preparation Kit (Illumina). For some feather follicle samples, which often yield lower DNA quality or quantity, libraries were prepared using the PCR-based Nextera XT Library Preparation Kit (Illumina). The quality of each library was assessed based on fragment size distribution, evaluated on an Agilent 2200 TapeStation using an HS D5000 Screen Tape (Agilent Technologies), and molarity, calculated using a KAPA qPCR library quantification kit (Roche). Libraries were sequenced using paired-end reads (2 × 150 bp) on an Illumina instrument.

Prior to data analyses, sequencing read quality was inspected with *FastQC* (v0.11.8) (https://www.bioinformatics.babraham.ac.uk/projects/fastqc/). Reads were then aligned to the Indian peafowl genome assembly generated in this study using *BWA-MEM* (v0.7.17-r1188) (82) with default parameters. Duplicate reads were flagged for downstream analysis using the *MarkDuplicates* function in *Picard* (v3.0.0) (http://broadinstitute.github.io/picard). Read group information was added to each BAM file using the *Picard* function *AddOrReplaceReadGroups*. Sequencing and mapping summary statistics were calculated using *SAMtools* (v1.11) (83). After mapping and duplicate removal, the final effective mean sequencing depth was 10.1× ± 5.3 (**table S7**).

Variant discovery and genotype calling. Single nucleotide polymorphisms (SNPs) and small insertions or deletions (indels) were identified using *GATK* (v4.2.6.1) (84). Briefly, *gVCF* files were generated for each individual using the *HaplotypeCaller* function requiring a minimum mapping quality of 30 and setting the heterozygosity value to 0.004. These files were subsequently combined into a single file using the function *CombineGVCFs*, and variants were called using the function *genotypeGVCFs* using default parameters except for the heterozygosity value (--heterozygosity 0.004). Prior to downstream analyses, additional filtering steps were applied at both the genotype and variant levels using *VCFtools* (v0.1.16) (85). The genotype of each individual was coded as 'missing data' if its quality was below 30 (--minGQ 30), or if its coverage was below 4× or higher than 58× (i.e., twice the average coverage of the individual with the highest coverage; --minDP 4 --maxDP 58). Following genotype filtering steps, variants with 50% or more missing genotype data across individuals (--max-missing 0.5 in *VCFtools*) were excluded.

Variant effect prediction. Filtered variants were annotated for their potential impact on protein-coding regions, including nonsynonymous, frameshift, splicing, and stop-gain mutations, using the *SnpEff* toolbox (v4.3t) (86). Based on these annotations, a subset of variants classified as high or moderate impact mutations was extracted for independent analysis of coding region variation. This filtering process resulted in a dataset of 228,553 variants.

Genome-wide association analysis. Before conducting the genome-wide association analysis, missing genotypes were imputed, and genotype data were phased using the software *Beagle* (v5.1) (87, 88). Association testing for each marker was performed with *GEMMA* (v0.98.1) (89) using a linear mixed model and coding each color morph as a binary trait (mutant vs. all others). The varieties that were known or discovered to be combinations of mutations were sometimes excluded from the control or case groups. Individuals belonging to the *white* variety (n = 17) were excluded from the mapping analyses of the other varieties because the mutation is epistatic, masking all other phenotypes. To minimize the potential confounding effects of population stratification and relatedness among individuals, a kinship matrix was included in the model as a random effect. The kinship matrix was estimated using *GEMMA*'s centered relatedness matrix option (-gk 1). Additionally, the first three principal components (PCs) from a principal components analysis (PCA), calculated with *PLINK* (v1.90b6.26) (90), were included as covariates. Variants with a minor allele frequency (MAF) lower than 10% were not considered. Significance thresholds for association testing were determined using a Bonferroni correction ($-\log_{10}$ [0.05/ number of loci]) applied to the likelihood ratio test for allele frequencies from *GEMMA*. Manhattan plots summarizing the associations were generated with the *qqman R* package (91).

Bulk RNA-sequencing

Sampling and RNA extraction. RNA-seq data were generated from 37 regenerating feather follicle samples of Indian peacocks, including neck feather follicles from wild-type and mutant varieties, and wing feather follicles from wild-type and Black-shoulder individuals (**table S8**). Feather follicles were collected in the pin stage of development (an early stage of feather development shortly after emerging through the skin), placed in RNAlater at room temperature for 8 hours, and subsequently stored at -80°C until RNA extraction. Total RNA was isolated using the RNeasy Plus Mini Kit (Qiagen). Following extraction, RNA integrity was assessed using a TapeStation RNA ScreenTape (Agilent), and RNA concentration was measured using a Qubit RNA BR assay kit (ThermoFisher Scientific).

Library preparation and sequencing. Illumina strand-specific RNA-seq libraries were prepared using the TruSeq Stranded mRNA Kit, according to the manufacturer's instructions. Sequencing of these libraries generated approximately 1,085 million paired-end reads (2 × 151 bp), with an average of ~70 million reads per individual (range: 41,911,332-97,612,226) (**table S8**).

Differential gene expression analysis. RNA-seq reads were aligned to the Indian peafowl reference genome using *HISAT2* (v.2.2.1) (92). Gene expression analyses were carried out using the *R* package *DESeq2* (v1.36.0) (93), with count data for each transcript generated with the *featureCounts* (94) function of the *Rsubread* package (v1.22.2) (95) against the annotation file. Differential expression analyses compared biological replicates of each mutant to wild-type birds (neck and wing analyzed separately). Transcripts with adjusted *P*-values (corrected for multiple testing) below 0.1 were considered significantly differentially expressed.

Allelic imbalance analyses. Allelic expression imbalance in neck and wing feather follicles was quantified in individuals heterozygous for the Black-shoulder nonsynonymous *MC1R* mutation (see main manuscript). For each sample, we estimated the relative expression of the two alleles either by directly counting RNA-seq reads overlapping the mutation site (when coverage exceeded 50×) or by targeted amplicon sequencing when RNA-seq coverage was below that threshold. Amplicon library preparation for Illumina sequencing followed Andrade *et al.* (2019) (96), with the following changes: first PCR with 5'-tailed primers (insert size: 177 bp; primer forward: 5' – TCGTCGGCAGCGTCAGATGTGTATAAGAGACAGCAATGAGCTCTTCCTGACG – 3'; primer reverse: 5' – GTCTCGTGGGCTCGGAGATGTGTATAAGAGACAGCAGCAGCATGAAGAGCATC – 3'), a touchdown PCR from 66-62°C, and PCR clean-up with 1:1 bead-to-sample volume ratio. The resulting libraries were pooled and sequenced using paired-end Illumina reads (2 × 150 bp). Reads were mapped to the reference genome using *BWA-MEM* (v0.7.17-r1188) with default parameters, and counts for the alleles were obtained by visual inspection with the *Integrative Genomics Viewer* (*IGV*) (97). For the neck, three heterozygous samples were analyzed ($n = 3$): two using RNA-seq and one using amplicon sequencing. For the wing, allelic proportions were obtained from two samples ($n = 2$) using amplicon sequencing only, as the RNA-seq datasets for wing follicles had <50× coverage at the mutation site.

Macroscopic photographs of feathers

The macroscopic photographs of the feathers from (i) the train eyespot region of wild-type and mutant peafowl varieties, (ii) the covert wing feathers of the common emerald dove (*Chalcophaps indica*), and (iii) the secondary wing feathers (or speculum) from the mallard duck (*Anas platyrhynchos*) were taken with a Sony Alpha 6400 combined with a Godox V1s flash. Both were installed in a setup with an angle of the flash of 13°.

Optical microscope characterization of the peafowl eyespot

Light microscope images and microscopic reflectance spectra were acquired with a correlative microscope setup consisting of a Zeiss Axio Imager Z2 optical microscope (Zeiss) combined with an MCS CCD UV-NIR spectrometer (Zeiss). The microscope was equipped with an Axiocam 820 color camera (Zeiss). Illumination was provided by a built-in halogen lamp (Osram) at 9.76 V. Images of individual barbules were acquired using a 20× objective with a numerical aperture (NA) of 0.5. Spectral measurements were performed using a 50× objective with an NA of 0.55. A silver mirror (Thorlabs) served as a 100% reflectance reference. The measured spot size was 16×16 µm. A single spectrum was recorded per spot. The integration time was adjusted to avoid

detector saturation and typically ranged between 100-200 ms for most color types, and 300-400 ms for *ultramarine* samples. Internal spectrometer smoothing was set to 5, and an averaging of 10 spectra was applied by the software. Binning was set to 2 × 2. Multiple spectra of the individual barbules were recorded, and the mean and standard deviation were calculated. For sample preparation, the individual barbules were carefully cut from the barb and adhered to a carbon pad (Plano).

Color measurement and chroma determination of the peafowl eyespot

Perceived color was quantified in the CIELAB (L*, a*, b*) color space, as defined by the International Commission on Illumination (CIE). CIELAB coordinates were calculated from the reflectance spectra recorded with the Zeiss Axio Imager Z2 microscope-spectrometer setup described above. The transformation followed standard procedures under the CIE 2006 convention, where L* represents lightness, a* corresponds to the green–red axis, and b* corresponds to the blue–yellow axis, under standard daylight illumination (D65) with a 2° observer angle and a step size of 5 nm. Chroma values were subsequently derived from these coordinates (98).

Spectroscopy of the peafowl eyespot

For the angle-dependent spectrometry, a customized setup was employed. A tungsten halogen lamp (HL-2000-HP-FHSA, Ocean Insight) served as the light source. The collected light was analyzed using a Flame-T-VIS-NIR-ES spectrometer (Ocean Insight). Both components were connected to collimators (74-UV-MP, Ocean Insight), which were mounted on mechanical arms and linked via glass fiber cables (105 µm, 0.22 NA Fiber Patch Cable, Thorlabs). These arms were controlled using two motorized rotational stages (Standa) to precisely adjust the angles of incidence and detection. Spectra were recorded using a custom *LabView*-based acquisition software. With this software, the integration time, averaging, and data export were controlled.

For sample preparation, the feathers were glued to a glass slide using carbon pads (Plano), ensuring a flat and stable surface for accurate measurements. Specular reflection measurements were conducted. The incidence angle was varied from 60° to 3° and subsequently from −3° to −60° in 1.5° steps. Measurements for incidence angles between 3° and −3° were not possible due to the obstruction of the light signal by the detector arm. Because angle-dependent spectra recorded from opposite sides exhibited symmetric (mirrored) peak behavior, only one side of the measurements was used for subsequent analysis (**fig. S17**). For reference measurements, a white standard (Labsphere) was used as the maximum reference, measured at the same angles as the sample. The minimum reference was obtained by recording the spectrometer signal without illumination. An integration time of 2800 ms and an averaging of 10 scans were used. For samples with a well-ordered photonic crystal (wild-type, Purple, Ultramarine, and Violet feathers), the spectra were smoothed over 200 points using the Adjacent-Averaging method in *OriginPro* (v2023b) (OriginLab), and the peak position was determined based on the highest intensity. For samples exhibiting either a less well-ordered photonic crystal or a highly ordered but few-layer photonic crystal structure that resulted in low reflectance (e.g., Bronze and Opal feathers), the spectra were first smoothed and subsequently baseline-corrected using a spline function in *OriginPro*, as the broadband pigment background otherwise obscured the structural peak. Peak positions were then determined by applying a Gaussian fit to the peak region, also in *OriginPro*. For samples without a photonic crystal (Cameo and Charcoal feathers), the spectra were only smoothed (200-point), and no peak could be evaluated. Because transformations did not significantly impact the peak wavelength identified for mutants across the multiangle measurements, values of the 200-point measures were used for peak selection (**fig. S18**).

Transmission Electron Microscopy (TEM)

TEM initial sample preparation. Feathers used for TEM were collected from the same sources described for macroscopic photographs, including wild-type and mutant peafowl, the common emerald dove, and the mallard duck. Feathers were washed twice with 0.1 M phosphate buffer (PB, pH 7.4) containing 0.5% Tween 20 (Carl Roth) and stored overnight at 4°C in the same solution. Samples were then treated for 2 hours at room temperature with a solution of 1.5% potassium ferricyanide (Merck) and 1% osmium tetroxide (>99.95%, Emsdiasum) in 0.1 M PB (pH 7.4). Afterwards, the feathers were washed three times in the same PB-Tween solution and stored overnight at 4°C.

Preparation of 0.1 M Phosphate Buffer Solution (Sørensen method). To prepare 1 liter of phosphate buffer solution (PB), 14.417 g of disodium hydrogen phosphate dihydrate ($Na_2HPO_4 \cdot 2H_2O$, ≥99%, Carl Roth) and 2.622 g of sodium dihydrogen phosphate monohydrate ($NaH_2PO_4 \cdot 1H_2O$, ≥98%, Carl Roth) were dissolved in 900 ml of Milli-Q water. The pH of the solution was adjusted to 7.4 using hydrochloric acid (HCl, ≥25%, Carl Roth) or sodium hydroxide (NaOH, ≥98%, Carl Roth). Finally, Milli-Q water was added to bring the total volume to 1000 ml.

Feather dehydration process. Feathers were progressively dehydrated at room temperature through a graded ethanol–acetone series. Samples were first immersed in 70% ethanol (≥99.8%, denatured, Carl Roth) for 60 minutes, followed by 80%, 90%, and 100% ethanol (denatured) for 30 minutes each. The dehydration continued with 100% ethanol (undenatured, ≥99.8%, Carl Roth) for 30 minutes, then a 50/50 mixture of ethanol (≥99.8%, Carl Roth) and acetone (≥99.8%, Carl Roth) for 30 minutes, followed by 100% acetone for 30 minutes. Finally, samples were immersed in 2/3 acetone and 1/3 Epon resin, and then 1/3 acetone and 2/3 Epon resin, each for 30 minutes at room temperature.

Preparation of Epon resin. Epon resin was prepared by mixing Solution A and Solution B as follows:

1) Solution A: 75 mL Glycidether 100 (Carl Roth) and 120 mL Glycidether hardener DBA (Carl Roth)
2) Solution B: 120 mL Glycidether 100 (Carl Roth) and 105 mL Glycidether hardener MNA (Carl Roth)

The two solutions were combined and supplemented with 2% accelerator DMP-30 (Carl Roth). The mixture was gently stirred until homogeneous and stored at 4°C until use.

Embedding and sectioning. Dehydrated feathers were embedded in Epon resin with glycidether accelerator DMP-30 (Carl Roth) overnight at 4°C. Polymerization was carried out by incubating samples at 60°C overnight, followed by 80°C, again overnight. The Epon blocks were cut into 40-60 nm thick sections using a Leica Ultracut UCT. These sections were treated with chloroform (≥99%, Carl Roth) to ensure a flat morphology and transferred onto copper grids coated with Pioloform FN65 (Plano) film.

Section preparation and image acquisition. Sections were stained with 10% uranyl acetate (>98%, Serva) for 10 minutes, rinsed with Milli-Q water, treated with 2.8% lead citrate (Merck) for 10 minutes, and rinsed again with Milli-Q water. Imaging was performed using a Zeiss Leo 906 transmission electron microscope (Zeiss) operated in bright-field mode at 60 kV with a TRS 2048 digital camera system.

Nanostructure measurements: Several variables related to melanosome size and spatial distribution in the keratin matrix were measured from TEM images. These variables included: number of melanosome layers (*N*), distance between layers (*a*), distance between melanosomes within a layer (*b*), cortex thickness (*c*), diameter of melanosomes (*Dm*), diameter of air pockets (*Da*), and length of melanosomes (*Lm*). Measurements were manually taken using the *straight line* and *measure* tools from *ImageJ* (99) software on longitudinal and transversal cuts of feather barbules. For each breed–zone combination ($n = 42$), 100 measurements were taken, and the mean and standard deviation were calculated.

Statistical analyses. Linear discriminant analyses (LDA) were conducted using either "phenotype" or "area" as the grouping variable. Model performance was assessed as the percentage of individuals correctly reclassified to their original group, based on a classifier that minimized each sample's multivariate Mahalanobis distance to the group mean. Pearson's correlation coefficients (r) were calculated to identify significant associations ($P < 0.05$) between Z-score standardized averages of the original measurements and the axes of the LDA models. Analyses were implemented using the *MASS R* package (100). To estimate the relative contribution of each variable to total dataset variance, squared loadings were weighted, summed, and normalized across LD axes to obtain contribution percentages.

Histology of regenerating feather follicles

Regenerating feather follicles at the pin stage of development were collected from the following sources: (i) the neck region of wild-type and mutant peafowl varieties, (ii) the covert wing feathers of the common emerald dove, and (iii) the secondary wing feathers (or speculum) from the mallard duck. The samples were fixed in 4% paraformaldehyde prepared in 0.1M PBS (pH 7.4) at 4°C for four days. After fixation, the follicles were washed in PBS and stored in 70% ethanol until further processing. The follicles were then dehydrated in an ascending ethanol series, cleared in xylene, and embedded in Paraplast Plus (Sigma). Longitudinal 10 µm

885 thick sections were cut with a Reichert-Jung 2040 Autocut Rotary Microtome. The ribbon of sections was
886 floated on the surface of distilled water at 37°C and mounted onto gelatin-coated glass slides. The sections
887 were heated at 65°C for 1 hour to melt the paraffin, deparaffinized in xylene, and mounted with DPX mounting
888 medium (Sigma). Images were captured using a Zeiss Axio Imager M2 epifluorescent microscope equipped
889 with AxioCam MRc5 camera (Zeiss) and *AxioVision Se64* (vRel.4.9.1) software (Zeiss). A 63× Plan-
890 apochromat oil immersion objective was used for imaging.
891
892 **Chemical characterization of melanin**
893 Fully grown feathers from the same sources used in the histological analysis (see previous section) were
894 collected for the quantification of melanin content. Feathers were kept in black plastic zip-lock bags at room
895 temperature, protected from direct light to prevent degradation. Approximately 15 mg of each feather sample
896 was homogenized in water using a Ten-Broeck glass homogenizer at a concentration of 10 mg/ml. An aliquot
897 of 100 µl (equivalent to 1 mg of sample) was mixed with 900 µL of Soluene-350 (Perkin-Elmer) in a 10 ml
898 screw-capped conical test tube (101). The mixture was vortexed and heated at 100˚C in a boiling water bath
899 for 15 minutes, then cooled. This process was repeated, followed by vortexing and centrifugation at 4,000 g
900 for 3–5 minutes. The resulting supernatant was analyzed using a spectrophotometer at 500 nm (A500) and
901 650 nm (A650). A blank reference sample (100 µl water and 900 µl Soluene-350) was processed under the
902 same conditions. To analyze pyrrole-2,3,5-tricarboxylic acid (PTCA), pyrrole-2,3-dicarboxylic acid (PDCA),
903 and thiazole-2,4,5-tricarboxylic acid (TTCA), alkaline hydrogen peroxide oxidation (AHPO) was
904 employed(102), while 4-amino-3-hydroxyphenylalanine (4-AHP) and 3-amino-4-hydroxyphenylalanine (3-
905 AHP) were quantified via hydroiodic acid (HI) hydrolysis (103). Absorbances due to proteins (0.021 and 0.001
906 per mg of feather) were subtracted from A500 and A650 values. Total melanin, eumelanin, benzothiazine-
907 pheomelanin (BT), and benzothiazole-pheomelanin (BZ) contents were calculated by multiplying the
908 concentrations of A500, PTCA, 4-AHP, and TTCA by factors of 101 (101), 80 (102), 9 (104), and 34 (105),
909 respectively. The quantification of different metabolites from these pigment analyses is available in **tables S6**
910 **and S9**.
911
912 **Single-cell RNA-sequencing**
913 *Tissue preparation and production of libraries for scRNA*-seq. The experiments were conducted on
914 regenerating feathers of one male emerald dove and two male mallards, taking advantage of the fact that these
915 species express within some feathers both iridescent and non-iridescent colors (**Fig. 6A; fig. S11**). For each
916 species, two scRNA-seq libraries were generated per individual feather to capture the structural coloration
917 asymmetry, with one library representing the left side and the other the right side (emerald dove: $n = 4$ libraries;
918 mallard: $n = 4$ libraries). For the emerald dove, wing covert feathers belonging to a row of feathers displaying
919 color asymmetry relative to the central axis of the feather itself (i.e., the rachis) were analyzed. The feathers
920 were sampled approximately nine days after being plucked, at a time when color differences between the two
921 sides had just started to be visible. For the mallard duck, feathers of the speculum, a bright iridescent patch of
922 inner secondary flight feathers, were sampled. Mallard feathers were sampled 20 days after plucking during
923 the formation of the iridescent patch.
924 For all the experiments, regenerating feathers were plucked, immediately placed on ice in Hanks'
925 Balanced Salt Solution (HBSS, Gibco), and dissected under a stereomicroscope. The distal-most half of the
926 feather, which is fully keratinized at the time of sampling, was removed (**fig. S11**). The remaining feather was
927 incised longitudinally along the rachis and flattened by pinning its corners in HBSS. This exposed the inner
928 pulp, which was then carefully removed with forceps. At this stage, in both emerald dove and mallard feathers,
929 the color asymmetry is evident as a darkening of the tissue where structural coloration would emerge during
930 later keratinocyte maturation. After confirming this difference, the feather was further cut at about 4 mm from
931 its base, at a level where barb ridges are formed, and the proximal-most portion of the sample was kept. The
932 left and right halves of the feather were then separated by cutting along an evident midline devoid of
933 keratinocytes, and processed individually for cell dissociation.
934 The samples were dissociated in 2mg/ml dispase solution in DMEM (Gibco) for 60 min at 37°C at 300
935 rpm. After 10 minutes of incubation, 30 µl of Liberase solution (Roche) in DMEM (10 mg/ml) was added,
936 and the mixture was passed through a pipette tip several times every 10 minutes. The partially dissociated
937 tissues were pelleted by centrifugation at 400 × g at 4°C and incubated in 0.05% Trypsin/EDTA (Gibco) for

938 10 minutes at 37°C and 300 rpm mixing, and occasionally passed through a pipette tip. The digestion was
939 arrested by adding 10% FBS (Gibco) in DMEM, the feather sheath was removed with forceps, and the mixture
940 was treated with DNase I (Roche) at 37°C for 5 min and 300 rpm. The cells were then washed twice in 0.4%
941 BSA (Sigma-Aldrich) in HBSS (with calcium and magnesium), filtered twice through a 40 µm-mesh filter
942 (Falcon) and once through a Flowmi 40 µm Cell Strainer (Bel-Art SP Scienceware), resuspended in 0.4%
943 BSA in HBSS, and counted in a hemocytometer after trypan blue staining. The resuspended cells were
944 partitioned and barcoded separately using a 10x Genomics Chromium instrument (10x Genomics) following
945 the manufacturer's protocol (Chromium Next GEM Single Cell 3′ Reagent Kits v3.1 Dual Index, Rev C) and
946 targeting the recovery of 10,000 cells per reaction. Following quantification and quality control (LightCycle
947 qPCR, Agilent TapeStation), the libraries were sequenced on an Illumina instrument and demultiplexed using
948 the *CellRanger Fastq* pipeline (10x Genomics). Summary statistics for the single-cell libraries are given in
949 **table S10**.

950 *Preprocessing of the scRNA-seq data*. The scRNA-seq libraries were pre-processed individually using the
951 *count* pipeline in *Cell Ranger* (v7.0.1; 10x Genomics). Briefly, the reads were aligned to the reference genomes
952 (emerald dove: this study and described below; mallard: GCF_047663525.1) using the splicing-aware aligner
953 *STAR* (66) as implemented in *Cell Ranger*. Uniquely mapped reads within the start and end coordinates of
954 each gene were considered for UMI counts, and cells were distinguished from empty droplets using an
955 algorithm based on the *EmptyDrop* method (106). Filtered count matrices were imported into the *R* package
956 *Seurat* (v5.3.0) (107) and further filtered to remove low-quality cells. For the emerald dove ($n = 4$) and mallard
957 ($n = 4$) libraries, cells with UMI counts between 2,000 and 18,000 and between 2,000 and 20,000, respectively,
958 and expressing more than 750 features were retained. After filtering, 10,213 emerald dove cells and 20,991
959 mallard cells remained. Gene expression matrix processing (data normalization and scaling) and
960 dimensionality reduction by Principal Components Analysis (PCA) were performed independently for each
961 library in *Seurat* with default settings. For each species separately, the libraries were integrated using the
962 *HarmonyIntegration* method as implemented in the *IntegrateLayers* function in *Seurat*.

963 *Cluster annotation*. Unsupervised clustering of cells was performed on the integrated data using the
964 *FindNeighbors* (*k.param* = 50, $dims_{dove}$ = 50; $dims_{mallard}$ = 30) and the *FindClusters* ($resolution_{dove}$ = 0.14;
965 $resolution_{mallard}$ = 0.05) functions in *Seurat.* Differential gene expression analyses between each cluster and all
966 remaining cells in the dataset, as well as between selected cluster pairs, were conducted with the Wilcoxon
967 rank-sum test as implemented in the *FindAllMarkers* and *FindMarkers* functions in *Seurat,* respectively.
968 Cluster annotation was manually curated based on the expression of known marker genes and the top
969 differentially expressed genes in each cluster. An overview of the cluster annotations and representative
970 marker genes is shown in **figs S12-S15**, and complete lists of the top differentially expressed genes for each
971 cluster are provided in **Data S3** and S**4**.
972 Within each dataset, clusters of cells showing enriched expression of keratin genes (e.g., *Keratin-14*,
973 *Keratin-19*, *Keratin-8*, *Keratin-5*) and known keratinocyte markers (e.g., *SHH* and *COL17A1*) (108–110) were
974 collectively labeled as keratinocytes. In both datasets, two distinct clusters of cells showed enriched expression
975 of melanocyte-specific markers such as *TYR*, *TYRP1*, *PMEL*, and *MLANA*. Within each dataset, pairwise
976 differential expression analyses between these clusters identified one population of cells (labeled as
977 melanocytes 1) showing upregulation of several melanocyte markers (e.g., *TRPM1*: Log_2FC_{dove} = 4.6; $P <$
978 0.0001; $Log_2FC_{mallard}$ = 3.7, $P < 0.0001$). In both datasets, the second population (labeled as melanocytes 2)
979 showed enriched expression of several glutathione S-transferases (e.g., Hematopoietic Prostaglandin D
980 Synthase*, HPGDS*: Log_2FC_{dove} = 1.76; $P < 0.0001$; $Log_2FC_{mallard}$ = 1.29, $P < 0.0001$). A previous study in
981 quails identified two distinct melanocyte lineages committed to the production of eumelanin or pheomelanin
982 within embryonic skin tracts, eventually forming black or yellow feather stripes (111). These populations were
983 negative and positive for the melanoblast/melanocyte early marker (MelEM) monoclonal antibody, which
984 binds a glutathione S-transferase alpha class subunit and labels melanoblasts and early melanocytes in the
985 avian embryo (112, 113). Increased glutathione S-transferase expression and decreased melanocyte-specific
986 marker gene expression suggest that these cells are early differentiating melanocytes, possibly progressing
987 towards pheomelanin production. Based on the common expression of many melanocyte markers, these
988 populations of cells were collectively labeled as melanocytes and were considered together for some analyses.

Additional small but clearly distinct clusters were manually annotated. In both datasets, a small cluster of cells expressing erythrocyte markers, such as *HBAA* and *HBB*, was manually assigned and annotated as erythrocytes (emerald dove: n = 30 cells; mallard: n = 67 cells). In the mallard dataset, co-expression of erythrocyte markers and some keratin genes suggests the contamination of small numbers of low-quality keratinocyte cells within the erythrocyte cluster. In the emerald dove dataset, one small cluster of cells (n = 29 cells) showed enriched expression of neural crest-derived cell genes (e.g. *FOXD3* and *NGFR*) and likely represents the melanoblast population at the base of the feather follicle. In the absence of canonical melanoblast markers (e.g., *DCT, EDNRB2*), this cluster was manually assigned and labeled as neural crest-derived cells. Overall, these changes represented minor manual adjustments to the clustering output, limited to clearly distinct and well-characterized cell populations, and did not affect the overall interpretation of the data. The remaining clusters in both datasets were left unchanged from the clustering provided by *Seurat* and were annotated based on the expression of marker genes for cell types previously described in regenerating feather follicles (7).

For the emerald dove, the final annotation of cells consisted in 11 clusters: (1) keratinocytes, n = 4,261; (2) mesenchymal cells 1, n = 1,716; (3) melanocytes 1, n = 1,430; (4) endothelial cells, n = 1,215; (5) melanocytes 2, n = 566; (6) leukocytes 1, n = 373; (7) mesenchymal cells 2, n = 276; (8) leukocytes 2, n = 239; (9) leukocytes 3, n = 77; (10) erythrocytes, n = 31, and (11) neural crest-derived cells, n = 29. For the mallard, the final annotation consisted of 8 clusters: (1) keratinocytes, n = 14,312; (2) mesenchymal cells 1, n = 4,376; (3) melanocytes 1, n = 855; (4) leukocytes, n = 491; (5) endothelial cells, n = 406; (6) melanocytes 2, n = 334; (7) mesenchymal cells 2, n = 150; and (8) erythrocytes, n = 67.

Tissue composition analyses. For both datasets, cell counts per cluster were extracted from each library (n = 4 libraries per species) and normalized by library total cell counts. Cell-type proportions in the samples were compared between conditions (iridescent color vs. non-iridescent color) with a Welch Two Sample t-test in *R* (n = 2 replicates per condition). Cell-type counts and summary test statistics are reported in **table S11**.

Differential gene expression analyses. For each species and for each cell type, differential expression analyses were performed using a pseudo-bulk approach. For all the analyses, differentially expressed genes with $\text{Log}_2\text{FC} \geq 0.5$ and P-value ≤ 0.05 were considered. To test for differences between feather samples developing iridescent or non-iridescent colors (i.e., color types), summed UMI counts within each sample ($n_{\text{iridescent}}$ = 2 samples per dataset, $n_{\text{non-iridescent}}$ = 2 samples per dataset) were used as inputs for *DESeq2* (v1.48.1) with default parameters as implemented in the *FindMarkers* function in *Seurat*. Lists of differentially expressed genes per cell type for the emerald dove and the mallard are reported in **Data S1 and S2**, respectively.

Gene ontology enrichment analyses. For each species, gene ontology (GO) enrichment analyses were carried out for the lists of melanocyte-specific differentially expressed genes (considering the merged populations of melanocytes 1 and 2) using the *topGO* package (v.2.59.0) (https://bioconductor.org/packages/topGO) in *R*. For each dataset, enrichment was assessed by comparing the frequencies of GO term annotations in the differentially expressed gene sets against background GO term frequencies in the species' genomes, followed by statistical testing by Fisher's exact test. GO terms associated with the differentially expressed gene sets for the emerald dove and the mallard are reported in **Data S5 and S6**, respectively.

Emerald dove genome assembly and annotation. The individual used to produce the draft reference genome sequence of the emerald dove was one adult male obtained from a licensed breeder in Portugal. Whole blood was collected using a sterile needle into a heparin-free capillary, transferred into a 10ml Vacutainer K2 EDTA tube (BD Biosciences), and immediately snap-frozen in liquid nitrogen. The sample was subsequently shipped to the genomic services provider Macrogen (Seoul, South Korea) in dry ice. High molecular weight DNA was extracted from 140 µl of blood using the Wizard HMW DNA Extraction kit (Promega). DNA quantity and integrity were assessed using a Victor Nivo Multimode Microplate Reader (PerkinElmer) with the QuantiFluor® dsDNA System (Promega) method, the Femto Pulse System (Agilent), and a N120 NanoPhotometer (IMPLEN). The average fragment length of the extracted DNA was estimated to be approximately 44 kb.

A Pacific Biosciences (PacBio) Revio sequencing library was prepared from 7 µg of DNA input. gDNA was sheared with the Megaruptor® 3 (Diagenode) and both purified and size-selected using AMPure PB magnetic beads (Pacific Biosciences). The size distribution was determined using the Femto Pulse System

(Agilent) for all size quality controls. The library insert size was within the optimal size range. A total of 10 µL of library was prepared using the PacBio SMRTbell prep kit 3.0 and SMRTbell templates were annealed using the Revio polymerase kit (Pacific Biosciences). Sequencing was performed using a Revio sequencing plate and Revio SMRT Cell tray. Each SMRT cell was captured using a 24-hour movie time using the PacBio Revio (Pacific Biosciences) sequencing platform by Macrogen (Seoul, South Korea). The subsequent steps are based on the PacBio Sample Net-Shared Protocol, available at https://www.pacb.com/.

A total of 6,372,772 HiFi long reads with an average length of 13,480 bp were generated, which corresponds to ~71× coverage of the approximate size of a bird genome (~1.2 Gb). Contig assembly was performed using *Hifiasm* (v0.20.0-r639) (114), resulting in 1,283,043,043 bp of primary assembly (contigs n = 315) with a contig N50 of 33 Mb and a maximum length of 121.1 Mb. These contigs were scaffolded into a pseudochromosome assembly using *RagTag* (v2.1.0) (115), with the rock pigeon *bColLiv1.pat.W.v2* genome assembly (GCF_036013475.1) serving as the reference. The final assembly comprised 219 scaffolds with an N50 of 83.8 Mb and a maximum scaffold length of 215.1 Mb. Completeness analysis of the assembly was performed using *BUSCO* (v5.8.2) and the 8,338 single-copy avian ortholog genes (*aves_odb10*), which indicates that our genome assembly was 97.1% complete. Annotation of the draft reference genome was conducted using *Liftoff* (v1.6.3) (116) by lifting over gene models from the annotation available for the rock pigeon genome. Genes of interest for the single-cell analyses were manually inspected.

Data availability

The whole-genome sequencing (Illumina), RNA sequencing, and single-cell RNA sequencing data generated in this study are available at the NCBI BioProject under accession number PRJNA1216069. The reference genome assembly and associated data, including Oxford Nanopore sequencing, Hi-C, and linked-read sequencing, are available under the ENA project accession PRJEB87866. The raw data supporting the nanostructural and optical analyses are available in the public repository Zenodo at the following DOI: XXXXXX.

Acknowledgements

We thank the numerous breeders who kindly provided feather and tissue samples for data analyses. We are also grateful to Jens Poulsen, Natalia Gusakova (Unsplash), and Clucking Fens Farm (www.cluckingfens.co.uk) for peafowl photographs used in Fig. 1, Fig. 5, and fig. S1. We thank Ibanidis Lda (Versele-Laga distributor), ZooService Lda (Manitoba distributor), and Papa d'Ovo (Domus Molinari distributor) as sponsoring partners of food, husbandry cages, and accessories. We thank Joana C. Carvalho for helping produce the main figures. We thank Nico Nees for kindly providing the code used for the chroma calculations, Bettina Winzer for her assistance in aligning the angle-dependent spectrometer, and Carmen Rubach for helpful discussions. This work was supported by the European Research Council under the European Union's Horizon 2020 research and innovation program to MC (grant agreement No. 101000504); by the Portuguese Foundation for Science and Technology (FCT, https://www.fct.pt) research contracts to MC (CEECINST/00014/2018/CP1512/CT0002), PA (2020.01405.CEECIND/CP1601/CT0011), and PMA (2020.01494.CEECIND); by research fellowships to CIM (SFRH/BD/147030/2019) and RAf (UI/BD/154451/2022), in the scope of the Biodiversity, Genetics and Evolution (BIODIV) PhD program; by the Deutsche Forschungsgemeinschaft (DFG, German Research Foundation) – Project-ID 416229255 – SFB 1411; by an EASI-Genomics project under CNAG-CRG coordination, funded by the European Union's Horizon 2020 research and innovation programme (Grant Agreement No. 824110); by national funds through FCT to CE3C (UIDB/00329/2020, https://doi.org/10.54499/UIDB/00329/2020); and by funding from Vetenskapsrådet (VR 2017-02907), and the Knut and Alice Wallenberg Foundation (KAW 2023.0160 and KAW 2024.0058) to LA.

Author Contributions

Conceptualization: M.C., N.V., J.C.C., L.A., S.B., C.B., R.A., P.M.A.

Methodology: S.B., P.M.A., P.P., P.A., R.Af., S.Af., J.Ca., R.J.L., J.M.A., M.F.A., R.A., C.B., M.P.J.N., J.B., A.Hi., A.He., E.S., B.A.Z., C.I.M., C.F., M.A.A., F.C., J.G.G., C.Z., M.G., T.A., S.I., K.W.

Investigation: S.B., P.M.A., P.P., P.A., R.Af., S.Af., J.Ca., R.J.L., J.M.A., M.F.A., R.A., C.B., M.P.J.N., J.B., A.Hi., A.He., E.S., B.A.Z., C.I.M., C.F., M.A.A., F.C., J.G.G., C.Z., M.G., T.A., S.I., K.W.

Data curation: S.B., P.M.A., P.P., P.A., R.A., C.B., J.B., A.Hi., A.He., E.S., B.A.Z., C.F., F.C., J.G.G., C.Z., M.G., T.A.
Formal analysis: S.B., M.F.A., R.A., P.P., C.B., M.P.J.N., J.B., A.Hi., A.He., E.S., B.A.Z.
Visualization: S.B., R.A., C.B., C.F., J.A.A., T.A., M.P.J.N., J.B., A.Hi., A.He., E.S., B.A.Z.
Supervision: M.C., N.V.

Declaration of interests

S.B., R.A., P.M.A. and M.C. are inventors on a pending patent application related to the technology described in this work. S.B., P.M.A. and M.C. are founders and shareholders of *Animal Genotyping Innovations (AGI), Lda*. The remaining authors declare no competing interests.

References

1. S. Kinoshita, Helen Ghiradella, Lars Olof Björn, "Spectral tuning in Biology II: Structural Color" in *Photobiology*, Björn L., Ed. (Springer, 2015).
2. I. C. Cuthill, *et al.*, The biology of color. *Science (1979).* **357** (2017).
3. M. D. Shawkey, L. D'Alba, Interactions between colour-producing mechanisms and their effects on the integumentary colour palette. *Philosophical Transactions of the Royal Society B: Biological Sciences* **372**, 20160536 (2017).
4. P. Vukusic, J. R. Sambles, Photonic structures in biology. *Nature* **424**, 852–855 (2003).
5. G. E. Hill, K. J. McGraw, *Bird coloration. In Mechanisms and Measurements, 1* (Harvard University Press, 2006).
6. T. F. Cooke, *et al.*, Genetic mapping and biochemical basis of yellow feather pigmentation in budgerigars. *Cell* **171**, 427-439 (2017).
7. R. Arbore, *et al.*, A molecular mechanism for bright color variation in parrots. *Science (1979).* **386** (2024).
8. M. A. Gazda, *et al.*, A genetic mechanism for sexual dichromatism in birds. *Science (1979).* **368**, 1270–1274 (2020).
9. R. Price-Waldman, M. C. Stoddard, Avian coloration genetics: recent advances and emerging questions. *Journal of Heredity* **112**, 395–416 (2021).
10. R. O. Prum, "Anatomy, physics, and evolution of avian structural colors" in *Bird Coloration, Volume 1: Mechanisms and Measurements*, G. E. Hill, K. J. MCGraw, Eds. (Harvard University Press, 2006).
11. V. Saranathan, C. Finet, Cellular and developmental basis of avian structural coloration. *Curr. Opin. Genet. Dev.* **69**, 56–64 (2021).
12. M. C. Stoddard, R. O. Prum, How colorful are birds? Evolution of the avian plumage color gamut. *Behavioral Ecology* **22**, 1042–1052 (2011).
13. M. F. Land, The physics and biology of animal reflectors. *Prog. Biophys. Mol. Biol.* [Preprint] (1972).
14. C. M. Eliason, R. Maia, M. D. Shawkey, Modular color evolution facilitated by a complex nanostructure in birds. *Evolution (N. Y).* **69**, 357–367 (2015).
15. R. Maia, D. R. Rubenstein, M. D. Shawkey, Key ornamental innovations facilitate diversification in an avian radiation. *Proceedings of the National Academy of Sciences* **110**, 10687–10692 (2013).
16. M. Nicolai, *et al.*, The evolution of brilliant iridescence in birds. [Preprint] (2025). https://doi.org/10.21203/rs.3.rs-8020267/v1
17. K. K. Nordén, *et al.*, Melanosome diversity and convergence in the evolution of iridescent avian feathers-Implications for paleocolor reconstruction. *Evolution (N. Y).* **73**, 15–27 (2019).
18. C. M. Eliason, *et al.*, Transitions between colour mechanisms affect speciation dynamics and range distributions of birds. *Nat. Ecol. Evol.* **8**, 1723–1734 (2024).
19. M. P. J. Nicolaï, *et al.*, The evolution of multiple color mechanisms Is correlated with diversification in sunbirds (Nectariniidae). *Syst. Biol.* **73**, 343–354 (2024).
20. R. Dakin, R. Montgomerie, Eye for an eyespot: how iridescent plumage ocelli influence peacock mating success. *Behavioral Ecology* **24**, 1048–1057 (2013).
21. S. M. Doucet, M. G. Meadows, Iridescence: a functional perspective. *J. R. Soc. Interface* **6** (2009).
22. B. E. Droguet, *et al.*, Large-scale fabrication of structurally coloured cellulose nanocrystal films and effect pigments. *Nat. Mater.* **21**, 352–358 (2022).
23. N. Vogel, *et al.*, Color from hierarchy: Diverse optical properties of micron-sized spherical colloidal assemblies. *Proc. Natl. Acad. Sci. U. S. A.* **112**, 10845-10850 (2015).
24. V. P. Patil, J. D. Sandt, M. Kolle, J. Dunkel, Topological mechanics of knots and tangles. *Science (1979).* **367**, 71–75 (2020).
25. K. K. Nordén, C. M. Eliason, M. C. Stoddard, Evolution of brilliant iridescent feather nanostructures. *Elife* **10** (2021).

26. R. Maia, R. H. F. Macedo, M. D. Shawkey, Nanostructural self-assembly of iridescent feather barbules through depletion attraction of melanosomes during keratinization. *J. R. Soc. Interface* **9**, 734–743 (2012).
27. H. Durrer, Schillerfarben der Vogelfeder als Evolutionsproblem. *Denkschr. Schweiz Naturforsch. Ges.* **14**, 1–126 (1977).
28. C. M. Eliason, R. Maia, J. L. Parra, M. D. Shawkey, Signal evolution and morphological complexity in hummingbirds (Aves: *Trochilidae*). *Evolution (N. Y).* **74**, 447–458 (2020).
29. J. Zi, *et al.*, Coloration strategies in peacock feathers. *Proc. Natl. Acad. Sci. U. S. A.* **100**, 12576-12578 (2003).
30. P. Freyer, D. G. Stavenga, Biophotonics of diversely coloured peacock tail feathers. *Faraday Discuss.* **223**, 49–62 (2020).
31. H. Durrer, Bau und Bildung der Augfeder des Pfaus (*Pavo cristatus* L.). *Revue suisse de zoologie.* (1965). https://doi.org/10.5962/bhl.part.75643.
32. D.-J. Jeon, S. Paik, S. Ji, J.-S. Yeo, Melanin-based structural coloration of birds and its biomimetic applications. *Appl. Microsc.* **51**, 14 (2021).
33. T. Okazaki, Reflectance spectra of peacock feathers and the turning angles of melanin rods in barbules. *Zoolog. Sci.* **35**, 86–91 (2018).
34. R. Maia, L. D'Alba, M. D. Shawkey, What makes a feather shine? A nanostructural basis for glossy black colours in feathers. *Proceedings of the Royal Society B: Biological Sciences* **278**, 1973–1980 (2011).
35. D. R. Rubenstein, *et al.*, Feather gene expression elucidates the developmental basis of plumage iridescence in African starlings. *Journal of Heredity* **112**, 417–429 (2021).
36. G. Gao, *et al.*, Comparative genomics and transcriptomics of Chrysolophus provide insights into the evolution of complex plumage colouration. *Gigascience* **7**, giy113 (2018).
37. H. Dürrer, Schillerfarben beim Pfau (*Pavo Cristatus* L.). *Naturf. Ges. Basel* **73** (1962).
38. R. Sarangarajan, R. E. Boissy, *Tyrp1* and Oculocutaneous Albinism Type 3. *Pigment Cell Res.* **14**, 437–444 (2001).
39. J. Li, *et al.*, A missense mutation in *TYRP1* causes the chocolate plumage color in chicken and alters melanosome structure. *Pigment Cell Melanoma Res.* **32**, 381–390 (2019).
40. C. R. Goding, H. Arnheiter, MITF—the first 25 years. *Genes Dev.* **33**, 983–1007 (2019).
41. H. van Grouw, W. Dekkers, The taxonomic history of Black-shouldered Peafowl; with Darwin's help downgraded from species to variation. *Bull. Br. Ornithol. Club* **143** (2023).
42. N. I. Mundy, A window on the genetics of evolution: *MC1R* and plumage colouration in birds. *Proceedings of the Royal Society B: Biological Sciences* **272**, 1633-1640 (2005).
43. H. E. Hoekstra, Genetics, development and evolution of adaptive pigmentation in vertebrates. *Heredity (Edinb).* **97**, 222–234 (2006).
44. D. Schwochow, *et al.*, The feather pattern *autosomal barring* in chicken is strongly associated with segregation at the *MC1R* locus. *Pigment Cell Melanoma Res.* **34**, 1015–1028 (2021).
45. S. Krishnan, R. L. Cryberg, Effects of mutations in pigeon *Mc1r* implicate an expanded plumage color patterning regulatory network. [Preprint] (2019). https://doi.org/10.1101/792945.
46. O. Vidal, J. Viñas, C. Pla, Variability of the melanocortin 1 receptor (*MC1R*) gene explains the segregation of the bronze locus in turkey (Meleagris gallopavo). *Poult. Sci.* **89**, 1599–1602 (2010).
47. T. Hirobe, Role of dermal factors involved in regulating the melanin and melanogenesis of mammalian melanocytes in normal and abnormal skin. *Int. J. Mol. Sci.* **25**, 4560 (2024).
48. L. Weiner, W. Fu, W. J. Chirico, J. L. Brissette, Skin as a living coloring book: how epithelial cells create patterns of pigmentation. *Pigment Cell Melanoma Res.* **27**, 1014–1031 (2014).
49. M. Giraldo, J. Sosa, D. Stavenga, Feather iridescence of *Coeligena* hummingbird species varies due to differently organized barbs and barbules. *Biol. Lett.* **17**, 20210190 (2021).
50. Y. Liu, *et al.*, Comparison of structural and chemical properties of black and red human hair melanosomes. *Photochem. Photobiol.* **81**, 135–144 (2005).
51. J. A. Brumbaugh, Ultrastructural differences between forming eumelanin and pheomelanin as revealed by the pink-eye mutation in the fowl. *Dev. Biol.* **18**, 375–390 (1968).
52. E. D. Enbody, *et al.*, A multispecies *BCO2* beak color polymorphism in the Darwin's finch radiation. *Current Biology* **31**, 5597-5604.e7 (2021).
53. D. E. Wood, S. L. Salzberg, Kraken: ultrafast metagenomic sequence classification using exact alignments. *Genome Biol.* **15**, R46 (2014).
54. S. Marco-Sola, M. Sammeth, R. Guigó, P. Ribeca, The GEM mapper: fast, accurate and versatile alignment by filtration. *Nat. Methods* **9**, 1185–1188 (2012).
55. N. C. Durand, *et al.*, Juicer provides a one-click system for analyzing loop-resolution Hi-C experiments. *Cell Syst.* **3**, 95–98 (2016).

56. A. V. Zimin, *et al.*, Hybrid assembly of the large and highly repetitive genome of *Aegilops tauschii* , a progenitor of bread wheat, with the MaSuRCA mega-reads algorithm. *Genome Res.* **27**, 787–792 (2017).
57. A. V. Zimin, *et al.*, The MaSuRCA genome assembler. *Bioinformatics* **29**, 2669–2677 (2013).
58. M. Kolmogorov, J. Yuan, Y. Lin, P. A. Pevzner, Assembly of long, error-prone reads using repeat graphs. *Nat. Biotechnol.* **37**, 540–546 (2019).
59. S. D. Jackman, *et al.*, Tigmint: correcting assembly errors using linked reads from large molecules. *BMC Bioinformatics* **19**, 393 (2018).
60. L. Coombe, *et al.*, ARKS: chromosome-scale scaffolding of human genome drafts with linked read kmers. *BMC Bioinformatics* **19**, 234 (2018).
61. R. L. Warren, *et al.*, LINKS: Scalable, alignment-free scaffolding of draft genomes with long reads. *Gigascience* **4** (2015).
62. O. Dudchenko, *et al.*, De novo assembly of the *Aedes aegypti* genome using Hi-C yields chromosome-length scaffolds. *Science (1979).* **356**, 92–95 (2017).
63. O. Dudchenko, *et al.*, The Juicebox Assembly Tools module facilitates *de novo* assembly of mammalian genomes with chromosome-length scaffolds for under $1000. [Preprint] (2018). https://doi.org/10.1101/254797.
64. G. Marçais, *et al.*, MUMmer4: A fast and versatile genome alignment system. *PLoS Comput. Biol.* **14**, e1005944 (2018).
65. F. A. Simão, R. M. Waterhouse, P. Ioannidis, E. V. Kriventseva, E. M. Zdobnov, BUSCO: Assessing genome assembly and annotation completeness with single-copy orthologs. *Bioinformatics* **31**, 3210–3212 (2015).
66. A. Dobin, *et al.*, STAR: ultrafast universal RNA-seq aligner. *Bioinformatics* **29**, 15–21 (2013).
67. M. Pertea, *et al.*, StringTie enables improved reconstruction of a transcriptome from RNA-seq reads. *Nat. Biotechnol.* **33**, 290–295 (2015).
68. Y. S. Niknafs, B. Pandian, H. K. Iyer, A. M. Chinnaiyan, M. K. Iyer, TACO produces robust multisample transcriptome assemblies from RNA-seq. *Nat. Methods* **14**, 68–70 (2017).
69. D. Mapleson, L. Venturini, G. Kaithakottil, D. Swarbreck, Efficient and accurate detection of splice junctions from RNA-seq with Portcullis. *Gigascience* **7** (2018).
70. B. J. Haas, Improving the Arabidopsis genome annotation using maximal transcript alignment assemblies. *Nucleic Acids Res.* **31**, 5654–5666 (2003).
71. O. Gotoh, Direct mapping and alignment of protein sequences onto genomic sequence. *Bioinformatics* **24**, 2438–2444 (2008).
72. M. Stanke, S. Waack, Gene prediction with a hidden Markov model and a new intron submodel. *Bioinformatics* **19**, ii215–ii225 (2003).
73. A. Lomsadze, V. Ter-Hovhannisyan, Y. O. Chernoff, M. Borodovsky, Gene identification in novel eukaryotic genomes by self-training algorithm. *Nucleic Acids Res.* **33**, 6494–6506 (2005).
74. B. J. Haas, *et al.*, Automated eukaryotic gene structure annotation using EVidenceModeler and the Program to Assemble Spliced Alignments. *Genome Biol.* **9**, R7 (2008).
75. A. Conesa, *et al.*, Blast2GO: a universal tool for annotation, visualization and analysis in functional genomics research. *Bioinformatics* **21**, 3674–3676 (2005).
76. S. F. Altschul, W. Gish, W. Miller, E. W. Myers, D. J. Lipman, Basic local alignment search tool. *J. Mol. Biol.* **215**, 403–410 (1990).
77. P. Jones, *et al.*, InterProScan 5: genome-scale protein function classification. *Bioinformatics* **30**, 1236–1240 (2014).
78. X. Cui, Z. Lu, S. Wang, J. Jing-Yan Wang, X. Gao, CMsearch: simultaneous exploration of protein sequence space and structure space improves not only protein homology detection but also protein structure prediction. *Bioinformatics* **32**, i332–i340 (2016).
79. E. P. Nawrocki, S. R. Eddy, Infernal 1.1: 100-fold faster RNA homology searches. *Bioinformatics* **29**, 2933–2935 (2013).
80. E. P. Nawrocki, *et al.*, Rfam 12.0: Updates to the RNA families database. *Nucleic Acids Res.* **43**, D130–D137 (2015).
81. T. M. Lowe, S. R. Eddy, tRNAscan-SE: A program for improved detection of transfer RNA genes in genomic sequence. *Nucleic Acids Res.* **25**, 955–964 (1997).
82. H. Li, R. Durbin, Fast and accurate short read alignment with Burrows-Wheeler transform. *Bioinformatics* **25**, 1754–1760 (2009).
83. H. Li, *et al.*, The Sequence Alignment/Map format and SAMtools. *Bioinformatics* **25**, 2078–2079 (2009).
84. A. McKenna, *et al.*, The genome analysis toolkit: A MapReduce framework for analyzing next-generation DNA sequencing data. *Genome Res.* **20**, 1297-1303 (2010).
85. P. Danecek, *et al.*, The variant call format and VCFtools. *Bioinformatics* **27**, 2156–2158 (2011).

86. P. Cingolani, *et al.*, A program for annotating and predicting the effects of single nucleotide polymorphisms, SnpEff. *Fly (Austin).* **6**, 80–92 (2012).
87. B. L. Browning, Y. Zhou, S. R. Browning, A One-Penny Imputed Genome from Next-Generation Reference Panels. *The American Journal of Human Genetics* **103**, 338–348 (2018).
88. B. L. Browning, X. Tian, Y. Zhou, S. R. Browning, Fast two-stage phasing of large-scale sequence data. *The American Journal of Human Genetics* **108**, 1880–1890 (2021).
89. X. Zhou, M. Stephens, Genome-wide efficient mixed-model analysis for association studies. *Nat. Genet.* **44**, 821–824 (2012).
90. S. Purcell, *et al.*, PLINK: A Tool Set for Whole-Genome Association and Population-Based Linkage Analyses. *The American Journal of Human Genetics* **81**, 559–575 (2007).
91. S. D. Turner, qqman: an R package for visualizing GWAS results using Q-Q and manhattan plots. *J. Open Source Softw.* **3**, 731 (2018).
92. D. Kim, J. M. Paggi, C. Park, C. Bennett, S. L. Salzberg, Graph-based genome alignment and genotyping with HISAT2 and HISAT-genotype. *Nat. Biotechnol.* **37**, 907–915 (2019).
93. M. I. Love, W. Huber, S. Anders, Moderated estimation of fold change and dispersion for RNA-seq data with DESeq2. *Genome Biol.* **15**, 550 (2014).
94. Y. Liao, G. K. Smyth, W. Shi, featureCounts: an efficient general purpose program for assigning sequence reads to genomic features. *Bioinformatics* **30**, 923–930 (2014).
95. Y. Liao, G. K. Smyth, W. Shi, The R package Rsubread is easier, faster, cheaper and better for alignment and quantification of RNA sequencing reads. *Nucleic Acids Res.* **47**, e47–e47 (2019).
96. P. Andrade, *et al.*, Regulatory changes in pterin and carotenoid genes underlie balanced color polymorphisms in the wall lizard. *PNAS* **116**, 5633–5642 (2019).
97. J. T. Robinson, *et al.*, Integrative genomics viewer. *Nat. Biotechnol.* **29**, 24-26 (2011).
98. J. Schanda, Ed., *Colorimetry* (Wiley, 2007).
99. C. A. Schneider, W. S. Rasband, K. W. Eliceiri, NIH Image to ImageJ: 25 years of image analysis. *Nat. Methods* **9**, 671–675 (2012).
100. B. Ripley, B. Venables, MASS: support functions and datasets for Venables and Ripley's MASS. *CRAN: contributed packages* [Preprint] (2009).
101. H. Ozeki, S. Ito, K. Wakamatsu, A. J. Thody, Spectrophotometric characterization of eumelanin and pheomelanin in hair. *Pigment Cell Res.* **9**, 265–270 (1996).
102. S. Ito, *et al.*, Usefulness of alkaline hydrogen peroxide oxidation to analyze eumelanin and pheomelanin in various tissue samples: application to chemical analysis of human hair melanins. *Pigment Cell Melanoma Res.* **24**, 605–613 (2011).
103. K. Wakamatsu, S. Ito, J. L. Rees, The usefulness of 4-amino-3-hydroxyphenylalanine as a specific marker of pheomelanin. *Pigment Cell Res.* **15**, 225–232 (2002).
104. M. d'Ischia, *et al.*, Melanins and melanogenesis: methods, standards, protocols. *Pigment Cell Melanoma Res.* **26**, 616–633 (2013).
105. S. Del Bino, *et al.*, Chemical analysis of constitutive pigmentation of human epidermis reveals constant eumelanin to pheomelanin ratio. *Pigment Cell Melanoma Res.* **28**, 707–717 (2015).
106. A. T. L. Lun, *et al.*, EmptyDrops: distinguishing cells from empty droplets in droplet-based single-cell RNA sequencing data. *Genome Biol.* **20**, 63 (2019).
107. Y. Hao, *et al.*, Integrated analysis of multimodal single-cell data. *Cell* **184**, 3573-3587.e29 (2021).
108. E. Cohen, C. Johnson, C. J. Redmond, R. R. Nair, P. A. Coulombe, Revisiting the significance of keratin expression in complex epithelia. *J. Cell Sci.* **135** (2022).
109. M. Nishimura, *et al.*, Extracellular cleavage of collagen XVII is essential for correct cutaneous basement membrane formation. *Hum. Mol. Genet.* **25**, 328–339 (2016).
110. M. Yu, P. Wu, R. B. Widelitz, C.-M. Chuong, The morphogenesis of feathers. *Nature* **420**, 308–312 (2002).
111. M. Inaba, C.-M. Chuong, Avian pigment pattern formation: developmental control of macro- (Across the Body) and micro- (within a feather) level of pigment patterns. *Front. Cell Dev. Biol.* **8** (2020).
112. V. Nataf, P. Mercier, C. Ziller, N. M. Le Douarin, Novel markers of melanocyte differentiation in the avian embryo. *Exp. Cell Res.* **207**, 171–182 (1993).
113. V. Nataf, *et al.*, Melanoblast/Melanocyte Early Marker (MelEM) Is a Glutathione S-Transferase Subunit. *Exp. Cell Res.* **218**, 394–400 (1995).
114. H. Cheng, G. T. Concepcion, X. Feng, H. Zhang, H. Li, Haplotype-resolved de novo assembly using phased assembly graphs with hifiasm. *Nat. Methods* **18**, 170–175 (2021).
115. M. Alonge, *et al.*, Automated assembly scaffolding using RagTag elevates a new tomato system for high-throughput genome editing. *Genome Biol.* **23**, 258 (2022).
116. A. Shumate, S. L. Salzberg, Liftoff: accurate mapping of gene annotations. *Bioinformatics* **37**, 1639–1643 (2021).

FIGURES

Figure 1. Mendelian color mutants in the Indian peafowl (*Pavo cristatus*). This figure illustrates the striking phenotypic effects of Mendelian color mutations on the overall appearance and eyespot coloration in peacocks. From left to right: wild-type, Ultramarine, Purple, Violet, Opal, Bronze, Cameo, Charcoal, and White. Additional photographs showing the full-body plumage phenotype of each color variety are provided in **fig. S1**.

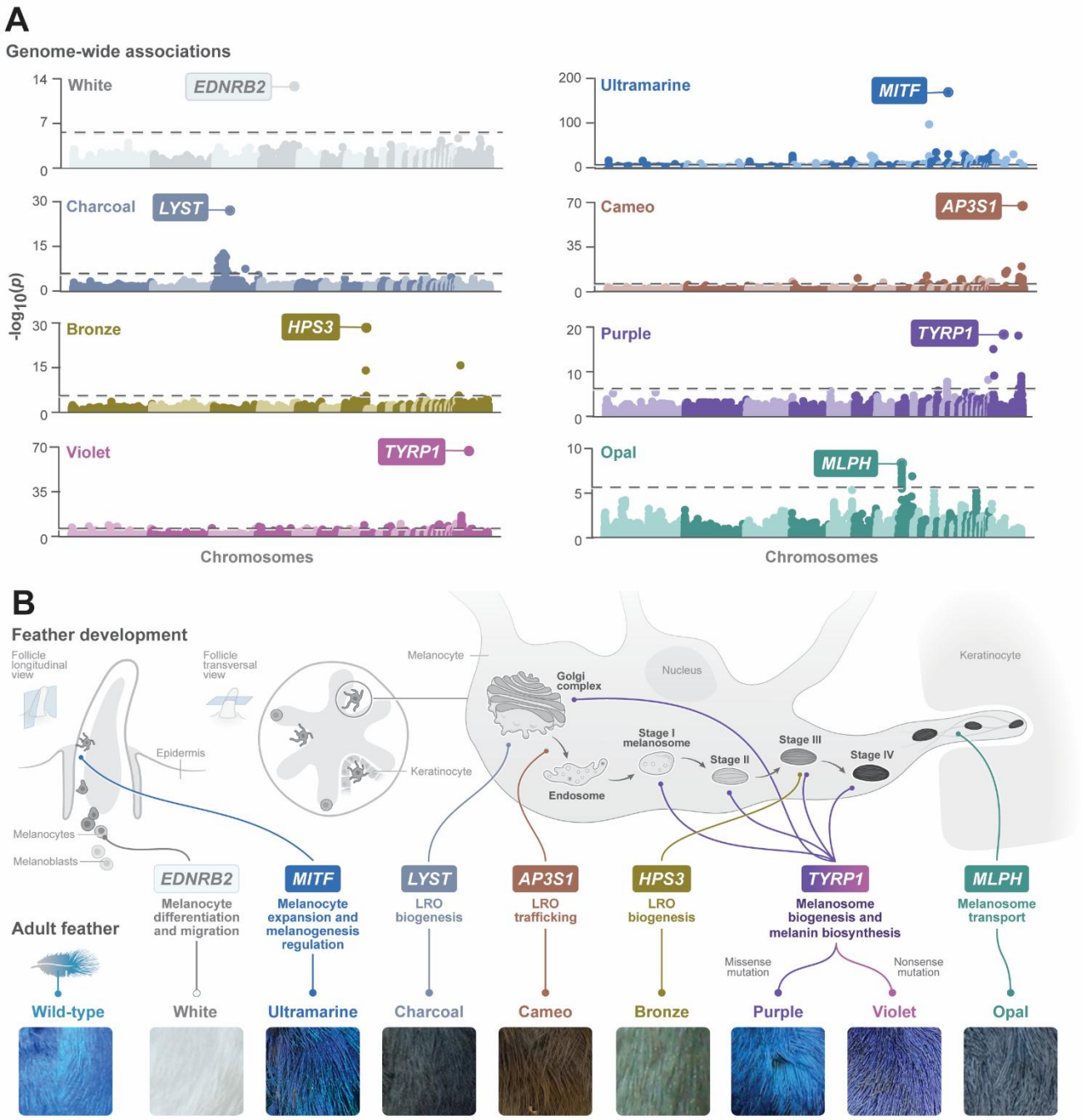

Figure 2. Genetic mapping of color variants. (A) Manhattan plots representing the genome-wide association analyses (GWAS) for plumage color. Each point represents a variant, with the *x*-axis showing genomic position (chromosomes in alternating colors, ordered according to the Indian peafowl reference genome) and the *y*-axis indicating statistical significance as $-\log_{10}(p)$. The horizontal dashed line indicates the Bonferroni-corrected genome-wide significance threshold. The most significantly associated variant in each plot is annotated with the name of the gene in which it resides. **(B)** Schematic overview of melanogenesis in feather development, highlighting candidate genes identified by GWAS. On the top left, longitudinal and cross-sectional views of a developing feather follicle depict the spatial arrangement of melanocytes during feather formation. In the center and top right, a melanocyte is illustrated with its key cellular components involved in melanogenesis, the melanosome maturation stages, and the dendritic projections connecting to keratinocytes, where melanosomes are finally deposited. Colored lines link genes to their respective subcellular locations and cellular processes associated with melanocytes, lysosome-related organelles (LRO), and melanosomes. *TYRP1* is associated with two phenotypes and the mutation type (e.g., missense, nonsense) is indicated. Along the bottom, magnified images of adult neck feathers (~2 × 2 cm) display the macroscopic color phenotypes corresponding to each mutation.

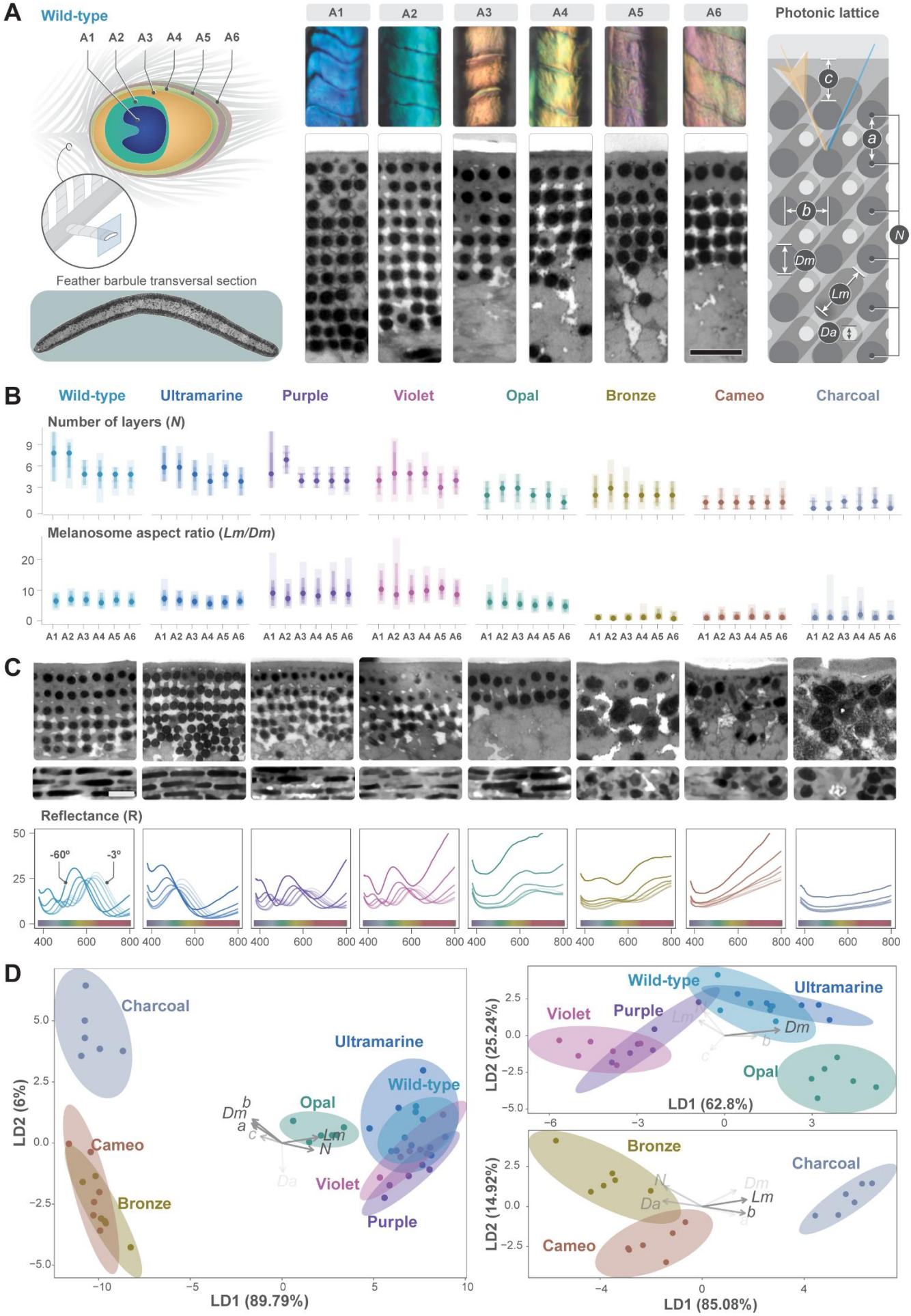
A
Wild-type
A1 A2 A3 A4 A5 A6
Feather barbule transversal section
Photonic lattice
c
a
b
N
Dm
Lm
Da
B
Wild-type
Ultramarine
Purple
Violet
Opal
Bronze
Cameo
Charcoal
Number of layers (N)
Melanosome aspect ratio (Lm/Dm)
C
Reflectance (R)
-60°
-3°
D
Charcoal
Ultramarine
Wild-type
Opal
Cameo
Bronze
Violet
Purple
LD1 (89.79%)
LD2 (6%)
LD1 (62.8%)
LD2 (25.24%)
LD1 (85.08%)
LD2 (14.92%)

Figure 3. Ultrastructural modifications and photonic impact in eyespot feathers. (A) Schematic representation of feather structure, sampling procedure, and measured parameters of the photonic lattice. Left: A diagram of the wild-type peacock eyespot, divided into six chromatic regions (A1–A6), alongside a transverse section of a feather barbule exemplifying the transmission electron microscopy (TEM) imaging used for structural analysis. Center: TEM images illustrating the ultrastructural arrangement of melanosomes across the six regions corresponding to different barbule colors in wild-type feathers (scale = 500 nm). Right: a 3D schematic representation of the key structural measurements from the photonic lattice of feather barbules, including: distance between melanosome layers (*a*); distance between melanosomes within layer (*b*); cortex thickness (*c*); melanosomes diameter (*Dm*); air pocket diameter (*Da*); number of melanosome layers (*N*) and length of melanosomes (*Lm*) (scale bar = 500 nm)**. (B)** Gradient plots illustrate differences in melanosome layer number (*N*) and aspect ratio (*Lm*/*Dm*) across A1–A6 in wild-type and mutants. Each circle represents an average measurement for a specific region, narrow bars represent quantile intervals at the 80% and 95% levels, and the wider bar represents the range of minimum and maximum for each area. Additional parameters are presented in **fig. S6**. **(C)** TEM of transversal (top) and longitudinal (bottom) cuts of feather barbules in A3 in wild-type and seven mutants (scale bar = 500 nm). Images for the remaining eyespot regions are available in **fig. S5**. Below, reflectance (R) profiles of A3 and variation (minimum–maximum) of the peak reflectance wavelength of the angle-dependent measurement from -60º to -3º (in increasing transparency). Measurements were taken at 10° intervals, with the exception of an additional measurement at −3° to capture the reflection near the surface normal. **(D)** Linear discriminant analyses (LDA) of structural measurements for all mutants on the left, and for iridescent (top) and non-iridescent (bottom) mutants on the right, with oval shading representing the variation per mutant across areas. The arrows represent the parameters explaining a significant amount of variance in LD1 of each analysis ($P < 0.01$), and the shading reflects their individual weight.

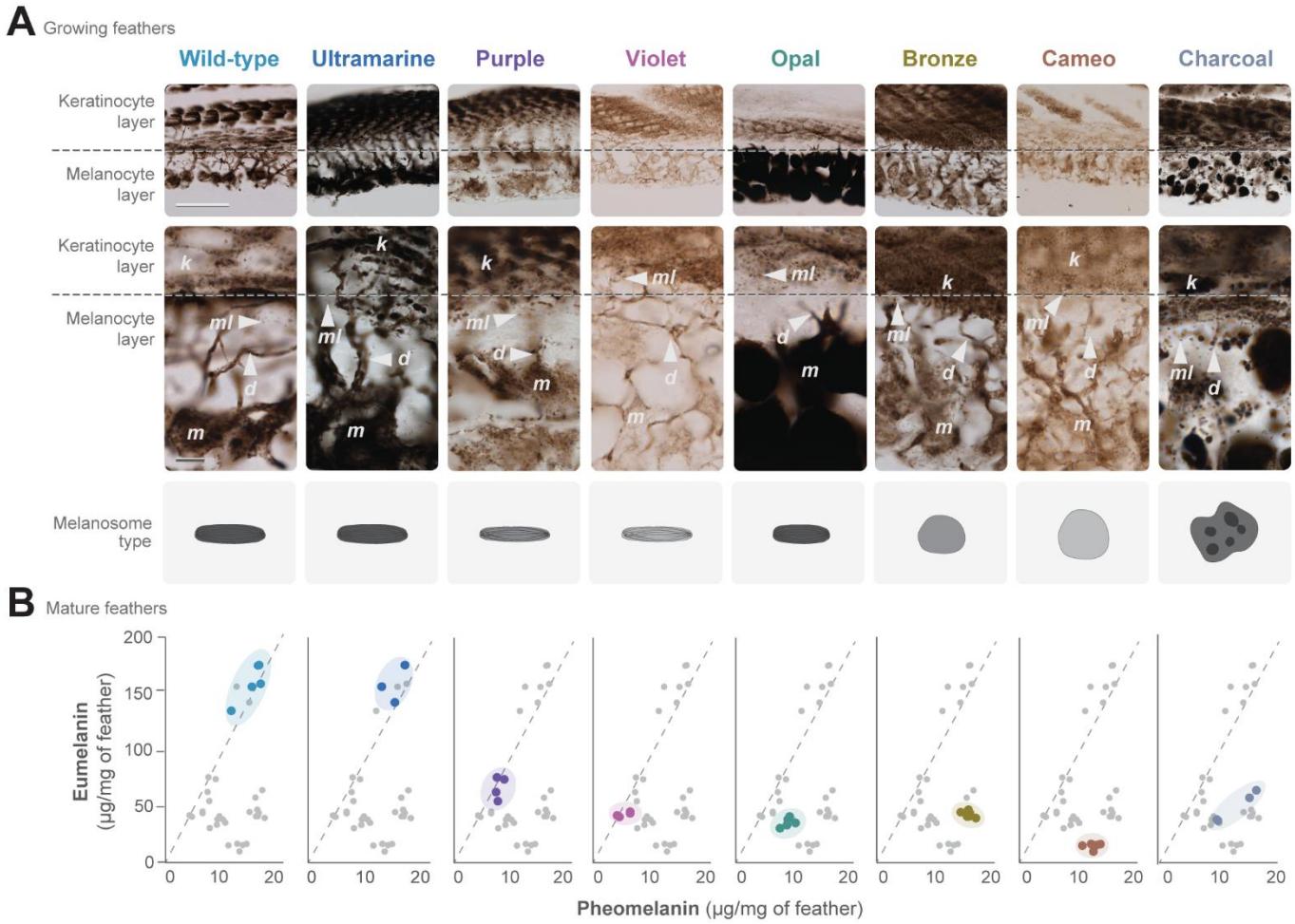

Figure 4. Histological and biochemical characterization of peafowl mutants. (**A**) Longitudinal sections of developing feather follicles of wild-type and mutant birds showing the organization of a melanocyte layer below the dashed line and a keratinocyte layer above the dashed line (top, scale bar = 50 µm). An enlarged view of the boundary between the two layers is shown (bottom, scale bar represents 10 µm), and various structures are highlighted: melanocytes (*m*), keratinocytes (*k*), dendrites (*d*), and melanosomes (*ml*). Across the bottom are schematic illustrations of melanosome morphology derived from TEM images (**fig. S5**). (**B**) Melanin quantification in mature neck feathers from wild-type and mutant phenotypes (detailed values provided in **table S6**). Graphs show quantification of pheomelanin (*x*-axis) and eumelanin (*y*-axis). All datapoints across all genotypes are plotted in each panel to enable direct visual comparison. Points belonging to the genotype shown in that panel are highlighted in color, while all other datapoints are shown in gray. The dashed line represents a eumelanin-to-pheomelanin ratio of 10:1.

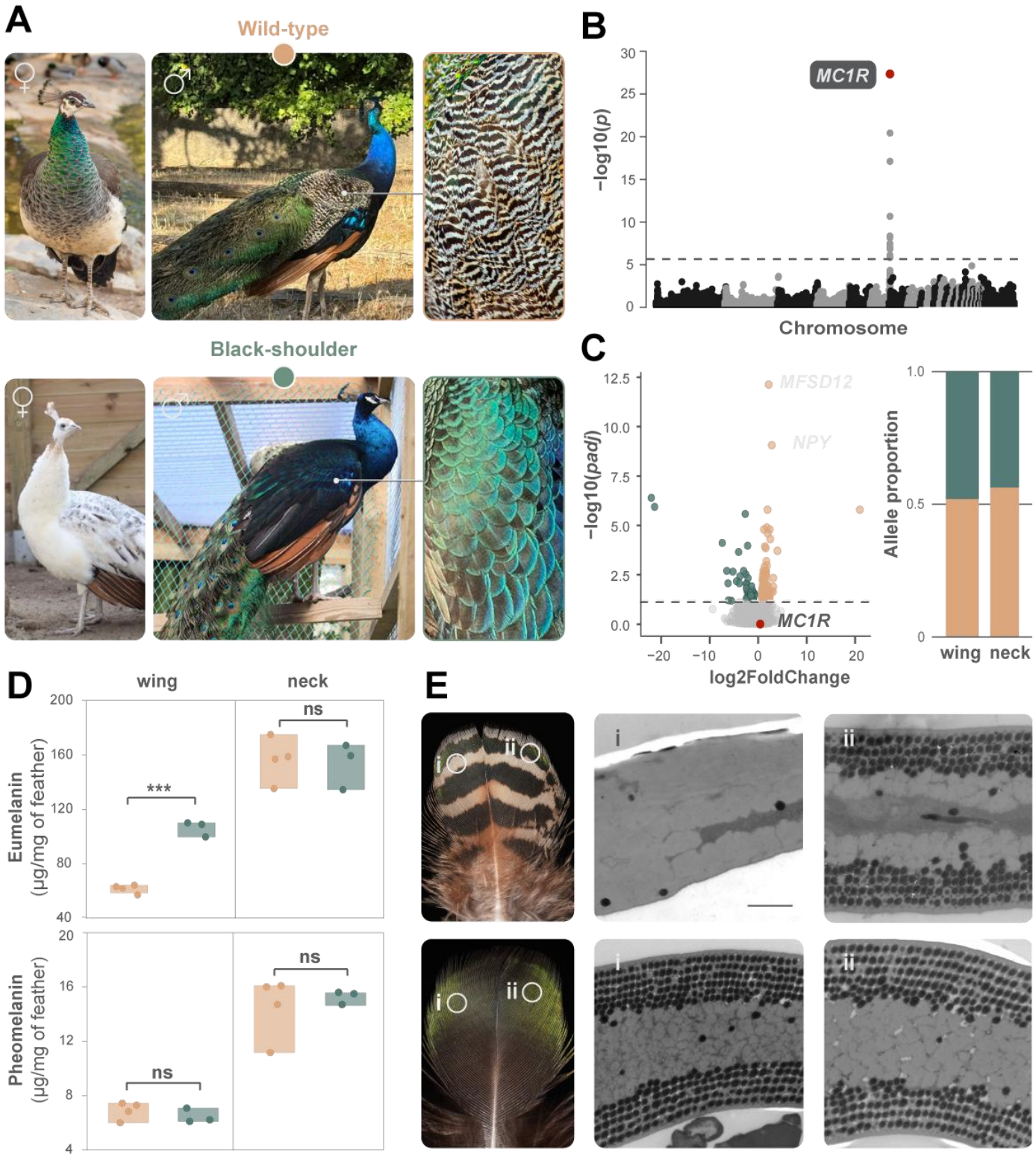

Figure 5. A patch-specific gain of iridescence. (A) Pictures illustrating wild-type (top) and Black-shoulder (bottom) peafowls, both females (peahens, left) and males (peacocks, center), and a close-up of peacock wing covert feathers (right). **(B)** Manhattan plot displaying whole-genome association results. Each dot represents the $-\log_{10}(p)$ value from the likelihood ratio test for a genetic variant. The red horizontal line indicates the Bonferroni-corrected genome-wide significance threshold. The strongest association corresponds to a missense mutation in *MC1R* (red circle). **(C)** Left panel: a volcano plot comparing RNA-seq expression profiles of regenerating feather follicles from the wing of wild-type ($n = 4$) and Black-shoulder ($n = 4$) males. The horizontal dashed line marks the significance threshold (FDR = 0.1). Green and beige circles represent genes upregulated in Black-shoulder and wild-type individuals, respectively. The red circle represents the *MC1R* gene. Significantly differentially expressed genes with known functions in melanogenesis are labeled in grey. Right panel: allelic imbalance analysis of the wild-type (beige) and Black-shoulder (green) *MC1R*

alleles in feather follicles from the wing and neck of male individuals heterozygous for the missense mutation associated with the Black-shoulder phenotype. **(D)** Comparisons of eumelanin (top) and pheomelanin (bottom) levels in wing and neck feathers of wild-type (beige) and Black-shoulder (green) male feathers (detailed values provided in **table S6**). Significant differences are indicated (*** $P < 0.001$), while "ns" denotes non-significant differences ($P > 0.05$), as determined by a two-sample *t*-test assuming unequal variances. **(E)** On the left, representative wing covert feathers from wild-type (top row) and Black-shoulder (bottom row) males, highlighting equivalent locations chosen for ultrastructural analyses of feather barbules. The center and right panels show TEM images of transversal cuts of feather barbules from the selected regions, illustrating melanosome organization, and where scale represents 1 μm and is maintained across figures.

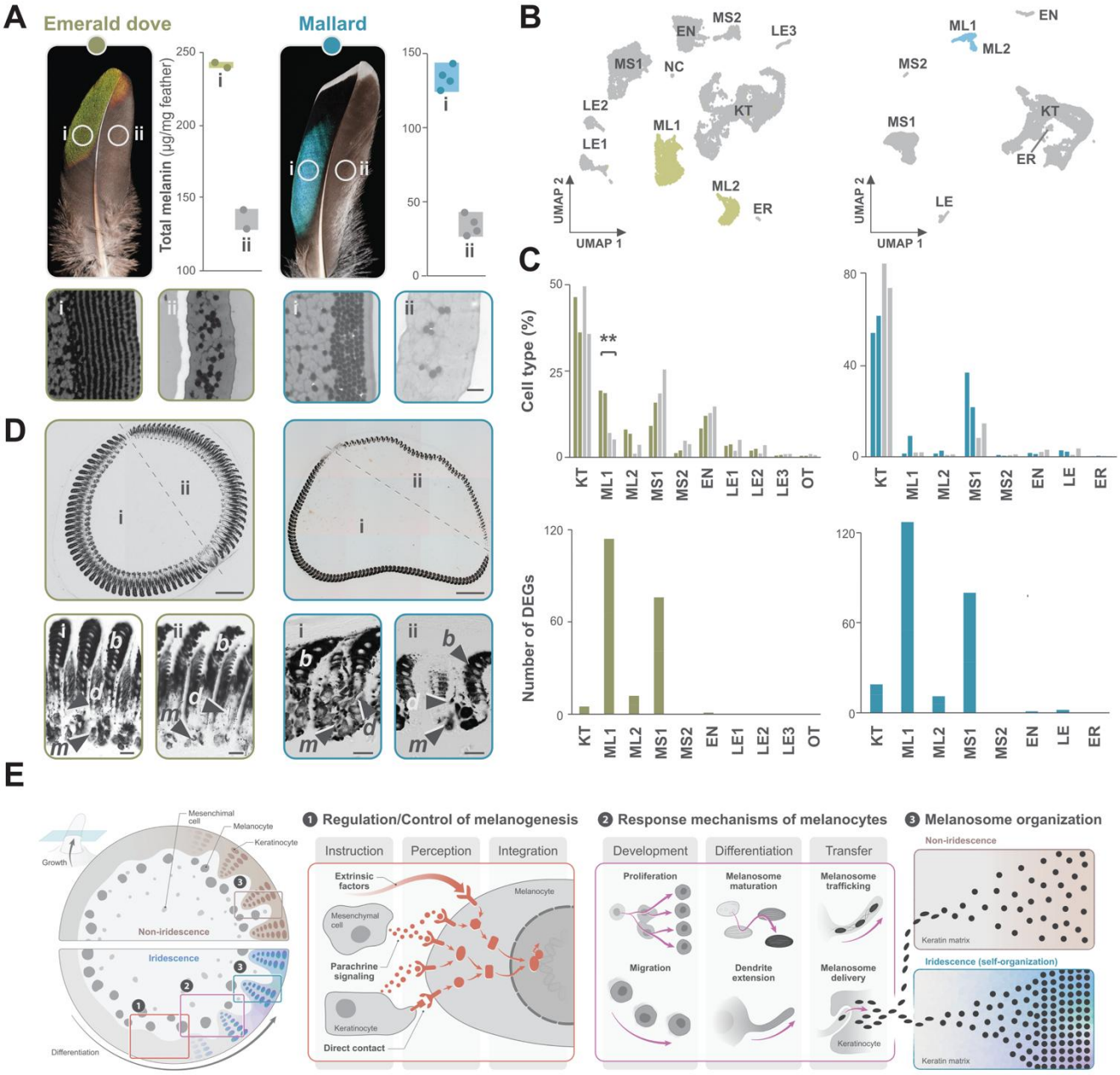

Figure 6. Modulation of iridescence via melanogenesis in wild bird species. The emerald dove (*Chalcophaps indica*) and the mallard duck (*Anas platyrhynchos*) develop asymmetric feathers containing both iridescent (i) and non-iridescent (ii) barbules. **(A)** *Top:* total melanin content per sample in each of the two feather regions. *Bottom:* TEM images of barbule cross-sections in iridescent and non-iridescent barbules (scale bar for all panels: 1 µm). **(B–C)** *scRNA-seq* of developing feathers from emerald dove (left) and mallard (right): ML, melanocytes; KT, keratinocytes; MS, mesenchymal cells; EN, endothelial cells; LE, leukocytes; ER, erythrocytes; NC, neural crest-derived cells; OT, others (ER+NC) **(B)** UMAP projections showing cell clustering. **(C)** *Top:* proportion of major cell types identified. *Bottom:* number of differentially expressed genes (DEGs) per cell type. **(D)** *Histological analyses* of developing feathers. *Top:* cross-sections of feathers showing overall morphology (scale bars: left = 200 µm; right = 500 µm). The dashed line indicates the boundary within the regenerating feather follicle separating regions that give rise to iridescent (i) and non-iridescent (ii) barbules. *Bottom*: high-magnification images of barb ridges (scale bar = 20 µm) reveal increased melanization in melanocytes (*m*) and their dendrites (*d*), associated with iridescent barbule keratinocytes (*b*). **(E)** Schematic summary of proposed mechanisms controlling iridescent feather color formation inferred from the scRNA-seq data. Cross-section representation of growing feathers developing

non-iridescent (top) or iridescent (bottom) colors. Throughout barbule differentiation, depicted as a gradient from left to right, melanocytes receive, perceive, and integrate environmental cues from neighboring cells and extrinsic factors (e.g., paracrine signals or growth factors) (1). These instructions modulate melanocyte behavior (2), and the resulting availability, shape, composition, and transfer of melanosomes influence their assembly into photonic structures (3).

SUPPLEMENTAL INFORMATION

Data S1. Differentially expressed genes (DEGs) per cell type between iridescent (n = 2 replicates) and non-iridescent barbules (n = 2 replicates) in the common emerald dove (*Chalcophaps indica*).

Data S2. Differentially expressed genes (DEGs) per cell type between iridescent (n = 2 replicates) and non-iridescent barbules (n = 2 replicates) in the mallard (*Anas platyrhynchos*).

Data S3. Top upregulated differentially expressed genes (DEGs) for each cell type in the common emerald dove (*Chalcophaps indica*) (n =10,213 cells; n = 12 cell types).

Data S4. Top upregulated differentially expressed genes (DEGs) for each cell type in the mallard (*Anas platyrhynchos*) (n = 20,991 cells; n = 9 cell types).

Data S5. Gene ontology (GO) enrichment analyses of melanocyte differentially expressed genes between barbule color types (iridescent vs. non-iridescent barbules) for the emerald dove (*Chalcophaps indica*) (adjusted P-value ≤ 0.1).

Data S6. Gene ontology (GO) enrichment analyses of melanocyte differentially expressed genes between barbule color types (iridescent vs. non-iridescent barbules) for the mallard (*Anas platyrhynchos*) (adjusted P-value ≤ 0.1).

Table S1. Genome assembly, annotation, and BUSCO statistics of the Indian peafowl genome

Genome assembly and sequencing statistics	
10x linked-reads	
Number of reads	262 153 402
Average coverage	60.03
Assembly size (bp)	372
Nanopore	
Number of reads	4 599 390
Average coverage	32.99
Contig N50 (kb)	16.62
Hi-C	
Number of reads	317 826 943
Number of contacts	261 213 953
Final assembly	
Assembly size (Gb)	1.04
Contig N50 (Mb)	3.57
Contig L50	86
Scaffolds	813
Scaffold N50 (Mb)	93.07
Scaffold L50	4
Genome annotation report	
Number of protein-coding genes	21 618
Median gene length (bp)	9 416
Number of transcripts	32 889
Number of exons	224 330
Number of coding exons	213 541
Coding GC content	52.62%
Median UTR length (bp)	1692
Median intron length (bp)	749
Exons per transcript	11.07
Transcripts per gene	1.52
Multi-exonic transcripts	0.92
Gene density (genes/Mb)	20.85
BUSCO analysis (8,338 avian genes; aves_odb10)	
Complete (%)	96.2
singleton (%)	95.8
duplicated (%)	0.4
Fragmented (%)	0.8
Missing (%)	3.0

Table S2. List of genes and mutations associated with the Indian peafowl varieties.

Variety	Gene	Acronym	Position	Type[a]	Protein change[b]	Evolutionary conservation (*n* = species)[c]
Mendelian						
Charcoal	*Lysosomal trafficking regulator*	*LYST*	3:38,734,068	Missense	Arg1556His	99% (135)
White	*Endothelin receptor B subtype 2*	*EDNRB2*	4:80,919,920	Nonsense	Trp206*	
Black-shoulder	*Melanocortin 1 receptor*	*MC1R*	6:53,715,975	Frameshift (Δ1)	Ser165Ala	
Black-shoulder	*Melanocortin 1 receptor*	*MC1R*	6:53,716,234	Missense	Trp251Arg	100% (47)
Bronze	*Hermansky-Pudlak syndrome type 3*	*HPS3*	7:53,510,213	Insertion (Δ12)	Cys524*	
Opal	*Melanophilin*	*MLPH*	8:34,112,863	Deletion (Δ483)	Ser245Gly	
Ultramarine	*Microphthalmia-associated transcription factor*	*MITF*	10:15,139,593	Missense	Glu205Lys	100% (139)
Purple	*Tyrosinase-related protein 1 enzyme*	*TYRP1*	Z:31,260,949	Missense	Phe243Ser	100% (288)
Violet	*Tyrosinase-related protein 1 enzyme*	*TYRP1*	Z:31,264,368	Nonsense	Arg373*	
Cameo	*Adaptor-related protein complex 3 sigma 1 subunit*	*AP3S1*	Z:74,408,869	Missense	Leu71Phe	100% (129)
Combinations of mutations[d]						
Taupe		Purple + *MLPH*	8:34,104,916	*nonsense*	Arg581*	
Hazel		Bronze + Purple				
Raw-umber		Cameo + Opal				
Peach		Cameo + Purple				

[a]The delta (Δ) represents the size of the insertion or deletion
[b]The asterisk represents mutations that give rise to premature STOP codons
[c]The proportion of amino acid residues that match the wild-type allele across whole-genome alignments of proteins across birds. In parentheses, the number of species included in the alignment are given.
[d]Color varieties resulting from combinations of loci are identified by the mutants they derive from, with the exception of *taupe* where another *MLPH* mutation contributes to the phenotype.

Table S3. Quantification of structural parameters in feather barbules across eyespot regions.

		N[a]		*a*[b]		*b*[c]		*c*[d]		*Dm*[e]		*Da*[f]		*Lm*[g]				
Phenotype	**Area**	**Mean**	**SD**	**Mean**	**SD**	**Mean**	**SD**	**Mean**	**SD**	**Mean**	**SD**	**Mean**	**SD**	**Mean**	**SD**	**Aspect ratio[h]**	**Chroma[i]**	**HEX[j]**
Wild-type	1	7.7	1.8	147.4	15.0	225.4	18.4	97.5	14.8	105.8	11.8	39.0	11.6	692.7	100.6	6.6	54.7	#007C7F
Wild-type	2	7.5	1.4	174.0	12.8	158.3	17.2	101.4	9.5	106.1	9.5	52.3	14.3	763.4	115.9	7.3	70.3	#00804D
Wild-type	3	5.4	1.0	198.7	21.7	178.9	21.7	141.0	14.6	110.8	10.5	48.9	15.0	769.9	105.0	7.0	32.8	#91643C
Wild-type	4	5.3	1.2	200.5	26.3	166.1	20.4	130.9	10.2	116.3	10.9	64.6	11.2	723.7	111.9	6.3	42.7	#A47E39
Wild-type	5	4.7	0.9	197.2	32.8	177.6	20.5	112.9	18.1	114.7	9.5	55.8	12.9	798.1	126.1	7.0	25.5	#775071
Wild-type	6	4.6	0.9	191.9	38.2	162.1	14.1	130.5	16.1	119.9	9.6	65.9	12.9	778.8	126.1	6.5	19.9	#8A5E6A
Ultramarine	1	6.3	1.6	148.1	15.3	149.7	21.0	83.2	12.0	103.8	8.4	57.3	14.0	765.8	112.6	7.5	26.1	#2A2273
Ultramarine	2	5.8	1.4	159.0	15.5	153.6	15.5	88.6	11.1	108.5	9.8	49.9	12.4	738.5	116.2	6.9	35.2	#004476
Ultramarine	3	4.9	1.1	199.0	34.8	143.1	18.5	122.4	14.1	115.8	9.2	58.7	16.5	740.5	101.2	6.4	13.2	#526554
Ultramarine	4	4.4	1.1	177.5	28.2	150.2	19.3	100.0	14.2	119.6	7.9	36.2	10.8	691.3	115.7	5.8	35.2	#5A8853
Ultramarine	5	4.9	0.8	179.2	20.6	160.1	16.2	109.3	13.0	120.5	10.4	38.1	13.8	748.1	116.1	6.3	36.5	#387546
Ultramarine	6	4.1	1.2	200.8	25.1	162.4	15.4	110.7	17.9	127.6	11.7	32.6	12.5	837.8	108.3	6.6	39.2	#547738
Purple	1	5.8	2.1	179.9	30.3	157.6	19.6	109.0	18.9	86.7	14.2	60.6	15.8	766.4	134.3	9.1	26.1	#004869
Purple	2	7.2	1.0	180.9	22.0	162.6	22.3	104.8	13.8	96.5	16.5	57.0	17.2	713.0	118.5	7.6	50.3	#007866
Purple	3	4.5	0.6	196.5	37.0	145.8	23.4	141.5	34.7	78.3	13.3	55.2	17.3	707.1	129.6	9.3	16.5	#7B5F4E
Purple	4	4.5	0.8	187.2	31.3	140.0	23.2	140.4	19.3	83.0	12.6	63.8	18.7	700.5	149.5	8.7	27.4	#BD8556
Purple	5	4.3	0.9	194.6	47.6	155.7	26.8	132.0	19.9	88.6	13.7	57.4	20.1	818.8	182.0	9.4	4.9	#685D5C
Purple	6	4.4	1.0	195.2	32.2	153.5	33.4	129.6	18.9	87.8	15.6	65.3	19.8	765.0	136.0	9.0	4.9	#6A5F5F
Violet	1	3.8	1.1	123.5	30.6	117.1	16.5	92.4	14.3	74.4	11.0	28.4	14.2	784.2	131.1	10.8	18.6	#2D324D
Violet	2	5.7	2.1	172.2	27.1	159.8	29.6	117.0	19.8	71.0	12.3	35.0	8.4	633.7	196.7	9.2	30.6	#506E1E
Violet	3	4.6	1.1	206.2	46.3	150.0	18.9	162.3	29.7	78.3	12.2	44.9	13.4	728.1	120.9	9.5	12.2	#695449
Violet	4	4.7	1.0	171.2	33.2	154.2	29.7	140.2	17.7	81.0	13.6	54.0	14.3	790.3	123.3	10.0	14.4	#667B68
Violet	5	3.4	1.2	181.3	38.0	143.4	22.5	165.9	21.6	84.4	11.3	44.0	14.4	869.8	120.3	10.4	12.5	#5C4755
Violet	6	4.0	0.9	183.1	30.3	138.4	21.2	134.1	15.1	88.7	12.5	47.8	15.4	774.6	155.0	8.9	21.7	#42684F
Opal	1	1.7	1.1	196.7	21.2	168.7	22.5	114.0	25.5	107.0	16.5	29.6	11.0	654.5	104.7	6.3	11.8	#1B3741
Opal	2	2.9	1.0	196.7	21.2	168.6	22.6	107.6	22.6	107.0	16.5	29.7	11.0	654.1	105.4	6.3	24.5	#2D563A
Opal	3	2.7	1.1	210.2	28.1	173.1	23.0	131.3	23.4	122.3	14.2	46.4	18.5	697.7	118.7	5.8	9.6	#422F34
Opal	4	2.1	0.7	220.3	25.2	174.5	21.7	134.3	18.5	119.8	12.8	42.5	15.5	630.0	108.4	5.3	19.1	#623A3A
Opal	5	2.1	1.1	214.4	37.3	169.0	23.2	141.1	23.9	119.9	15.5	47.7	15.1	685.8	109.1	5.8	18.0	#663833
Opal	6	0.8	0.8	216.5	26.3	199.5	33.3	166.8	24.1	132.7	16.9	51.8	22.8	653.7	98.7	5.0	9.2	#493833
Bronze	1	1.9	1.1	232.8	49.1	237.5	46.5	82.3	35.2	156.5	44.9	46.2	26.3	187.6	39.9	1.3	1.5	#373633

Bronze	2	3.1	1.3	264.5	46.2	249.0	48.9	146.5	33.7	176.7	35.2	75.7	26.5	190.1	50.1	1.1	2.3	#3A3639
Bronze	3	1.7	1.0	285.9	69.6	294.3	68.7	183.3	38.6	183.9	38.4	73.2	31.0	226.0	67.1	1.3	6.9	#42493F
Bronze	4	2.0	0.8	284.8	64.4	232.2	56.4	177.0	32.8	152.3	37.7	62.1	26.5	201.4	65.9	1.4	3.8	#3B3F3A
Bronze	5	1.9	0.9	228.5	41.7	199.1	42.4	135.7	34.7	130.8	34.5	55.9	20.5	234.7	88.3	1.9	5.2	#3A4440
Bronze	6	1.9	1.0	303.2	57.8	246.5	53.2	175.5	36.2	180.8	47.5	51.2	20.7	174.0	67.7	1.1	1.7	#3A3D3D
Cameo	1	0.6	0.7	604.8	433.4	525.7	316.9	88.9	37.3	133.5	24.2	42.5	14.0	160.7	55.3	1.3	1.0	#3F3D3E
Cameo	2	0.8	0.8	319.5	193.3	300.2	205.6	167.1	38.8	132.9	30.6	49.3	14.0	197.2	80.1	1.6	1.9	#3D3938
Cameo	3	0.8	0.8	313.9	134.9	264.3	127.5	160.8	46.8	127.5	32.2	41.8	17.8	186.1	56.4	1.5	1.5	#413F3D
Cameo	4	0.8	0.7	280.2	86.6	281.4	130.5	163.8	48.8	130.3	37.0	64.5	26.4	210.6	87.9	1.8	4.0	#49443F
Cameo	5	0.8	0.8	301.4	104.7	289.9	121.9	170.5	37.8	152.0	29.8	59.0	17.7	229.2	53.1	1.6	3.4	#433E3A
Cameo	6	1.0	0.9	359.4	169.7	347.9	150.7	178.3	47.7	160.7	37.0	51.1	17.0	215.0	59.8	1.4	3.2	#3F3936
Charcoal	1	0.5	0.6	388.2	211.2	491.4	255.6	148.0	47.4	189.1	62.3	44.9	22.9	251.1	122.8	1.5	1.5	#343131
Charcoal	2	0.3	0.6	397.2	248.7	448.6	318.9	201.4	51.7	200.2	86.3	40.6	21.9	271.6	115.5	1.7	2.6	#332D2C
Charcoal	3	0.6	0.6	354.5	202.8	457.1	256.4	148.8	49.6	215.9	78.5	35.0	16.3	274.7	151.0	1.5	2.7	#322D2B
Charcoal	4	0.6	0.9	458.7	401.3	483.5	326.2	192.3	70.7	152.5	72.5	31.4	20.7	308.3	143.4	2.5	1.8	#33302E
Charcoal	5	0.8	0.9	467.1	333.9	536.7	339.4	180.6	42.7	206.6	66.8	28.8	11.7	270.8	104.4	1.5	1.1	#363433
Charcoal	6	0.3	0.6	663.0	428.8	387.2	215.6	162.1	45.5	227.2	68.6	38.5	16.5	315.8	110.4	1.6	1.9	#373332

[a]Number of melanosome layers
[b]Distance between layers
[c]Distance between melanosomes within a layer
[d]Cortex thickness
[e]Melanosome diameter
[f]Air pocket diameter
[g]Melanosome length
[h]Calculated as the ratio of melanosome length (*Lm*) and diameter (*Dm*)
[i]Measure of color saturation or intensity
[j]RGB-based hexadecimal color code

Table S4. Linear discriminant analysis (LDA) per group (all mutants, iridescent, and non-iridescent).

	All mutants				Iridescent				Non-iridescent	
	LD1	**LD2**	**LD3**	**LD4**	**LD1**	**LD2**	**LD3**	**LD4**	**LD1**	**LD2**
Variance explained[a]										
	0.899	0.060	0.024	0.014	0.628	0.252	0.095	0.024	0.851	0.149
Pearson's *r*[b]										
N[d]	0.852	0.146	**-0.395**	-0.221	-0.341	**0.807**	0.198	-0.056	-0.746	**0.642**
a[e]	-0.768	-0.383	0.103	-0.255	0.381	-0.414	0.345	-0.068	0.634	-0.252
b[f]	-0.804	-0.489	0.038	**-0.289**	0.543	-0.020	0.356	**-0.723**	0.836	-0.213
c[g]	-0.580	-0.138	0.218	-0.186	-0.232	-0.487	0.081	-0.402	0.318	-0.006
Dm[h]	-0.823	-0.405	-0.330	0.145	**0.941**	0.194	-0.019	-0.118	0.663	0.510
Da[i]	0.022	**0.594**	-0.413	-0.291	-0.204	0.311	**0.704**	0.104	-0.765	0.172
Lm[j]	**0.986**	-0.115	0.057	0.058	-0.432	0.512	-0.119	0.020	**0.865**	0.213
***P*-value**[c]										
N	1.58E-14	3.22E-01	**5.50E-03**	1.32E-01	6.53E-02	**7.29E-08**	2.94E-01	7.67E-01	3.78E-04	**4.04E-03**
a	1.88E-10	7.26E-03	4.87E-01	8.03E-02	3.79E-02	2.28E-02	6.21E-02	7.22E-01	4.75E-03	3.12E-01
b	6.13E-12	4.23E-04	7.98E-01	**4.61E-02**	1.93E-03	9.15E-01	5.37E-02	**6.50E-06**	1.55E-05	3.97E-01
c	1.59E-05	3.48E-01	1.37E-01	2.06E-01	2.17E-01	6.30E-03	6.69E-01	2.77E-02	1.99E-01	9.82E-01
Dm	7.06E-13	4.26E-03	2.18E-02	3.26E-01	**1.18E-14**	3.04E-01	9.22E-01	5.35E-01	2.72E-03	3.06E-02
Da	8.83E-01	**8.39E-06**	3.50E-03	4.50E-02	2.79E-01	9.40E-02	**1.41E-05**	5.86E-01	2.16E-04	4.94E-01
Lm	**1.25E-37**	4.35E-01	7.02E-01	6.93E-01	1.71E-02	3.82E-03	5.30E-01	9.18E-01	**3.53E-06**	3.95E-01

Numbers in bold represent the top correlated variable with the respective axis, for axes explaining above 5% of variance

[a]Proportion of the total between-group variance

[b]Correlation

[c]Significance of mean values of each photonic lattice parameter per area per mutant (Z-score standardized) with LDA axes

[d]Number of melanosome layers

[e]Distance between layers

[f]Distance between melanosomes within a layer

[g]Cortex thickness

[h]Melanosome diameter

[i]Air pocket diameter

[j]Melanosome length

Table S5. Proportion of variance explained per variable and phenotype relative to wild-type in linear discriminant analysis (LDA).

	Ultramarine		Purple		Violet		Opal		Bronze		Cameo		Charcoal	
	Pearson's *r*	*P*-value	Pearson's *r*	*P*-value	Pearson's *r*	*P*-value	Pearson's *r*	*P*-value	Pearson's *r*	*P*-value	Pearson's *r*	*P*-value	Pearson's *r*	*P*-value
N[a]	-0.385	2.16E-01	-0.323	3.06E-01	**-0.589**	**4.41E-02**	**-0.868**	**1.13E-04**	**-0.895**	**8.46E-05**	**-0.943**	**4.42E-06**	**-0.949**	**2.61E-06**
a[b]	-0.216	4.99E-01	0.146	6.51E-01	-0.265	4.04E-01	**0.638**	**2.69E-02**	**0.866**	**2.70E-04**	**0.748**	**5.13E-03**	**0.882**	**1.48E-04**
b[c]	**-0.659**	**1.96E-02**	**-0.624**	**3.01E-02**	**-0.683**	**1.43E-02**	-0.083	8.27E-01	**0.789**	**2.27E-03**	**0.771**	**3.29E-03**	**0.972**	**1.24E-07**
c[d]	-0.537	7.19E-02	0.235	4.61E-01	0.361	2.49E-01	0.362	2.54E-01	0.497	1.00E-01	**0.598**	**4.00E-02**	**0.822**	**1.05E-03**
Dm[e]	0.291	3.59E-01	**-0.948**	**2.83E-06**	**-0.956**	**1.27E-06**	0.319	2.31E-01	**0.882**	**1.46E-04**	**0.822**	**1.03E-03**	**0.931**	**1.13E-05**
Da[f]	-0.457	1.36E-01	0.375	2.29E-01	-0.571	5.27E-02	**-0.581**	**4.05E-02**	0.300	3.43E-01	-0.173	5.90E-01	**-0.766**	**3.70E-03**
Lm[g]	-0.011	9.74E-01	-0.122	7.06E-01	0.080	8.04E-01	**-0.808**	**5.29E-04**	**-0.997**	**2.18E-12**	**-0.996**	**5.50E-12**	**-0.994**	**6.05E-11**

Significant values are represented in bold

[a]Number of melanosome layers

[b]Distance between layers

[c]Distance between melanosomes within a layer

[d]Cortex thickness

[e]Melanosome diameter

[f]Air pocket diameter

[g]Melanosome length

Table S6. Quantification of melanin in mature feathers of wild-type and mutant peacocks.

			S-350 (/mg)[a]		AHPO (ng/mg)[b]			HI (ng/mg)[c]		TM[d]	EM[e]	BZ[f]	BT[g]	PM[h]
Sample	**Region**	**Pheno**	**A500**	**A650**	**PTCA**	**PDCA**	**TTCA**	**4-AHP**	**3-AHP**	**(µg/mg)**	**(µg/mg)**	**(µg/mg)**	**(µg/mg)**	**(µg/mg)**
peacock247	Neck	Wild-type	1.851	0.601	1985	277	465	39	96	187	159	15.8	0.4	16.2
peacock411	Neck	Wild-type	2.229	0.749	2188	288	451	37	66	225	175	15.3	0.3	15.7
peacock282	Neck	Wild-type	1.820	0.571	1952	235	427	18	19	184	156	14.5	0.2	14.7
peacock479	Neck	Wild-type	1.593	0.498	1685	248	326	11	16	161	135	11.1	0.1	11.2
peacock506	Neck	Ultramarine	2.141	0.745	2193	234	458	34	96	216	175	15.6	0.3	15.9
peacock510	Neck	Ultramarine	1.963	0.657	1779	193	409	34	175	198	142	13.9	0.3	14.2
peacock520	Neck	Ultramarine	1.519	0.491	1955	183	350	19	66	153	156	11.9	0.2	12.1
peacock197	Neck	Purple	1.063	0.344	947	200	198	63	30	107	76	6.7	0.6	7.3
peacock236	Neck	Purple	0.944	0.292	927	205	228	86	54	95	74	7.8	0.8	8.5
peacock314	Neck	Purple	0.843	0.260	684	167	202	64	46	85	55	6.9	0.6	7.4
peacock316	Neck	Purple	0.857	0.276	784	154	192	69	44	87	63	6.5	0.6	7.1
peacock274	Neck	Violet	0.617	0.191	549	128	161	93	50	62	44	5.5	0.8	6.3
peacock278	Neck	Violet	0.638	0.194	567	127	164	83	50	64	45	5.6	0.7	6.3
peacock150	Neck	Violet	0.413	0.122	508	108	126	23	21	42	41	4.3	0.2	4.5
peacock476	Neck	Violet	0.448	0.134	525	104	115	21	23	45	42	3.9	0.2	4.1
peacock239	Neck	Opal	0.532	0.176	481	56	249	40	34	54	38	8.5	0.4	8.8
peacock249	Neck	Opal	0.397	0.129	384	54	214	27	30	40	31	7.3	0.2	7.5
peacock302	Neck	Opal	0.524	0.172	442	63	278	77	44	53	35	9.5	0.7	10.1
peacock238	Neck	Opal	0.561	0.186	513	74	257	45	35	57	41	8.7	0.4	9.1
peacock306	Neck	Opal	0.500	0.165	420	61	242	56	39	51	34	8.2	0.5	8.7
peacock174	Neck	Bronze	0.579	0.193	496	69	322	653	215	58	40	10.9	5.9	16.8
peacock192	Neck	Bronze	0.671	0.221	551	81	319	552	177	68	44	10.8	5.0	15.8
peacock196	Neck	Bronze	0.581	0.187	514	72	292	601	185	59	41	9.9	5.4	15.3
peacock175	Neck	Bronze	0.750	0.248	562	100	303	440	154	76	45	10.3	4.0	14.3
peacock284	Neck	Bronze	0.642	0.207	515	76	307	582	202	65	41	10.4	5.2	15.7
peacock286	Neck	Bronze	0.768	0.256	588	92	319	526	179	78	47	10.8	4.7	15.6
peacock189	Neck	Cameo	0.227	0.072	195	28	188	745	228	23	16	6.4	6.7	13.1
peacock191	Neck	Cameo	0.191	0.056	191	27	143	648	188	19	15	4.9	5.8	10.7
peacock224	Neck	Cameo	0.178	0.049	125	25	196	655	238	18	10	6.7	5.9	12.6
peacock297	Neck	Cameo	0.237	0.069	209	32	183	660	223	24	17	6.2	5.9	12.2
peacock295	Neck	Cameo	0.239	0.070	206	32	203	762	249	24	16	6.9	6.9	13.8
peacock234	Neck	Charcoal	0.794	0.256	804	102	461	85	38	80	64	15.7	0.8	16.4
peacock265	Neck	Charcoal	0.483	0.156	479	65	275	43	19	49	38	9.4	0.4	9.7

peacock266	Neck	Charcoal	0.530	0.171	494	68	261	33	17	54	40	8.9	0.3	9.2
peacock508	Neck	Charcoal	0.682	0.223	722	76	369	304	110	69	58	12.5	2.7	12.8
peacock332	Neck	Black-shoulder	1.853	0.615	1673	248	425	37	94	187	134	14.5	0.3	14.7
peacock337	Neck	Black-shoulder	1.889	0.625	1939	283	450	28	92	191	155	15.3	0.2	15.5
peacock237	Neck	Black-shoulder	2.059	0.689	2080	282	463	37	73	208	166	15.7	0.3	16.0
peacock247	Wing	Wild-type	0.672	0.210	802	119	180	188	88	68	64	6.1	1.7	7.8
peacock427	Wing	Wild-type	0.595	0.185	774	114	168	43	40	60	62	5.7	0.4	6.1
peacock411	Wing	Wild-type	0.594	0.186	796	107	172	112	38	60	64	5.8	1.0	6.9
peacock282	Wing	Wild-type	0.607	0.194	717	97	190	74	27	61	57	6.5	0.7	7.1
peacock332	Wing	Black-shoulder	1.249	0.392	1247	199	180	15	63	126	100	6.1	0.1	6.3
peacock337	Wing	Black-shoulder	1.227	0.378	1376	206	205	16	55	124	110	7.0	0.1	7.1
peacock237	Wing	Black-shoulder	1.223	0.382	1362	204	177	13	35	124	109	6.0	0.1	6.1

[a]Soluene-350 solubilization
[b]Alkaline hydrogen peroxide oxidation
[c]Hydroiodic acid hydrolysis
[d]Total melanin (A500 × 101)
[e]Eumelanin (PTCA × 0.080)
[f]Benzothiazole (TTCA × 0.034)
[g]Benzothiazine (4-AHP × 0.009)
[h]Pheomelanin (BZ + BT)

Table S7. Statistics from whole-genome sequencing of peafowl individuals.

ID	Species	Body color phenotype	Wing phenotype	Coverage	Number of reads	Mapped reads (%)	Properly paired (%)
peacock001	*Pavo cristatus*	bronze		8.3	71 989 677	99.0	98.8
peacock002	*Pavo cristatus*	bronze		9.1	76 720 800	98.8	96.3
peacock003	*Pavo cristatus*	bronze	black-shoulder	9.5	78 832 417	98.9	95.9
peacock004	*Pavo cristatus*	bronze	black-shoulder	9.8	84 976 525	98.9	96.2
peacock005	*Pavo cristatus*	bronze	black-shoulder	11.2	95 514 878	98.5	96.1
peacock006	*Pavo cristatus*	bronze		9.7	82 144 664	98.6	95.1
peacock007	*Pavo cristatus*	bronze		10.8	90 931 068	98.6	95.3
peacock008	*Pavo cristatus*	bronze		9.8	82 514 008	98.9	95.3
peacock009	*Pavo cristatus*	bronze		9.4	79 772 763	98.9	96.1
peacock010	*Pavo cristatus*	bronze		8.7	74 944 196	98.4	96.3
peacock011	*Pavo cristatus*	bronze		8.9	74 850 903	99.1	95.2
peacock012	*Pavo cristatus*	bronze		9.1	77 517 989	99.1	96.7
peacock013	*Pavo cristatus*	cameo	black-shoulder	7.8	68 595 974	98.8	96.6
peacock014	*Pavo cristatus*	bronze		9.3	80 469 878	98.8	95.4
peacock015	*Pavo cristatus*	cameo	black-shoulder	10.2	85 935 164	98.7	95.9
peacock016	*Pavo cristatus*	cameo	black-shoulder	8.8	75 138 376	98.0	95.0
peacock017	*Pavo cristatus*	cameo		8.1	71 067 052	98.5	94.2
peacock018	*Pavo cristatus*	cameo		10.1	87 030 285	98.8	95.4
peacock019	*Pavo cristatus*	cameo		9.1	79 153 902	98.3	96.0
peacock020	*Pavo cristatus*	cameo	black-shoulder	11.3	94 994 710	98.9	94.9
peacock021	*Pavo cristatus*	cameo		8.1	72 299 953	98.8	96.2
peacock022	*Pavo cristatus*	cameo		8.9	73 970 015	98.7	95.9
peacock023	*Pavo cristatus*	cameo		14.1	119 938 068	99.1	95.8
peacock024	*Pavo cristatus*	cameo		9.2	79 105 044	98.8	96.8
peacock025	*Pavo cristatus*	cameo		11.8	104 125 601	99.1	96.1
peacock026	*Pavo cristatus*	cameo		8.3	71 172 758	98.9	96.8
peacock027	*Pavo cristatus*	cameo		10.5	93 198 763	98.8	96.2
peacock028	*Pavo cristatus*	opal		8.5	73 985 449	98.7	95.8
peacock029	*Pavo cristatus*	opal		9.0	78 284 880	98.9	95.7
peacock030	*Pavo cristatus*	opal		8.4	71 571 758	98.8	96.0
peacock031	*Pavo cristatus*	opal		8.8	73 891 382	98.4	95.8
peacock032	*Pavo cristatus*	opal		8.5	72 839 698	98.7	95.4
peacock033	*Pavo cristatus*	opal		6.8	59 094 643	99.1	95.7
peacock034	*Pavo cristatus*	opal		8.9	75 667 198	98.7	96.6
peacock035	*Pavo cristatus*	opal		7.8	71 572 780	98.7	95.8
peacock036	*Pavo cristatus*	opal		10.9	90 847 869	98.8	95.7
peacock037	*Pavo cristatus*	opal		10.0	85 219 019	99.0	96.1
peacock038	*Pavo cristatus*	opal		9.9	83 601 888	98.6	96.6
peacock039	*Pavo cristatus*	opal		8.0	69 961 722	98.2	95.1
peacock040	*Pavo cristatus*	opal		7.6	64 247 995	98.8	94.8
peacock041	*Pavo cristatus*	prussian-blue	black-shoulder	16.9	148 632 494	99.0	96.3
peacock042	*Pavo cristatus*	prussian-blue	black-shoulder	11.7	99 871 842	98.6	96.5
peacock043	*Pavo cristatus*	prussian-blue	black-shoulder	7.9	68 903 920	98.8	95.5
peacock044	*Pavo cristatus*	prussian-blue	black-shoulder	9.5	80 601 736	98.8	96.0
peacock045	*Pavo cristatus*	prussian-blue	black-shoulder	9.7	82 980 871	98.6	96.2
peacock046	*Pavo cristatus*	prussian-blue	black-shoulder	8.8	74 950 790	98.5	95.5
peacock047	*Pavo cristatus*	prussian-blue	*black-shoulder*	8.9	78 423 035	98.7	95.3
peacock048	*Pavo cristatus*	prussian-blue	*black-shoulder*	9.2	77 177 496	98.6	95.7
peacock049	*Pavo cristatus*	prussian-blue		14.2	128 846 524	97.8	95.8
peacock050	*Pavo cristatus*	prussian-blue		9.8	88 365 882	97.5	92.1
peacock051	*spalding*	purple		7.6	67 195 165	98.6	91.1
peacock052	*Pavo cristatus*	purple		6.6	58 007 239	98.8	95.8

peacock053	*Pavo cristatus*	purple	9.6	82 977 526	98.7	95.8
peacock054	*Pavo cristatus*	purple	5.2	46 716 968	98.6	95.8
peacock055	*Pavo cristatus*	purple	9.0	79 847 660	98.6	95.2
peacock056	*Pavo cristatus*	purple	4.9	42 516 372	98.3	95.2
peacock057	*Pavo cristatus*	purple	9.1	79 525 289	98.6	93.4
peacock058	*Pavo cristatus*	purple	7.5	64 188 415	98.7	94.9
peacock059	*Pavo cristatus*	purple	7.5	65 858 079	98.7	95.1
peacock060	*Pavo cristatus*	purple	7.4	65 375 482	98.6	95.2
peacock061	*Pavo cristatus*	purple	7.3	62 853 140	98.9	94.9
peacock062	*Pavo cristatus*	raw-umber	7.0	60 844 559	99.1	96.2
peacock063	*Pavo cristatus*	raw-umber	8.6	75 843 161	98.5	96.7
peacock064	*Pavo cristatus*	raw-umber	6.6	57 904 928	98.8	94.6
peacock065	*Pavo cristatus*	raw-umber	9.8	85 733 473	98.2	95.7
peacock066	*Pavo cristatus*	raw-umber	6.6	58 247 364	97.4	92.6
peacock067	*Pavo cristatus*	raw-umber	9.0	79 522 167	98.9	92.6
peacock068	*Pavo cristatus*	raw-umber	9.6	82 887 591	98.8	95.7
peacock069	*Pavo cristatus*	violet	9.7	86 060 745	98.5	96.2
peacock070	*Pavo cristatus*	violet	8.2	68 984 267	99.1	95.1
peacock071	*Pavo cristatus*	violet	6.7	59 488 393	98.9	97.0
peacock072	*Pavo cristatus*	violet	9.0	78 784 225	98.9	96.2
peacock073	*Pavo cristatus*	violet	8.4	73 061 934	98.7	95.9
peacock074	*Pavo cristatus*	violet	8.8	76 792 327	98.7	95.6
peacock075	*Pavo cristatus*	violet	7.3	64 151 498	98.8	95.5
peacock076	*Pavo cristatus*	violet	8.7	74 466 728	98.8	96.0
peacock077	*Pavo cristatus*	violet	8.1	71 459 385	98.6	95.8
peacock078	*Pavo cristatus*	violet	8.4	73 004 433	98.7	95.3
peacock079	*Pavo cristatus*	violet	10.9	96 074 477	98.7	95.3
peacock080	*Pavo cristatus*	violet	8.9	76 879 453	98.9	95.0
peacock081	*Pavo cristatus*	violet	9.3	80 503 388	98.5	96.2
peacock082	*Pavo cristatus*	white	7.2	61 219 168	98.9	95.0
peacock083	*Pavo cristatus*	white	8.3	70 906 180	98.5	96.2
peacock084	*Pavo cristatus*	white	8.9	78 109 981	98.3	95.3
peacock085	*Pavo cristatus*	white	8.5	76 331 840	98.8	94.5
peacock086	*Pavo cristatus*	white	7.9	67 077 443	98.8	95.8
peacock087	*Pavo cristatus*	white	8.1	69 013 029	98.0	95.8
peacock088	*Pavo cristatus*	white	7.0	61 258 164	98.5	93.5
peacock089	*Pavo cristatus*	white	6.0	52 758 580	98.7	95.1
peacock090	*Pavo cristatus*	white	7.3	64 010 239	98.9	95.8
peacock091	*Pavo cristatus*	white	8.0	69 844 607	98.6	96.4
peacock092	*Pavo cristatus*	wild-type	8.3	71 579 202	98.1	95.3
peacock093	*Pavo cristatus*	wild-type	8.8	75 518 209	98.9	93.9
peacock094	*Pavo cristatus*	wild-type	10.1	86 577 842	98.7	96.2
peacock095	*Pavo cristatus*	wild-type	9.1	77 748 705	98.4	95.1
peacock096	*Pavo cristatus*	wild-type	10.0	86 014 708	98.5	95.2
peacock097	*Pavo cristatus*	wild-type	10.2	91 156 190	99.1	94.8
peacock098	*Pavo cristatus*	wild-type	8.1	67 569 237	98.1	96.7
peacock099	*Pavo cristatus*	wild-type	6.9	58 771 766	98.9	94.5
peacock100	*Pavo cristatus*	wild-type	8.8	74 265 385	98.7	96.5
peacock101	*Pavo cristatus*	peach	9.4	79 710 570	98.5	95.9
peacock102	*Pavo cristatus*	peach	3.9	35 333 950	97.3	93.1
peacock103	*Pavo cristatus*	peach	7.5	63 475 572	98.2	85.8
peacock104	*Pavo cristatus*	brown	7.5	65 632 909	98.5	92.6
peacock105	*Pavo cristatus*	brown	6.0	51 289 165	97.9	93.0
peacock106	*Pavo cristatus*	brown	6.1	54 026 900	97.8	91.8
peacock107	*Pavo cristatus*	charcoal	5.8	51 348 493	98.1	89.7
peacock108	*Pavo cristatus*	charcoal	7.5	63 885 183	98.6	91.6

peacock109	*Pavo cristatus*	charcoal		9.7	83 648 618	98.1	93.5
peacock110	*Pavo cristatus*	charcoal		11.0	97 767 387	98.0	90.8
peacock111	*Pavo cristatus*	charcoal		8.3	73 001 564	98.0	91.6
peacock112	*Pavo cristatus*	midnight	black-shoulder	7.1	61 585 754	98.4	91.4
peacock113	*Pavo cristatus*	midnight	black-shoulder	5.4	47 093 664	98.1	92.5
peacock114	*Pavo cristatus*	midnight	black-shoulder	5.5	48 336 350	97.6	91.7
peacock115	*Pavo cristatus*	wild-type	black-shoulder	7.5	65 927 927	98.1	90.8
peacock116	*Pavo cristatus*	wild-type	black-shoulder	10.6	91 047 910	98.5	91.1
peacock117	*Pavo cristatus*	wild-type	black-shoulder	10.4	90 393 443	98.3	94.1
peacock118	*Pavo cristatus*	charcoal		2.6	48 042 179	98.9	92.3
peacock119	*Pavo cristatus*	hazel		1.9	44 767 165	99.2	96.8
peacock120	*Pavo cristatus*	indigo		3.4	49 989 461	99.3	97.6
peacock121	*Pavo cristatus*	ivory		3.2	60 497 633	99.1	97.9
peacock122	*Pavo cristatus*	jade		4.7	67 917 003	99.0	97.4
peacock123	*Pavo cristatus*	midnight		5.4	76 642 936	99.0	97.3
peacock124	*Pavo cristatus*	peach		2.0	28 200 742	99.0	97.1
peacock125	*Pavo cristatus*	opal		3.8	59 089 537	99.1	97.1
peacock126	*Pavo cristatus*	purple		3.1	53 963 210	99.1	97.5
peacock127	*Pavo cristatus*	cameo		3.4	53 314 729	99.2	97.6
peacock128	*Pavo cristatus*	sonja violet		3.4	54 987 361	99.0	97.6
peacock129	*Pavo cristatus*	white		2.8	47 046 279	99.2	97.4
peacock130	*Pavo cristatus*	white		3.5	48 956 062	99.3	97.9
peacock132	*Pavo cristatus*	white		4.8	86 794 650	99.2	98.0
peacock133	*Pavo cristatus*	white		2.9	49 086 529	98.9	97.8
peacock134	*Pavo cristatus*	white		4.9	68 266 639	99.2	96.9
peacock135	*Pavo cristatus*	white		5.5	101 212 335	98.8	97.7
peacock136	*Pavo cristatus*	white		5.6	188 093 363	99.0	96.7
peacock137	*Pavo cristatus*	opal		3.6	52 270 392	98.9	97.1
peacock138	*Spalding*	NA		2.6	46 333 090	99.0	96.9
peacock139	*Spalding*	NA		4.7	70 574 921	99.0	97.0
peacock140	*Spalding*	NA		6.9	108 033 826	99.0	96.9
peacock141	*Spalding*	NA		6.8	132 732 376	98.7	96.8
peacock142	*Spalding*	NA		6.0	103 739 490	98.7	96.0
peacock143	*Pavo cristatus*	charcoal	black-shoulder	4.9	72 640 330	98.7	96.3
peacock144	*Spalding*	NA		5.0	67 949 451	99.1	96.5
peacock145	*Spalding*	NA		4.2	64 692 475	98.5	97.2
peacock146	*Spalding*	NA		1.4	13 994 504	99.3	95.9
peacock147	*Spalding*	NA		6.0	81 793 150	98.8	96.6
peacock148	*Pavo cristatus*	raw-umber		10.6	93 980 060	97.7	96.4
peacock149	*Pavo cristatus*	raw-umber		5.5	49 192 542	97.7	92.7
peacock150	*Pavo cristatus*	raw-umber		8.2	71 812 702	98.2	91.5
peacock151	*Pavo cristatus*	raw-umber		6.5	59 468 420	97.1	92.9
peacock152	*Pavo cristatus*	wild-type		9.1	83 614 418	97.5	85.6
peacock153	*Pavo cristatus*	raw-umber	black-shoulder	17.9	161 977 719	97.9	90.4
peacock154	*Pavo cristatus*	raw-umber	black-shoulder	7.7	67 938 857	98.4	92.9
peacock155	*Pavo cristatus*	prussian-blue		11.0	98 086 128	97.6	93.0
peacock156	*Pavo cristatus*	prussian-blue	black-shoulder	8.6	76 077 469	98.1	89.9
peacock157	*Pavo cristatus*	prussian-blue	black-shoulder	6.9	63 654 245	97.3	91.8
peacock158	*Pavo cristatus*	prussian-blue	black-shoulder	7.8	70 272 783	97.3	89.6
peacock159	*Pavo cristatus*	prussian-blue	black-shoulder	9.0	78 320 185	97.9	90.0
peacock160	*Pavo cristatus*	bronze		9.5	85 001 373	98.0	90.3
peacock161	*Pavo cristatus*	raw-umber/prussian-blue		10.2	92 448 410	98.0	92.6
peacock162	*Pavo cristatus*	raw-umber/prussian-blue		9.7	86 132 454	97.4	93.0
peacock163	*Pavo cristatus*	prussian-blue		12.8	115 611 222	98.2	91.3
peacock164	*Pavo cristatus*	wild-type		19.4	203 719 913	98.1	91.4
peacock165	*Pavo cristatus*	wild-type		7.6	68 939 995	97.8	93.6

peacock166	*Pavo cristatus*	wild-type		17.9	220 217 938	98.1	91.6
peacock167	*Pavo cristatus*	purple		22.1	258 065 356	98.2	93.9
peacock168	*Pavo cristatus*	wild-type		11.7	105 287 197	97.8	94.1
peacock169	*Pavo cristatus*	purple	black-shoulder	7.7	138 550 110	98.9	92.3
peacock170	*Pavo cristatus*	purple		5.9	52 993 405	97.6	96.9
peacock171	*Pavo cristatus*	purple		18.8	216 601 888	98.3	91.4
peacock172	*Pavo cristatus*	purple		21.0	255 493 972	98.2	94.7
peacock173	*Pavo cristatus*	purple		14.6	136 616 219	96.7	94.2
peacock174	*Pavo cristatus*	bronze	black-shoulder	3.4	29 753 754	98.2	85.4
peacock175	*Pavo cristatus*	bronze	black-shoulder	10.3	89 029 840	97.9	84.0
peacock178	*Pavo cristatus*	hazel	black-shoulder	3.3	29 990 348	98.3	86.6
peacock179	*Pavo cristatus*	hazel	black-shoulder	7.3	62 493 554	98.2	86.1
peacock180	*Pavo cristatus*	taupe		4.8	41 541 203	98.4	86.8
peacock181	*Pavo cristatus*	taupe		3.9	34 575 680	98.2	88.8
peacock182	*Pavo cristatus*	taupe		4.9	42 864 124	98.4	84.2
peacock183	*Pavo cristatus*	taupe		6.8	57 857 064	98.7	87.6
peacock184	*Pavo cristatus*	bronze		4.3	37 787 983	98.4	89.4
peacock185	*Spalding*	NA		11.6	100 809 507	97.9	88.1
peacock186	*Spalding*	NA		7.2	63 201 159	98.5	84.4
peacock188	*Pavo cristatus*	cameo		6.3	53 966 104	98.1	87.9
peacock189	*Pavo cristatus*	cameo		6.8	59 474 996	98.1	87.0
peacock190	*Pavo cristatus*	cameo		2.9	24 800 490	98.2	85.9
peacock191	*Pavo cristatus*	cameo		6.1	53 233 914	98.6	86.8
peacock194	*Pavo cristatus*	hazel		1.1	9 818 940	98.4	88.6
peacock195	*Pavo cristatus*	taupe		2.0	17 654 757	98.2	86.6
peacock196	*Pavo cristatus*	bronze	black-shoulder	1.2	10 988 511	98.3	83.6
peacock197	*Pavo cristatus*	purple		4.4	40 442 485	98.0	84.2
peacock198	*Pavo cristatus*	purple		7.5	63 134 995	98.4	79.3
peacock199	*Pavo cristatus*	purple		13.9	110 871 827	98.2	88.6
peacock200	*Pavo cristatus*	hazel		4.8	41 297 599	98.5	89.1
peacock202	*Pavo cristatus*	hazel	black-shoulder	1.3	10 904 568	98.1	88.1
peacock203	*Pavo cristatus*	taupe	black-shoulder	8.4	73 009 016	98.1	83.0
peacock213	*Pavo cristatus*	taupe	black-shoulder	3.8	34 224 797	97.2	86.9
peacock214	*Pavo cristatus*	taupe		4.6	39 514 249	98.6	78.9
peacock215	*Pavo cristatus*	taupe		6.0	51 469 764	98.5	90.0
peacock216	*Pavo cristatus*	purple		8.1	70 110 130	98.3	88.3
peacock217	*Pavo cristatus*	purple		8.9	77 435 938	98.1	88.3
peacock218	*Pavo cristatus*	purple		13.4	113 232 769	98.1	85.9
peacock219	*Pavo cristatus*	purple		11.6	101 647 507	98.3	87.9
peacock220	*Pavo cristatus*	bronze	black-shoulder	5.6	48 430 459	98.0	86.0
peacock221	*Pavo cristatus*	bronze	black-shoulder	7.0	61 247 542	98.2	84.1
peacock234	*Pavo cristatus*	charcoal	black-shoulder	2.2	18 964 784	97.5	86.1
peacock235	*Pavo cristatus*	charcoal	black-shoulder	14.1	104 729 475	98.4	83.8
peacock236	*Pavo cristatus*	purple		12.9	106 671 473	97.8	93.6
peacock237	*Pavo cristatus*	wild-type	black-shoulder	1.8	16 252 693	97.7	84.7
peacock238	*Pavo cristatus*	opal	black-shoulder	1.3	11 967 643	97.5	82.3
peacock239	*Pavo cristatus*	opal	black-shoulder	0.9	8 454 179	98.2	76.9
peacock240	*Pavo cristatus*	opal		3.0	27 155 082	97.1	83.3
peacock241	*Pavo cristatus*	opal	black-shoulder	14.2	104 252 581	98.8	76.7
peacock242	*Pavo cristatus*	opal	black-shoulder	14.2	105 820 728	98.4	95.6
peacock243	*Pavo cristatus*	opal		13.4	112 016 486	98.1	94.3
peacock244	*Pavo cristatus*	opal		12.3	108 830 935	98.2	88.4
peacock245	*Pavo cristatus*	cameo		7.8	67 308 883	98.2	87.6
peacock246	*Pavo cristatus*	bronze	black-shoulder	8.6	76 081 418	98.1	88.3
peacock247	*Pavo cristatus*	wild-type		4.8	42 582 597	98.0	84.3
peacock248	*Pavo cristatus*	wild-type		2.4	21 660 929	98.0	82.8

peacock249	*Pavo cristatus*	opal		14.1	111 261 792	98.2	81.2
peacock251	*Pavo cristatus*	opal		11.2	97 602 424	97.7	89.2
peacock252	*Pavo cristatus*	purple		12.3	102 523 574	98.2	85.9
peacock253	*Pavo cristatus*	purple		12.6	109 400 811	98.2	89.5
peacock255	*Pavo cristatus*	midnight	black-shoulder	13.5	110 539 650	98.2	87.7
peacock265	*Pavo cristatus*	charcoal	black-shoulder	11.9	91 296 018	98.9	89.4
peacock266	*Pavo cristatus*	charcoal	black-shoulder	6.1	45 863 079	99.1	96.1
peacock267	*Pavo cristatus*	charcoal		7.1	53 609 721	98.9	96.4
peacock268	*Pavo cristatus*	charcoal		7.7	59 159 845	99.0	96.0
peacock269	*Pavo cristatus*	charcoal		7.3	55 401 774	98.6	95.9
peacock270	*Pavo cristatus*	charcoal		3.2	24 650 448	98.4	94.7
peacock271	*Pavo cristatus*	charcoal		6.3	48 379 662	98.5	94.2
peacock272	*Pavo cristatus*	violet		3.4	25 635 955	98.7	94.1
peacock273	*Pavo cristatus*	violet		7.9	59 660 304	99.1	95.1
peacock274	*Pavo cristatus*	violet		3.9	29 666 064	98.5	96.2
peacock275	*Pavo cristatus*	violet		9.8	73 873 385	98.7	94.7
peacock276	*Pavo cristatus*	violet		10.2	77 304 191	98.9	95.5
peacock277	*Pavo cristatus*	violet		10.9	83 026 124	98.7	95.7
peacock278	*Pavo cristatus*	violet		12.5	94 625 445	99.0	95.3
peacock279	*Pavo cristatus*	violet		6.1	46 833 204	98.0	96.4
peacock280	*Pavo cristatus*	violet		8.6	65 470 491	98.2	93.1
peacock281	*Pavo cristatus*	violet		3.9	29 509 013	99.0	94.3
peacock282	*Pavo cristatus*	bronze	black-shoulder	14.4	109 037 981	99.0	96.2
peacock283	*Pavo cristatus*	bronze	black-shoulder	12.1	92 583 156	98.7	96.1
peacock284	*Pavo cristatus*	bronze	black-shoulder	10.0	75 618 516	99.1	95.4
peacock285	*Pavo cristatus*	bronze		15.7	123 907 871	98.6	96.4
peacock286	*Pavo cristatus*	bronze	black-shoulder	7.3	54 664 769	98.9	94.2
peacock287	*Pavo cristatus*	bronze		9.6	73 826 811	98.8	95.6
peacock288	*Pavo cristatus*	bronze		9.8	74 668 646	99.1	93.9
peacock289	*Pavo cristatus*	bronze	black-shoulder	11.6	86 674 171	99.1	96.6
peacock290	*Pavo cristatus*	bronze	black-shoulder	20.8	160 060 747	98.7	96.6
peacock291	*Pavo cristatus*	bronze	black-shoulder	12.6	95 918 318	98.7	95.5
peacock292	*Pavo cristatus*	cameo		22.1	168 853 561	98.7	94.8
peacock293	*Pavo cristatus*	cameo	black-shoulder	10.6	80 177 762	98.7	94.5
peacock294	*Pavo cristatus*	cameo		16.0	121 773 622	98.6	94.9
peacock295	*Pavo cristatus*	cameo		23.3	175 887 380	99.0	95.7
peacock296	*Pavo cristatus*	cameo	black-shoulder	22.8	172 769 031	98.9	96.3
peacock297	*Pavo cristatus*	cameo		25.5	192 948 430	98.9	96.3
peacock298	*Pavo cristatus*	cameo		26.7	209 519 127	98.7	96.1
peacock299	*Pavo cristatus*	cameo		12.0	91 033 581	98.8	95.6
peacock300	*Pavo cristatus*	cameo	black-shoulder	8.0	60 973 876	98.5	95.4
peacock301	*Pavo cristatus*	cameo	black-shoulder	18.3	139 940 589	98.4	93.5
peacock302	*Pavo cristatus*	opal	black-shoulder	19.9	152 210 258	98.7	94.2
peacock303	*Pavo cristatus*	opal	black-shoulder	23.4	177 286 695	98.8	95.4
peacock304	*Pavo cristatus*	opal		26.9	203 808 073	99.1	95.7
peacock305	*Pavo cristatus*	opal		7.7	57 904 819	98.8	96.9
peacock306	*Pavo cristatus*	opal		21.7	164 997 536	99.0	96.0
peacock307	*Pavo cristatus*	opal	black-shoulder	14.0	106 104 077	98.7	96.4
peacock308	*Pavo cristatus*	opal		21.1	160 762 662	98.7	95.7
peacock309	*Pavo cristatus*	opal	black-shoulder	12.7	97 318 344	98.4	95.9
peacock310	*Pavo cristatus*	opal		11.7	89 630 025	98.7	94.4
peacock311	*Pavo cristatus*	opal		18.9	142 182 607	98.9	94.7
peacock312	*Pavo cristatus*	purple	black-shoulder	5.5	40 748 769	99.1	96.2
peacock313	*Pavo cristatus*	purple		7.9	58 348 392	99.1	96.8
peacock314	*Pavo cristatus*	purple		14.0	105 088 511	99.2	96.9
peacock315	*Pavo cristatus*	purple		8.7	64 418 410	99.0	96.6

peacock316	*Pavo cristatus*	purple		5.2	38 640 189	99.0	96.3
peacock317	*Pavo cristatus*	purple	black-shoulder	12.9	95 704 636	99.1	96.2
peacock318	*Pavo cristatus*	purple		5.9	43 641 533	98.8	96.9
peacock319	*Pavo cristatus*	purple	black-shoulder	13.4	99 874 696	98.9	96.0
peacock320	*Pavo cristatus*	purple		21.8	163 038 760	99.2	96.3
peacock321	*Pavo cristatus*	purple	black-shoulder	9.6	71 264 913	98.8	96.8
peacock322	*Pavo cristatus*	hazel	black-shoulder	9.8	73 048 388	99.1	96.3
peacock323	*Pavo cristatus*	hazel	black-shoulder	11.8	87 771 167	99.2	96.6
peacock324	*Pavo cristatus*	hazel	black-shoulder	9.2	68 605 609	99.1	97.2
peacock332	*Pavo cristatus*	wild-type	black-shoulder	14.1	105 321 345	99.0	96.6
peacock333	*Pavo cristatus*	wild-type		9.3	69 341 044	99.1	96.5
peacock334	*Pavo cristatus*	wild-type	black-shoulder	9.5	71 184 976	99.0	96.9
peacock335	*Pavo cristatus*	wild-type		12.1	89 757 663	99.2	96.2
peacock336	*Pavo cristatus*	wild-type		9.1	67 797 867	99.0	97.0
peacock337	*Pavo cristatus*	wild-type	black-shoulder	10.1	75 346 911	99.1	96.7
peacock338	*Pavo cristatus*	wild-type	black-shoulder	5.9	43 460 812	99.0	96.7
peacock339	*Pavo cristatus*	hazel		6.7	49 856 723	99.1	96.4
peacock340	*Pavo cristatus*	chestnut		10.6	78 974 502	99.0	96.7
peacock341	*Pavo cristatus*	charcoal		16.9	126 937 880	98.9	96.3
peacock342	*Pavo muticus*	wild-type		9.2	68 532 071	98.8	96.4
peacock343	*Pavo muticus*	wild-type		22.2	166 010 149	98.9	95.6
peacock350	*Pavo cristatus*	wild-type	black-shoulder	24.2	180 618 850	99.2	95.9
peacock352	*Pavo cristatus*	wild-type		10.6	78 836 727	98.9	97.1
peacock358	*Pavo muticus*	wild-type		29.0	221 634 574	98.9	96.3
peacock359	*Pavo muticus*	wild-type		17.0	127 349 189	98.7	95.9
peacock364	*Pavo cristatus*	violet		21.6	162 541 012	98.8	95.4
peacock365	*Pavo cristatus*	violet		12.6	94 525 743	98.8	95.7
peacock366	*Pavo cristatus*	violet		22.2	168 026 281	98.8	94.8
peacock367	*Pavo cristatus*	violet		21.6	161 679 458	99.2	94.7
peacock368	*Pavo cristatus*	purple		10.8	80 852 232	99.0	96.9
peacock369	*Pavo cristatus*	purple	black-shoulder	16.1	119 825 424	99.2	96.6
peacock370	*Pavo cristatus*	purple		17.4	131 065 426	99.2	96.8
peacock371	*Pavo cristatus*	purple		8.6	64 012 797	99.0	96.7
peacock376	*Pavo cristatus*	opal		8.9	66 994 698	98.8	96.4
peacock377	*Pavo cristatus*	opal	black-shoulder	7.5	56 583 466	98.8	94.5
peacock378	*Pavo cristatus*	opal		17.0	127 536 413	98.8	95.2
peacock379	*Pavo cristatus*	wild-type		22.8	170 104 871	99.1	93.8
peacock380	*Pavo cristatus*	wild-type		8.3	62 501 411	98.8	96.8
peacock381	*Pavo cristatus*	charcoal		6.0	44 327 572	99.2	95.9
peacock383	*Pavo cristatus*	cameo	black-shoulder	10.3	77 230 425	98.9	96.5
peacock384	*Pavo cristatus*	cameo		5.3	40 070 238	98.4	96.0
peacock385	*Pavo cristatus*	cameo		11.9	88 952 118	98.8	93.2
peacock386	*Pavo cristatus*	bronze		9.9	74 748 054	98.9	94.3
peacock387	*Pavo cristatus*	bronze		12.5	93 672 049	98.9	95.2
peacock388	*Pavo cristatus*	bronze	black-shoulder	13.6	105 025 164	98.6	95.4
peacock389	*Pavo cristatus*	midnight	black-shoulder	10.3	77 968 699	98.9	95.2
peacock390	*Pavo cristatus*	midnight	black-shoulder	7.4	56 142 606	98.6	96.3
peacock391	*Pavo cristatus*	midnight		12.5	95 478 844	98.9	95.4
peacock395	*Pavo cristatus*	wild-type	black-shoulder	12.7	97 124 037	98.5	96.0
peacock398	*Pavo cristatus*	opal	black-shoulder	8.6	64 820 694	98.9	95.3
peacock399	*Pavo cristatus*	opal		8.8	67 110 737	98.8	96.1
peacock400	*Pavo cristatus*	opal		14.8	111 879 169	98.7	95.9
peacock401	*Pavo cristatus*	taupe		11.7	88 998 685	98.7	95.6
peacock402	*Pavo cristatus*	taupe		14.5	109 898 461	98.9	95.8
peacock403	*Pavo cristatus*	charcoal		5.7	42 462 794	98.9	96.1
peacock408	*Pavo cristatus*	midnight	black-shoulder	9.4	70 858 951	98.9	96.0

peacock409	*Pavo cristatus*	midnight	black-shoulder	13.4	102 506 553	98.7	95.8
peacock410	*Pavo cristatus*	wild-type	black-shoulder	18.6	141 930 675	98.8	95.7
peacock411	*Pavo cristatus*	wild-type		23.0	176 741 713	98.4	95.6
peacock412	*Pavo cristatus*	wild-type		13.1	99 678 354	98.9	93.9
peacock413	*Pavo cristatus*	wild-type		9.2	70 188 099	98.6	95.9
peacock414	*Pavo cristatus*	wild-type		17.8	134 808 622	98.7	95.0
peacock415	*Pavo cristatus*	wild-type		10.5	79 961 235	98.8	95.4
peacock416	*Pavo cristatus*	wild-type		10.0	78 318 965	98.7	95.8
peacock417	*Pavo cristatus*	wild-type		6.9	52 279 229	98.6	95.2
peacock418	*Pavo cristatus*	wild-type		9.2	71 429 623	98.4	94.9
peacock421	*Pavo cristatus*	wild-type		20.6	168 551 380	98.4	94.8
peacock422	*Pavo cristatus*	wild-type		18.6	153 383 463	98.7	96.0
peacock423	*Pavo cristatus*	wild-type		18.5	150 156 609	98.6	96.3
peacock424	*Pavo cristatus*	wild-type		22.9	189 274 044	98.5	96.4
peacock425	*Pavo cristatus*	wild-type		21.8	177 563 064	98.7	96.5
peacock426	*Pavo cristatus*	wild-type		14.5	118 026 139	98.7	96.8
peacock428	*Pavo cristatus*	charcoal		9.0	117 628 788	99.6	96.7
peacock429	*Pavo cristatus*	ultramarine		9.9	149 783 723	99.7	98.5
peacock430	*Pavo cristatus*	ultramarine		13.0	179 668 317	99.7	98.8
peacock431	*Pavo cristatus*	ultramarine		5.9	68 325 260	99.6	98.9
peacock432	*Pavo cristatus*	ultramarine		15.9	274 466 223	99.3	98.7
peacock433	*Pavo cristatus*	ultramarine		14.8	210 587 599	99.7	98.2
peacock434	*Pavo cristatus*	ultramarine		12.5	175 168 642	98.0	97.5
peacock435	*Pavo cristatus*	ultramarine		18.1	301 514 174	99.3	97.3
peacock436	*Pavo cristatus*	ultramarine		17.7	222 126 642	99.7	98.0
peacock437	*Pavo cristatus*	ultramarine		18.2	248 213 883	99.8	97.3
peacock438	*Pavo cristatus*	ultramarine		4.3	61 006 029	99.6	96.5
peacock439	*Pavo cristatus*	ultramarine		5.6	69 465 446	98.3	98.5
peacock448	*Pavo cristatus*	raw-umber	black-shoulder	12.0	99 918 843	98.5	96.1
peacock449	*Pavo cristatus*	raw-umber	black-shoulder	14.2	117 310 064	98.5	96.2
peacock452	*Pavo cristatus*	raw-umber/ prussian-blue	black-shoulder	18.8	153 387 245	98.7	96.1
peacock453	*Pavo cristatus*	prussian-blue	black-shoulder	25.6	211 854 433	98.4	96.7
peacock454	*Pavo cristatus*	prussian-blue	black-shoulder	19.2	157 758 481	98.7	96.4
peacock455	*Pavo cristatus*	prussian-blue	black-shoulder	20.3	168 577 890	98.3	97.0
peacock456	*Pavo cristatus*	prussian-blue	black-shoulder	18.9	153 790 587	98.9	95.8
peacock457	*Pavo cristatus*	prussian-blue	black-shoulder	23.0	190 959 524	98.7	97.0

Table S8. RNA-sequencing statistics for regenerating feather follicles from peafowl neck and wing.

ID	Body phenotype	Wing phenotype	Feather follicle		Number of reads
			Neck	Wing	
peacock460	Opal		X		84 663 672
peacock469	Cameo		X		97 612 226
peacock470	Cameo		X		97 612 226
peacock471	Bronze		X		84 853 934
peacock473	Wild-type		X		67 658 498
peacock474	Bronze		X		54 789 354
peacock475	Bronze		X		82 021 652
peacock476	Violet		X		82 765 102
peacock477	Violet		X		83 352 310
peacock479	Wild-type		X		82 127 766
peacock480	White		X		47 051 030
peacock487	Purple		X		68 502 820
peacock488	Purple		X		83 074 342
peacock489	Wild-type		X		85 734 468
peacock490	Wild-type		X		71 770 966
peacock491	Opal		X		77 832 716
peacock492	Cameo		X		62 452 472
peacock493	Purple		X		56 326 838
peacock494	Wild-type		X		63 742 562
peacock496	White		X		88 610 120
peacock497	Wild-type		X		65 887 202
peacock506	Ultramarine		X		145 574 546
peacock507	*Ultramarine*		X		194 918 934
peacock508	*Charcoal*		X		202 059 768
peacock510	*Ultramarine*		X		206 821 926
peacock521	*Charcoal*		X		210 442 370
peacock522	*Charcoal*		X		211 975 220
peacock473		Wild-type		X	66 416 662
peacock476		Wild-type		X	51 536 456
peacock489		Black-shoulder		X	63 387 960
peacock497		Wild-type		X	62 204 698
peacock500		Wild-type		X	41 911 332
peacock501		Black-shoulder		X	56 572 500
peacock502		Black-shoulder		X	53 733 978
peacock503		Black-shoulder		X	44 944 076
peacock504		Wild-type		X	73 628 562
peacock505		Wild-type		X	66 995 070

Table S9. Quantitative analysis of melanin content in feathers of the common emerald dove and mallard

			S-350 (/mg)[b]		AHPO (ng/mg)[c]			HI (ng/mg)[d]		TM[e]	EM[f]	BZ[g]	BT[h]	PM[i]
Species	**Sample ID**	**Area[a]**	**A500**	**A650**	**PTCA**	**PDCA**	**TTCA**	**4-AHP**	**3-AHP**	**(μg/mg)**	**(μg/mg)**	**(μg/mg)**	**(μg/mg)**	**(μg/mg)**
Mallard	1	i	1.324	0.452	1337	127	578	51	36	134	107	19.7	0.5	20.1
Mallard	1	ii	0.297	0.099	398	38	120	7	11	30	32	4.1	0.1	4.1
Mallard	2	i	1.246	0.429	1274	122	577	59	8	126	102	19.6	0.5	20.1
Mallard	2	ii	0.271	0.091	341	28	123	6	10	27	27	4.2	0.1	4.2
Mallard	3	i	1.360	0.462	1162	80	551	81	37	137	93	18.7	0.7	19.5
Mallard	3	ii	0.336	0.116	456	39	116	8	7	34	36	3.9	0.1	4.0
Mallard	4	i	1.430	0.488	1182	80	565	71	44	144	95	19.2	0.6	19.8
Mallard	4	ii	0.424	0.136	513	44	179	8	9	43	41	6.1	0.1	6.2
Emerald dove	1	i	2.377	0.839	2409	204	660	47	33	240	193	22.4	0.4	22.9
Emerald dove	1	ii	1.276	0.433	1633	143	184	13	31	129	131	6.3	0.1	6.4
Emerald dove	2	i	2.405	0.841	2429	224	639	40	51	243	194	21.7	0.4	22.1
Emerald dove	2	ii	1.405	0.464	1691	151	188	17	47	142	135	6.4	0.1	6.5

[a]The number of the area refers to **fig. S11**.
[b]Soluene-350 solubilization
[c]Alkaline hydrogen peroxide oxidation
[d]Hydroiodic acid hydrolysis
[e]Total melanin (A500 × 101)
[f]Eumelanin (PTCA × 0.080)
[g]Benzothiazole (TTCA × 0.034)
[h]Benzothiazine (4-AHP × 0.009)
[i]Pheomelanin (BZ + BT)

Table S10. Single-cell RNA-sequencing and read mapping statistics.

Species	Individual	Experiment	Phenotype	Number of read pairs	Valid barcodes (%)[a]	Mapped reads (%)[b]	Reads mapped confidently to genome (%)[c]	Reads mapped confidently to transcriptome (%)[d]	Reads mapped confidently to intronic regions (%)[e]	Reads mapped confidently to exonic regions (%)[f]	Reads mapped antisense to gene (%)[g]	Valid UMI (%)[h]
Emerald dove	1	1	Iridescent	77,432,152	96.6	89.9	81.3	68.3	12.4	60.0	4.0	99.9
Emerald dove	1	1	Non-iridescent	119,961,948	94.4	72.1	63.5	50.8	12.4	43.6	5.2	100.0
Emerald dove	1	2	Iridescent	212,496,461	96.0	94.1	86.0	72.7	13.2	63.2	3.6	100.0
Emerald dove	1	2	Non-iridescent	87,166,635	96.1	93.8	82.4	69.2	15.4	58.2	4.2	99.6
Mallard	1	3	Iridescent	132,157,734	97.4	89.9	88.6	77.7	18.1	64.9	5.2	99.7
Mallard	1	3	Non-iridescent	119,568,782	97.2	90.5	88.8	76.8	16.1	67.2	6.4	99.7
Mallard	2	4	Iridescent	96,545,734	96.3	90.7	89.7	78.5	21.8	62.6	5.8	99.8
Mallard	2	4	Non-iridescent	104,256,954	95.8	90.5	89.6	78.2	23.0	61.1	5.7	99.8

[a]Fraction of reads with barcodes that match the whitelist after barcode correction
[b]Fraction of reads that mapped to the genome
[c]Fraction of reads that mapped uniquely to the genome
[d]Fraction of reads that mapped to a unique gene in the transcriptome
[e]Fraction of reads that mapped uniquely to an intronic region of the genome
[f]Fraction of reads that mapped uniquely to an exonic region of the genome
[g]Fraction of reads confidently mapped to the transcriptome on the opposite strand of their annotated gene
[h]Fraction of reads with UMI sequences that do not contain Ns and that are not homopolymers

Table S11. Single-cell RNA-sequencing tissue composition and cell proportion differences between iridescent and non-iridescent feather halves in the common emerald dove and mallard.

	Emerald dove						
	Iridescent color		**Non-iridescent color**		**Two Sample t-test**		
	Replicate 1	Replicate 2	Replicate 1	Replicate 2	*t*	*df*	*P*
Keratinocytes	1311	1247	881	822	-0.159	1.849	0.890
Melanocytes 1	545	641	125	119	12.955	1.288	**0.025**
Melanocytes 2	227	236	19	84	3.566	1.408	0.115
Endothelial cells	236	413	228	338	-1.762	1.506	0.259
Mesenchymal 1	258	545	329	584	-1.975	1.998	0.187
Mesenchymal 2	35	68	86	87	-1.337	1.343	0.364
Leukocytes 1	94	130	33	116	0.123	1.025	0.922
Leukocytes 2	54	84	20	81	-0.123	1.095	0.921
Leukocytes 3	15	23	16	23	-4.148	1.848	0.061
Erythrocytes	7	6	15	3	-0.770	1.022	0.580
Neural-crest derived cells	5	10	3	11	-0.547	1.261	0.666
All	2787	3403	1755	2268			

	Mallard						
	Iridescent color		**Non-iridescent color**		**Two Sample t-test**		
	Replicate 1	Replicate 2	Replicate 1	Replicate 2	*t*	*df*	*P*
Keratinocytes	2797	4047	4228	3240	-3.262	1.784	0.096
Mesenchymal 1	1899	1425	413	639	2.182	1.339	0.220
Melanocytes 1	74	601	94	86	0.874	1.000	0.543
Melanocytes 2	74	176	38	46	1.802	1.107	0.304
Leukocytes	147	143	43	158	0.200	1.119	0.871
Endothelial cells	86	80	105	135	-2.133	1.402	0.218
Mesenchymal 2	42	29	33	46	-0.842	1.996	0.489
Erythrocytes	12	26	17	12	0.085	1.322	0.943
All	5131	6527	4971	4362			

Figure S1. Phenotypic variation in male peafowl (peacocks, left) and female peafowl (peahens, right) across the mutations examined in this study. Each mutant phenotype differs by a single mutational step from the wild-type.

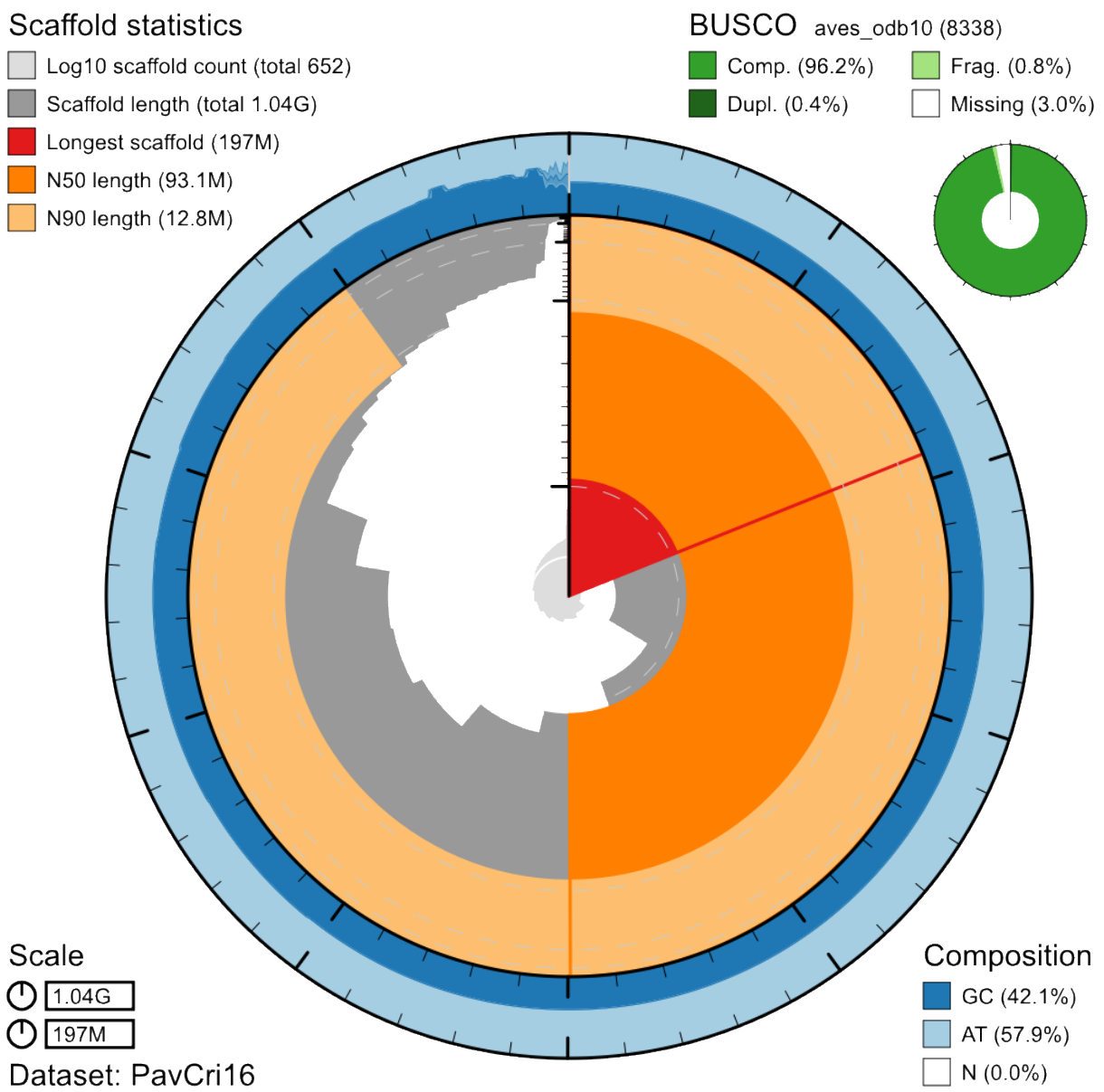

Figure S2. Snail plot summary of assembly statistics for the Indian peafowl (*Pavo cristatus*) reference genome (*PavCri17*). This plot provides an overview of the *PavCri17* genome assembly statistics (see also **table S1**). The main circular plot is divided into 1,000 size-ordered bins, each representing 0.1% of the 1,036,683,990 bp assembly. The distribution of sequence lengths is depicted in dark gray, with the plot radius scaled to the longest scaffold (196,737,001 bp, shown in red). Orange and pale-orange arcs indicate the N50 (93,074,296 bp) and N90 (12,795,000 bp) sequence lengths, respectively. The pale gray spiral represents the cumulative sequence count on a logarithmic scale, with white dashed lines marking increasing orders of magnitude. The outer blue and pale-blue regions show GC, AT, and N content distributions in the same bins as the inner plot. A summary of complete, fragmented, duplicated, and missing BUSCO genes from the *aves_odb10* set is provided in the top right corner.

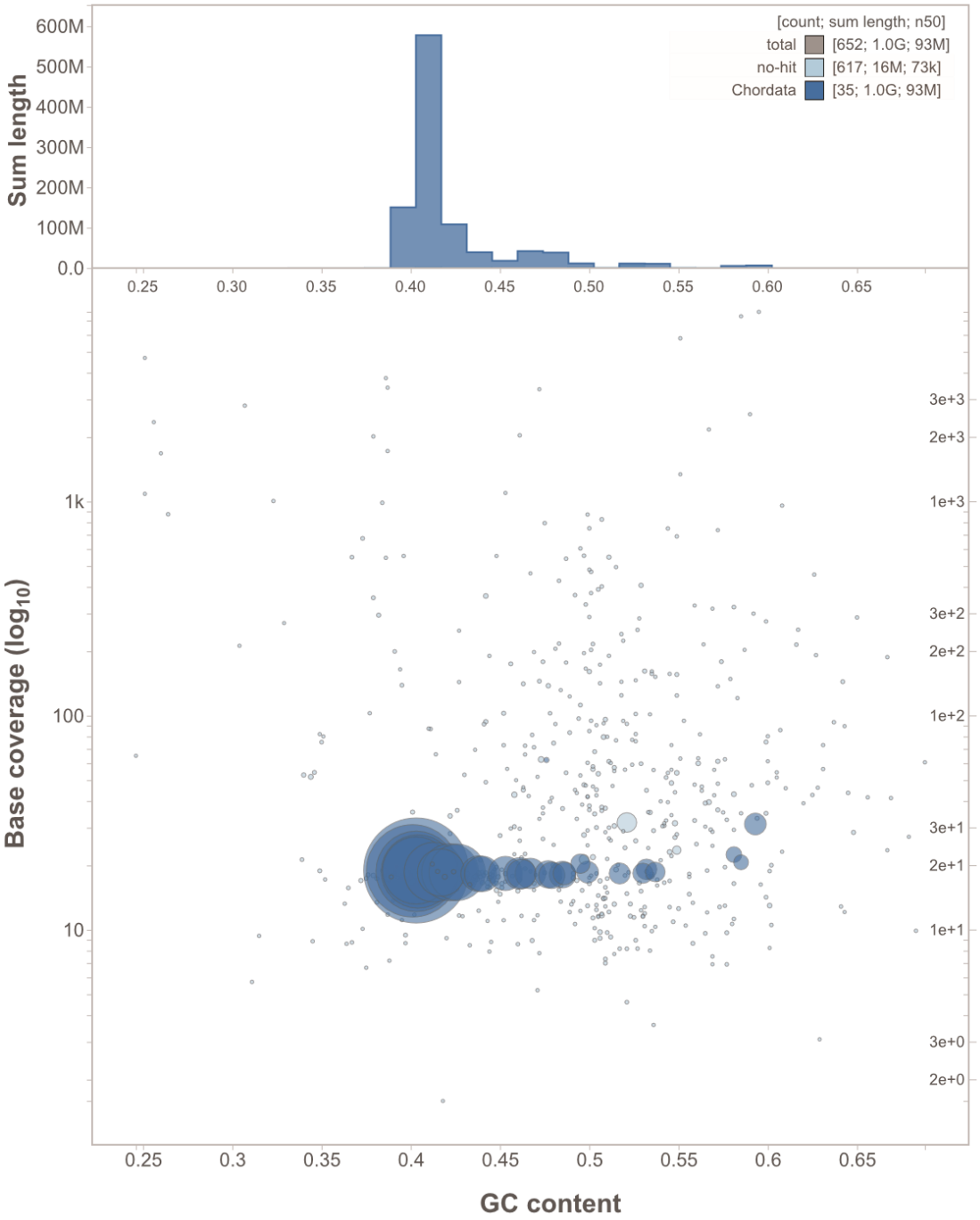

Figure S3. Blob Plot. The plot displays base coverage (Illumina reads; *y*-axis) versus GC content (*x*-axis) for scaffolds in the Indian peafowl (*Pavo cristatus*) reference genome (*PavCri17*). Circle sizes correspond to scaffold lengths. Marginal histograms illustrate the cumulative sequence length distribution along each axis. All scaffolds were assigned to Chordata (top-right corner), and coverage remained consistent across major scaffolds, providing no evidence of significant contamination from other taxa.

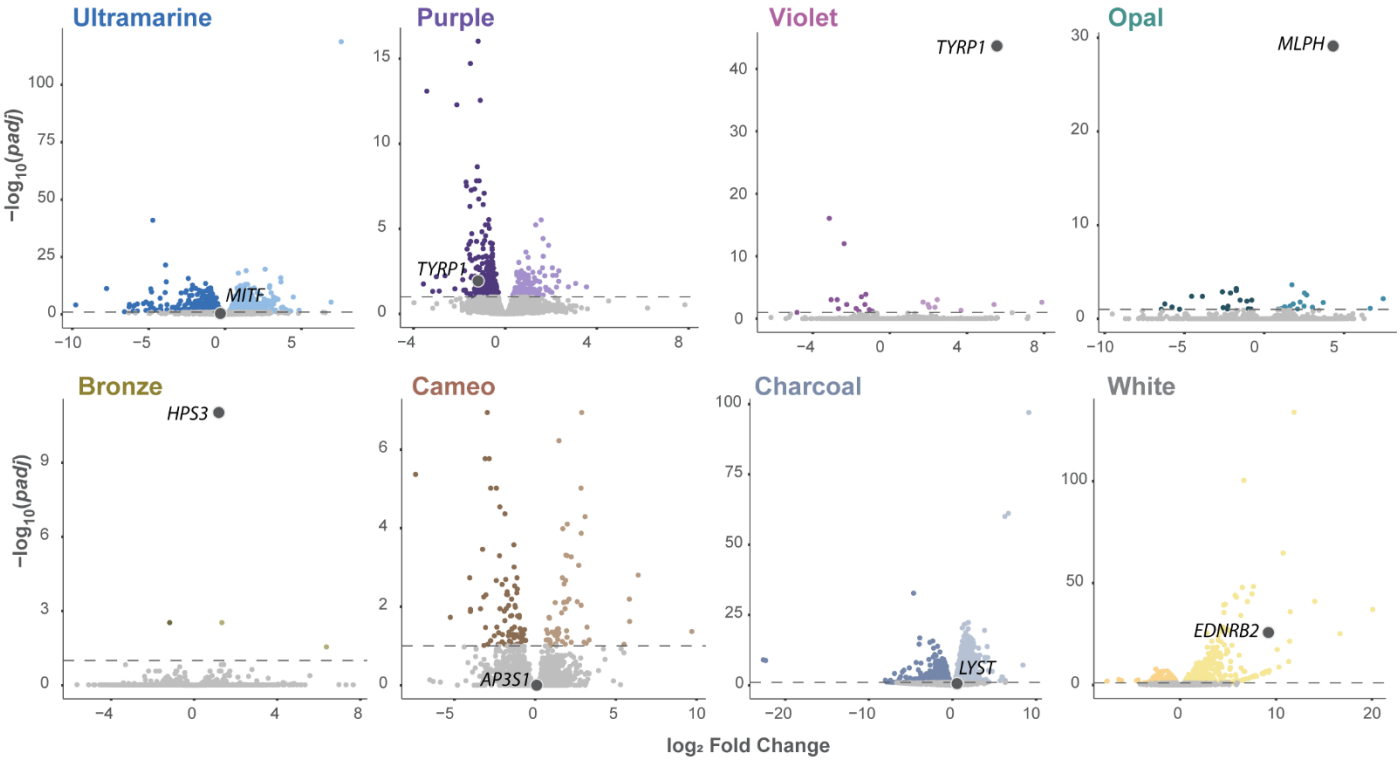

Figure S4. Volcano plots of RNA sequencing results. Each circle represents one gene, and light and dark colors indicate significant under- and over-expression in the mutant, respectively. Genes highlighted and labeled in dark gray circles represent those for which a genomic association was found.

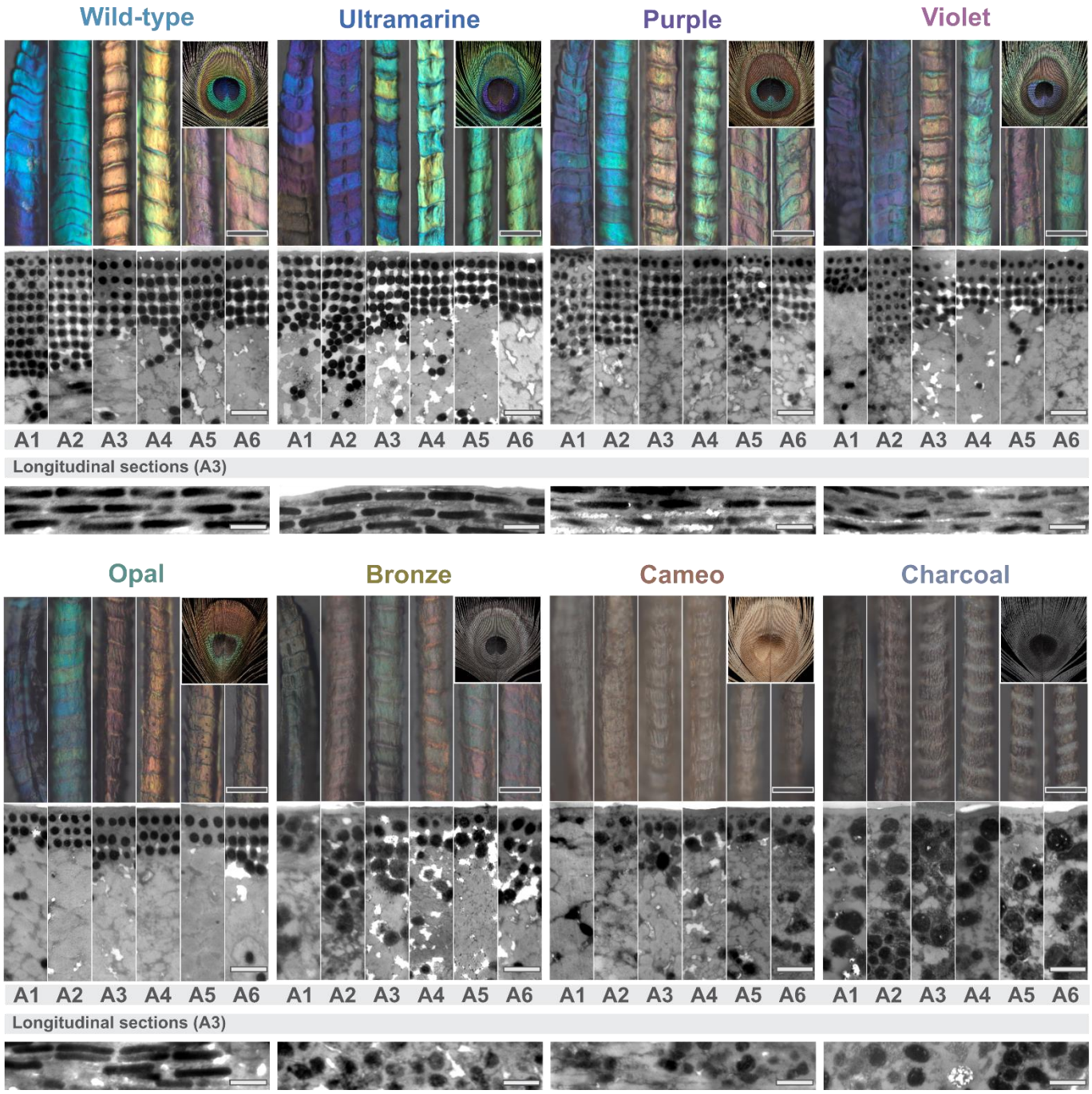

Figure S5. Optical and transmission electron microscopy (TEM) images of feather barbules. Transversal and longitudinal cuts are shown for each of the six areas of the eyespot (A1–A6) in wild-type and seven mutants. For each mutant and area, we show a picture of the feather barbule on top and TEM below, with an inset of the macroscopic appearance of the eyespot in the top right corner. Across the bottom of each set, we show a TEM longitudinal section of A3 to exemplify melanosome shape as rod-like versus sphere-like. Gray and white scales represent 50 µm (full barbule) and 500 nm (barbule sections), respectively.

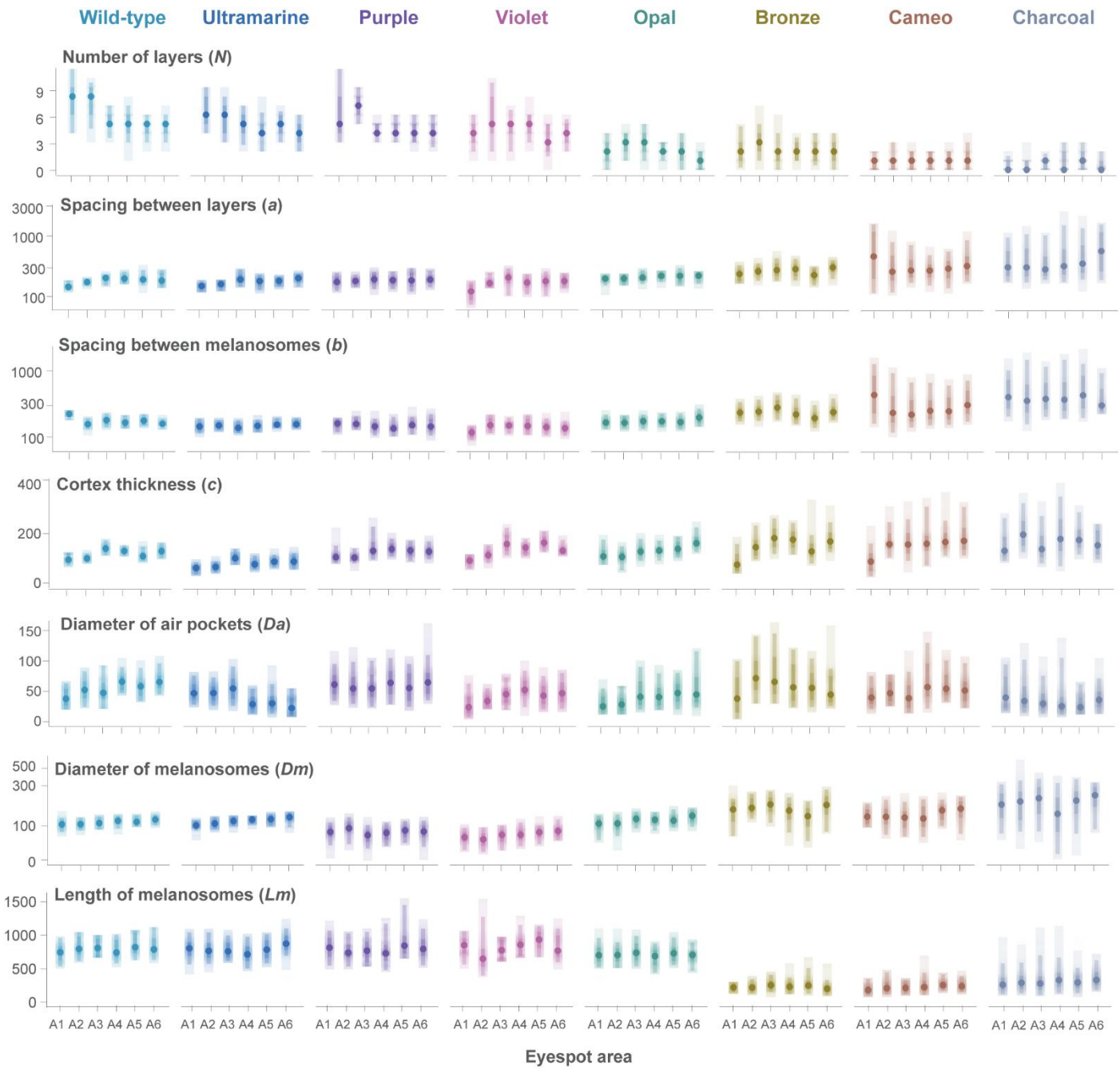

Figure S6. TEM measurements of photonic lattice parameters. Gradient plots of variation in lattice parameters across A1–A6 regions for wild-type and peafowl mutants: number of melanosome layers (*N*), spacing between layers (*a*), spacing between melanosomes within layer (*b*), cortex thickness (*c*), diameter of air pockets (*Da*), diameter of melanosomes (*Dm*), and length of melanosomes (*Lm*). Each circle represents an average measurement for a specific region, narrow bars represent quantile intervals at the 80% and 95% levels, and the wider bar represents the minimum–maximum range for each area. Spacing measures are in nm, and a log scale is used for clearer visualization of the variation in *a*, *b,* and *Dm*.

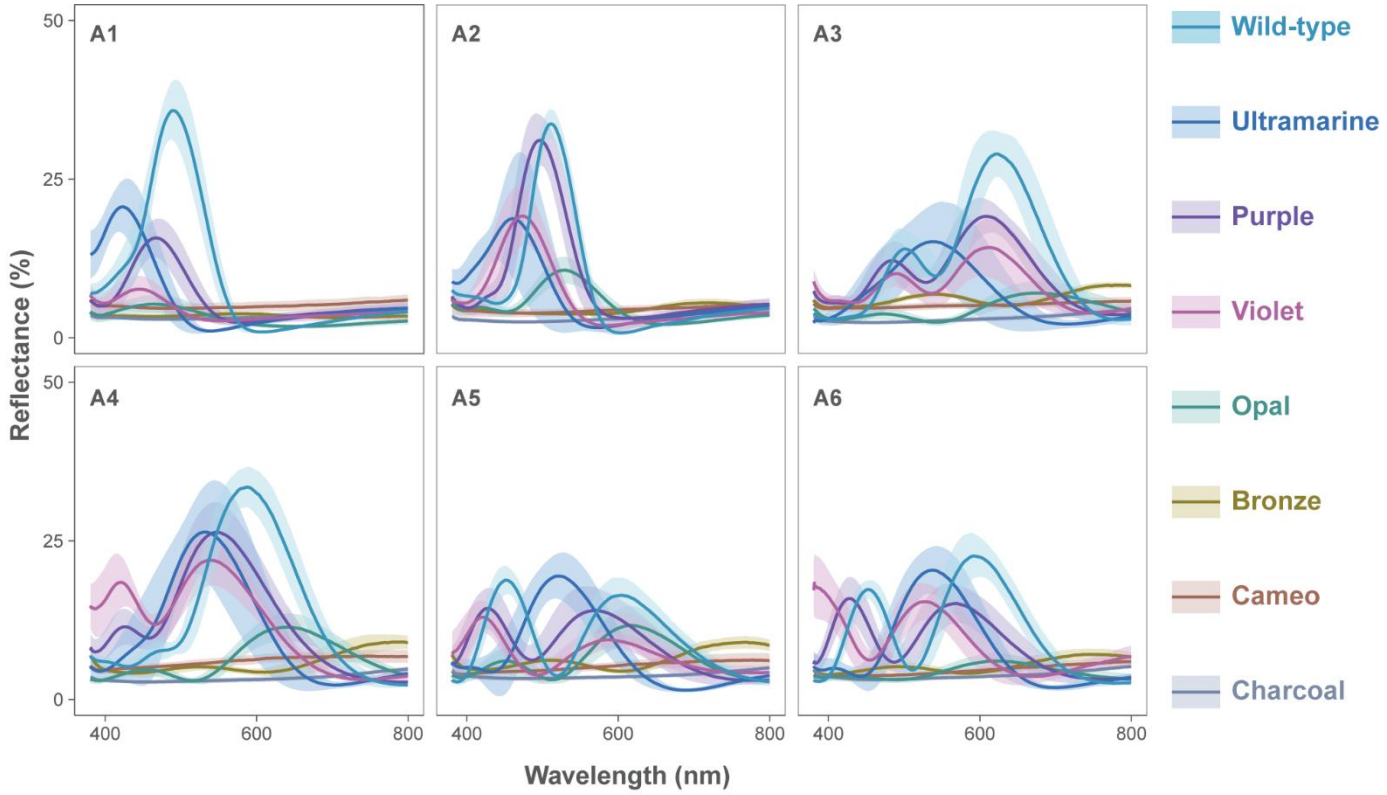

Figure S7. Microscopic reflectance spectra at 90º angle across all eyespot areas (A1–A6) for all mutants. For each mutant in each area, the solid line indicates the average measured reflectance across wavelengths, and the shaded area indicates the corresponding standard deviation.

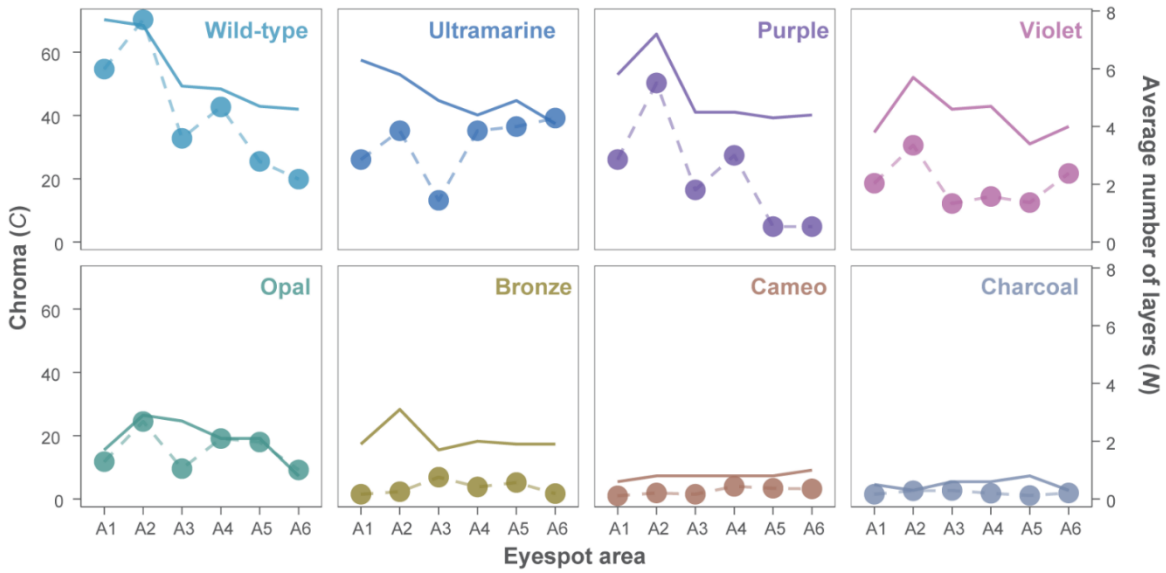

Figure S8. Chroma intensity (*C*) across mutants and eyespot areas in relation to the average number of melanosome layers (*N*). Chroma values (measured in Munsell chroma units) are shown as circles, while the average number of layers per area is represented by solid lines (scale on the right axis). This figure shows the high correlation of chroma intensity with the number of layers (83.9%, $t = 5.7$, $df = 94$, $P = 1.3 \times 10^{-7}$).

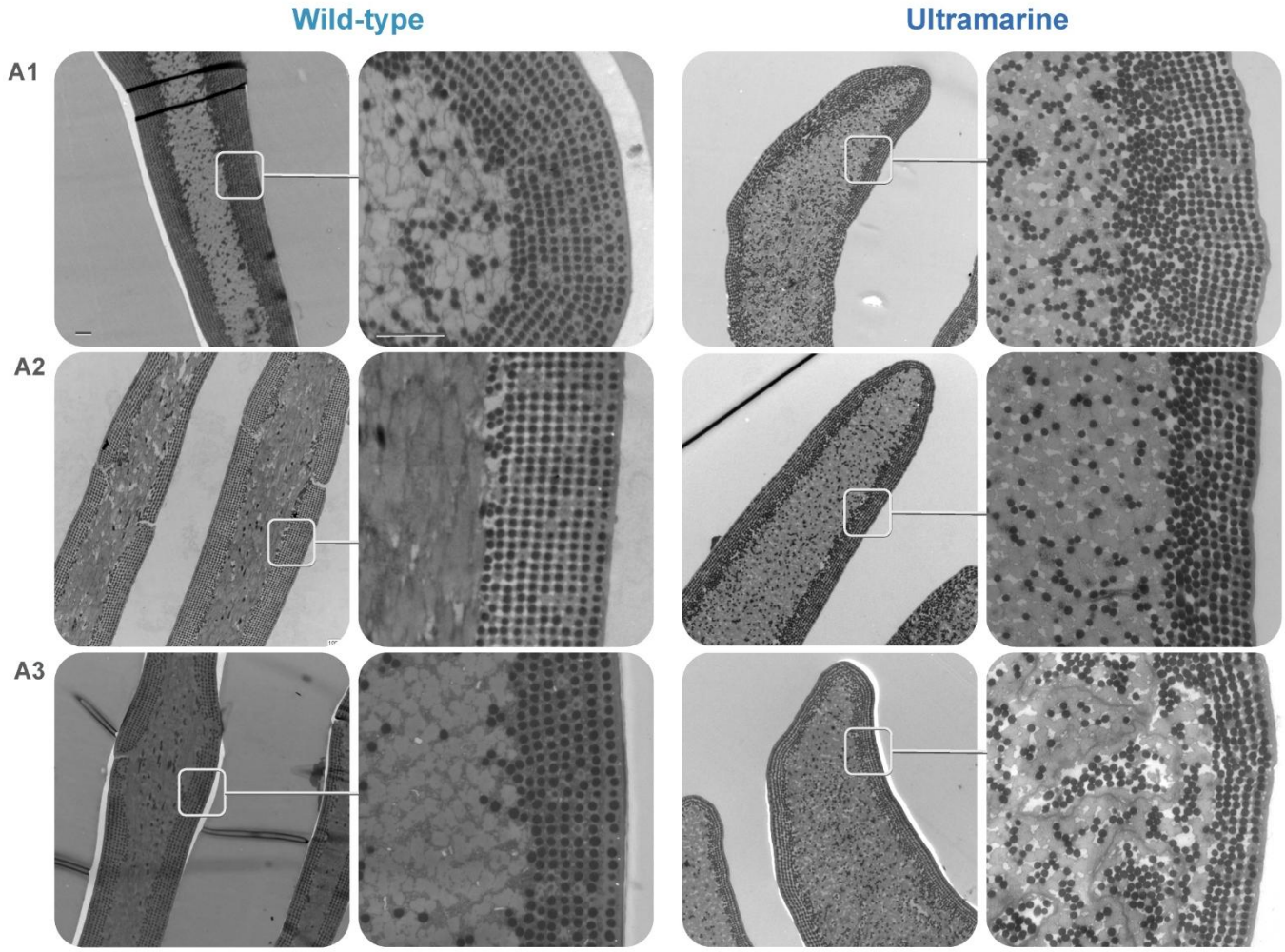

Figure S9. Barbule ultrastructure comparison of wild-type and *ultramarine* using transmission electron microscopy (TEM). Images in two scales are presented for each phenotype across the most distinct eyespot areas (A1–A3): a zoomed-out on the left (scale bar 5 µm) and a zoomed-in on the right (scale bar 1 µm).

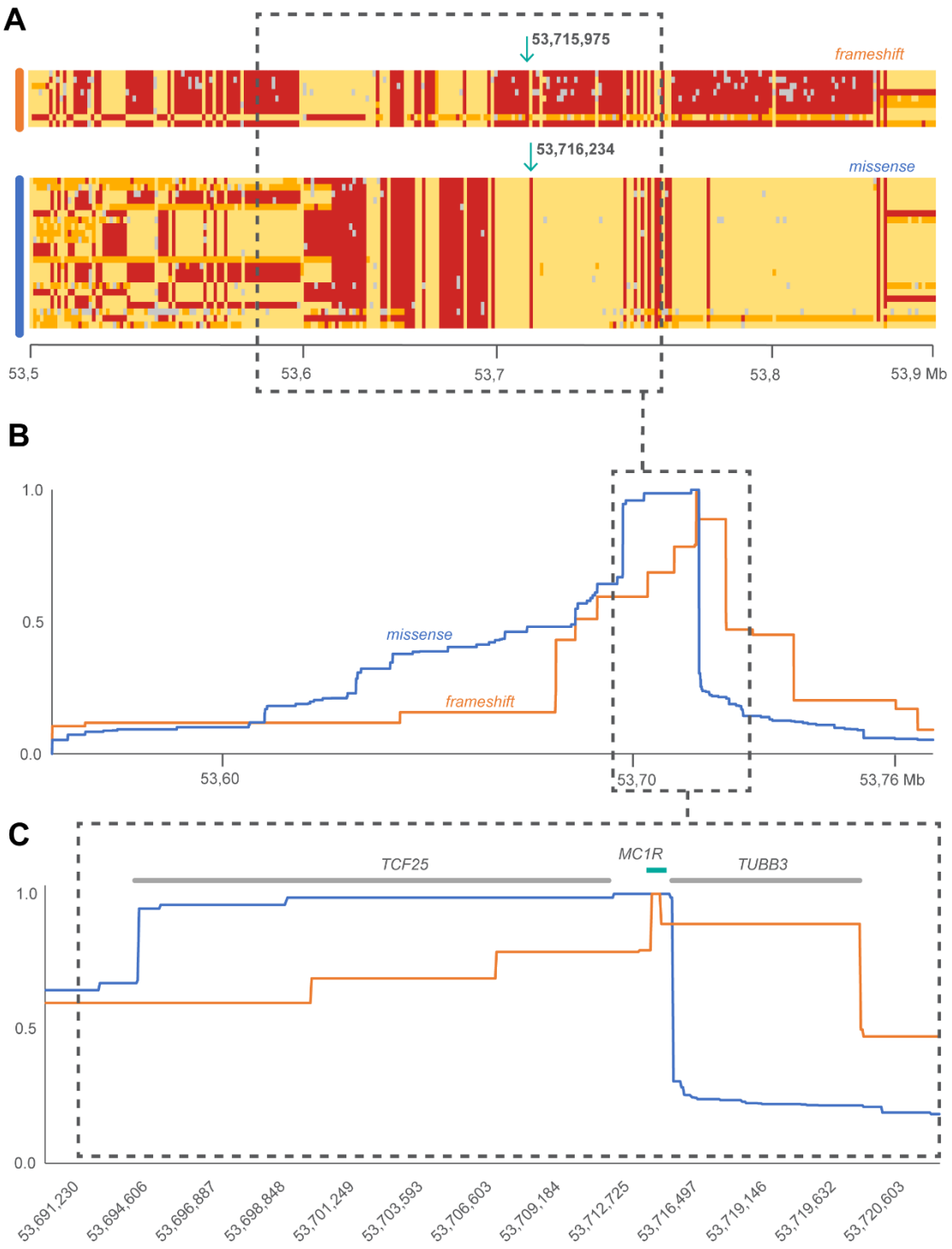

Figure S10. Identical-by-descent (IBD) analysis of the Black-shoulder mutations. (A) Black-shoulder haplotype structure over ~500 kb around the topmost significant variants of the genome-wide association analyses, with the relative gene position and arrows indicating the position of the two mutations [frameshift (orange): chr6:53,715,975 CA>C; missense (blue): chr6:53,716,234 T>C] (**table S2**). Each line represents a haplotype and each column a variable position with a thinning of 1,000 bp between positions. Positions containing the reference allele are colored in yellow, those containing the alternative allele are colored in red, heterozygous positions are colored in orange, and missing genotypes are colored in gray. **(B)** Extended haplotype homozygosity (EHH) within a genomic interval centered on the most significantly associated variants with the Black-shoulder color phenotype. **(C)** Zoom into the ~40kb region highlighted in **B** with a dashed black box, indicating the relative position of the *MC1R* gene (green) and the two neighboring genes (gray) in the interval. The IBD region for both protein-coding mutations is small and overlaps the *MC1R* gene.

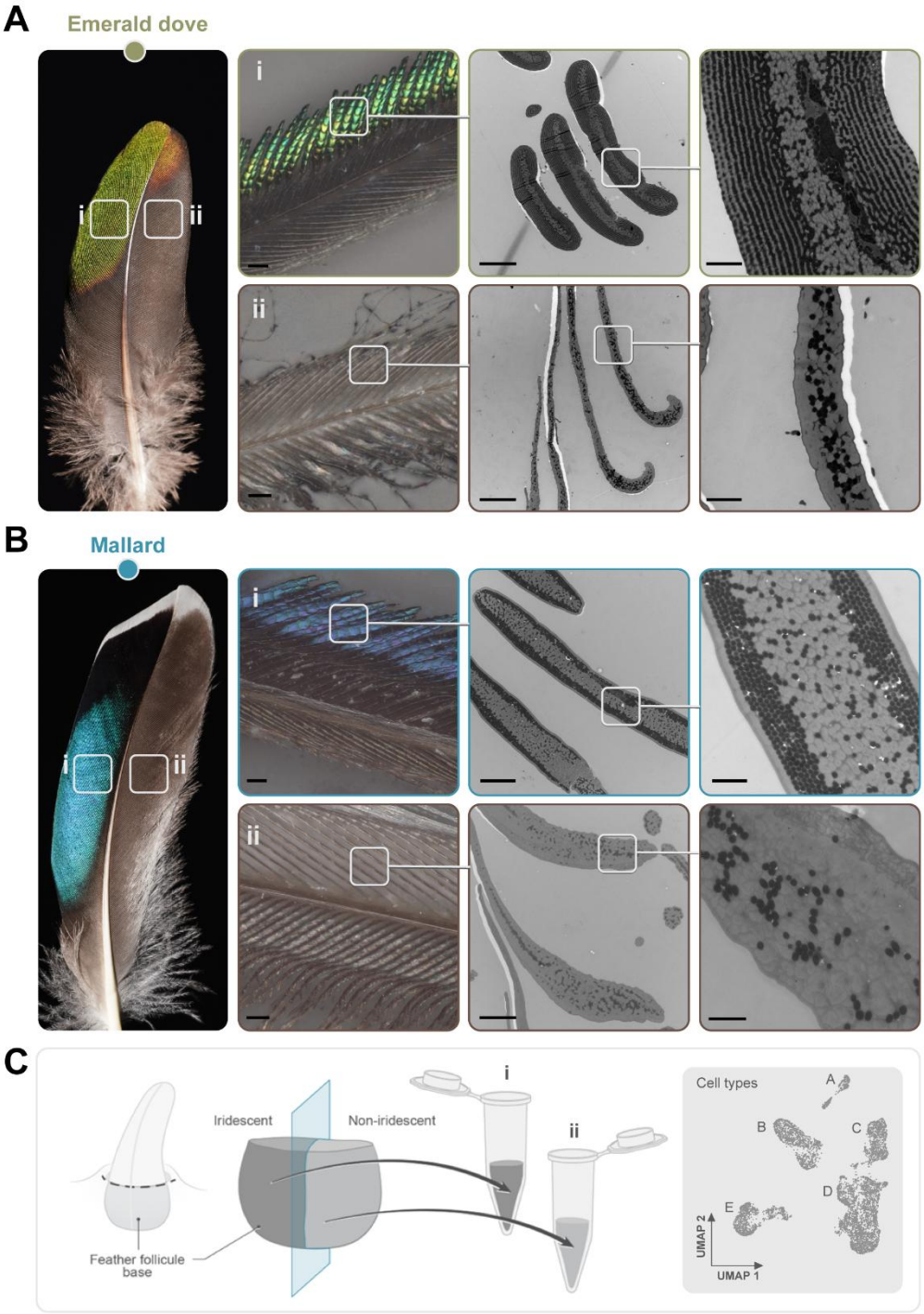

Figure S11. Transmission electron microscopy (TEM) of iridescent and non-iridescent barbules in asymmetric feathers. In both the emerald dove (*Chalcophaps indica*) (**A**) and the mallard duck (*Anas platyrhynchos*) (**B**), some feathers show marked coloration asymmetry, with iridescent barbules (i) developing on one side and non-iridescent barbules (ii) on the other. Left to right: optical microscopy images of individual barbs (scale bars: 50 µm) and TEM images of barbules (scale bars: 5 µm and 1 µm). Cross-sections at multiple magnifications reveal distinct barbule morphologies and melanosome organization between color types. **(C)** Schematic of the sampling strategy for the single-cell RNA-seq analyses: individual asymmetric feathers were plucked during growth at the time of iridescent color formation, the basal portion of the follicle was isolated, and each half of the feather producing iridescent barbules (i) or non-iridescent barbules (ii) was processed separately for cell dissociation and single-cell RNA-seq analyses (see Methods). The same methodology was applied for both species on two individual feathers (n = 4 libraries per species).

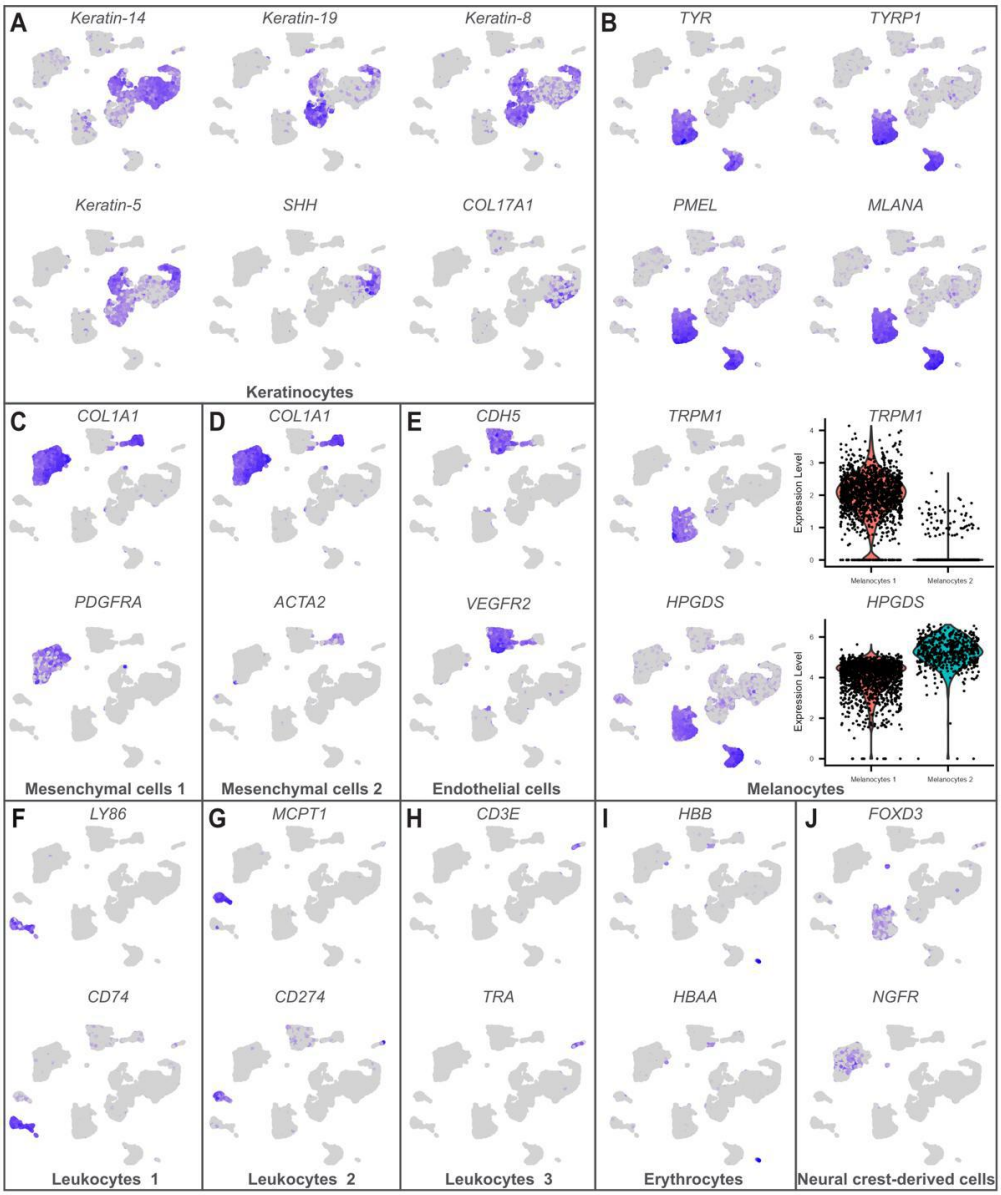

Figure S12. **Expression heat maps of selected genes supporting the single-cell RNA sequencing (scRNA-seq) cluster annotation for the common emerald dove**. UMAP projections based on 10,213 cells (i.e., four scRNA-seq libraries merged). **(A)** Keratinocytes: *Keratin-14* and *Keratin*-19 (type I), *Keratin-8* and *Keratin*-5 (type II), *SHH* (marker for marginal plate cells), *COL17A1* (marker for basal keratinocytes); **(B)** Melanocytes: *TYR* (required for the conversion of tyrosine to melanin), *TYRP1* (involved in eumelanin synthesis and pigment stabilization), *PMEL* (essential for melanosome formation and melanin deposition), *MLANA* (involved in melanosome biogenesis), *TRPM1* (involved in melanocyte signaling; marker for Melanocytes 1), *HPGDS* (glutathione S-transferase; enriched in Melanocytes 2; see Methods). The violin plots reports log-normalized expression for Melanocytes 1 and 2; **(C)** Mesenchymal cells 1: *COL1A1* (fibroblast marker), *PDGFRA* (fibroblast surface receptor for platelet-derived growth factors); **(D)** Mesenchymal cells 2: *COL1A1* (fibroblast marker), *ACTA2* (myofibroblast marker); **(E)** Endothelial cells: *CDH5* (plays a role in endothelial adherens junctions), *VEGFR2* (receptors for endothelial cell growth factor); **(F)** Leukocytes 1: *LY86* (lymphocyte antigen), *CD74* (regulates antigen presentation for immune response); **(G)** Leukocytes 2: *MCPT1* (mast cell–specific protease), *CD274* (ligand inhibiting T-cell activation, expressed in T cells and B cells); **(H)** Leukocytes 2: *CD3E* (part of the TCR-CD3 complex present on T-lymphocytes), *TRA* (involved in T cell activation); **(I)** Erythrocytes: *HBB* (hemoglobin subunit beta), *HBAA* (hemoglobin subunit alpha 1); **(J)** Neural crest-derived cells: *FOX3D* (promotes the development of neural crest cells from neural tube progenitors), *NGFR* (regulates neural crest-derived cell proliferation, survival, and differentiation). Log-normalized expression scale ranges from gray (no expression) to dark blue (maximum expression).

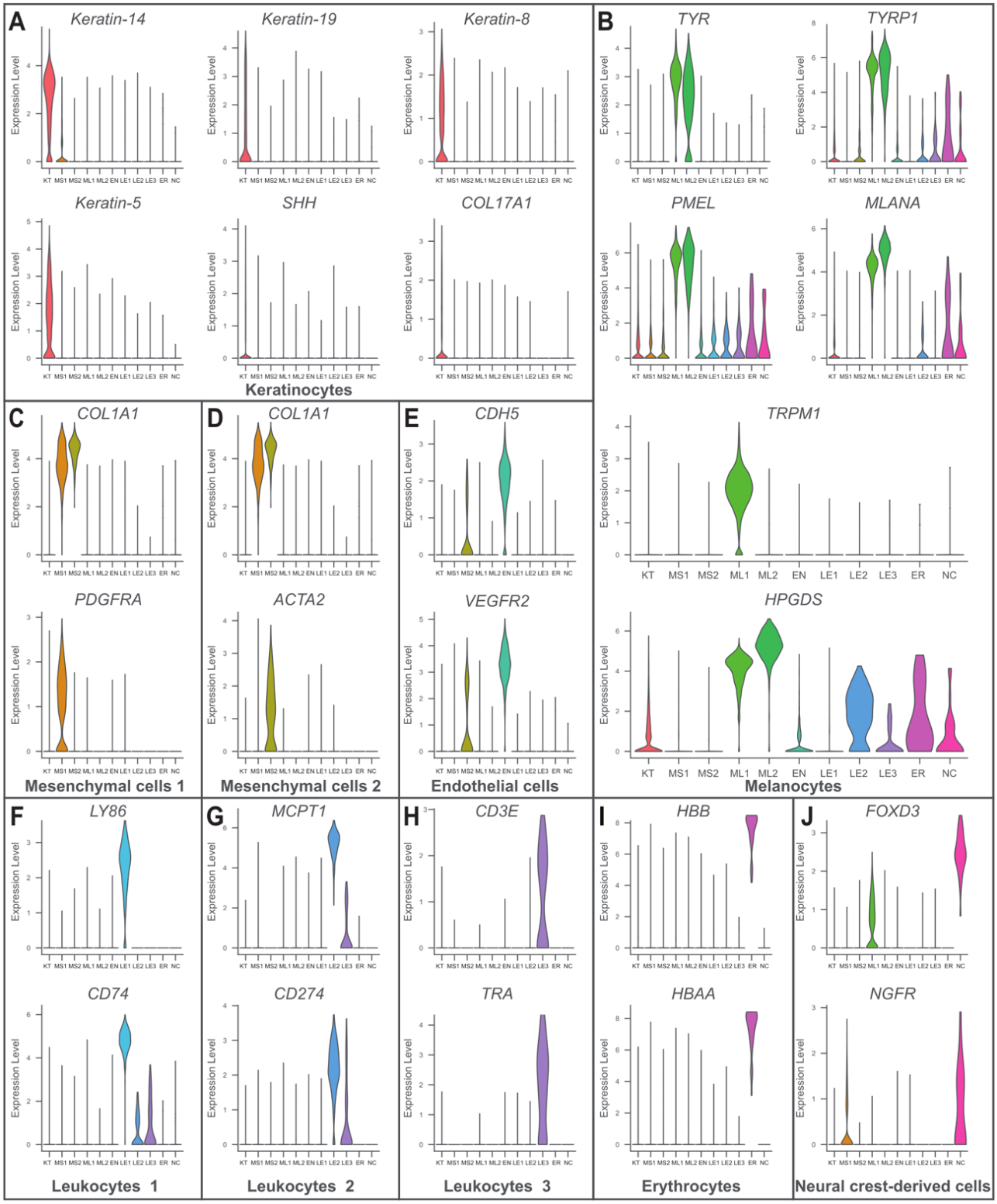

Figure S13. **Expression violin plots of selected genes supporting the single-cell RNA sequencing (scRNA-seq) cluster annotation for the common emerald dove**. Plots based on 10,213 cells (i.e., four scRNA-seq libraries merged). **(A-J)** The marker genes are the same as in **fig. S12**. KT: Keratinocytes; MS1: Mesenchymal cells 1; MS2: Mesenchymal cells 2; ML1: Melanocytes 1; ML2: Melanocytes 2; EN: Endothelial cells; LE1: Leukocytes 1; LE2: Leukocytes 2; LE3: Leukocytes; ER: Erythrocytes; NC: Neural crest-derived cells. The distribution of the expression levels for each gene (log-normalized) across clusters is reported.

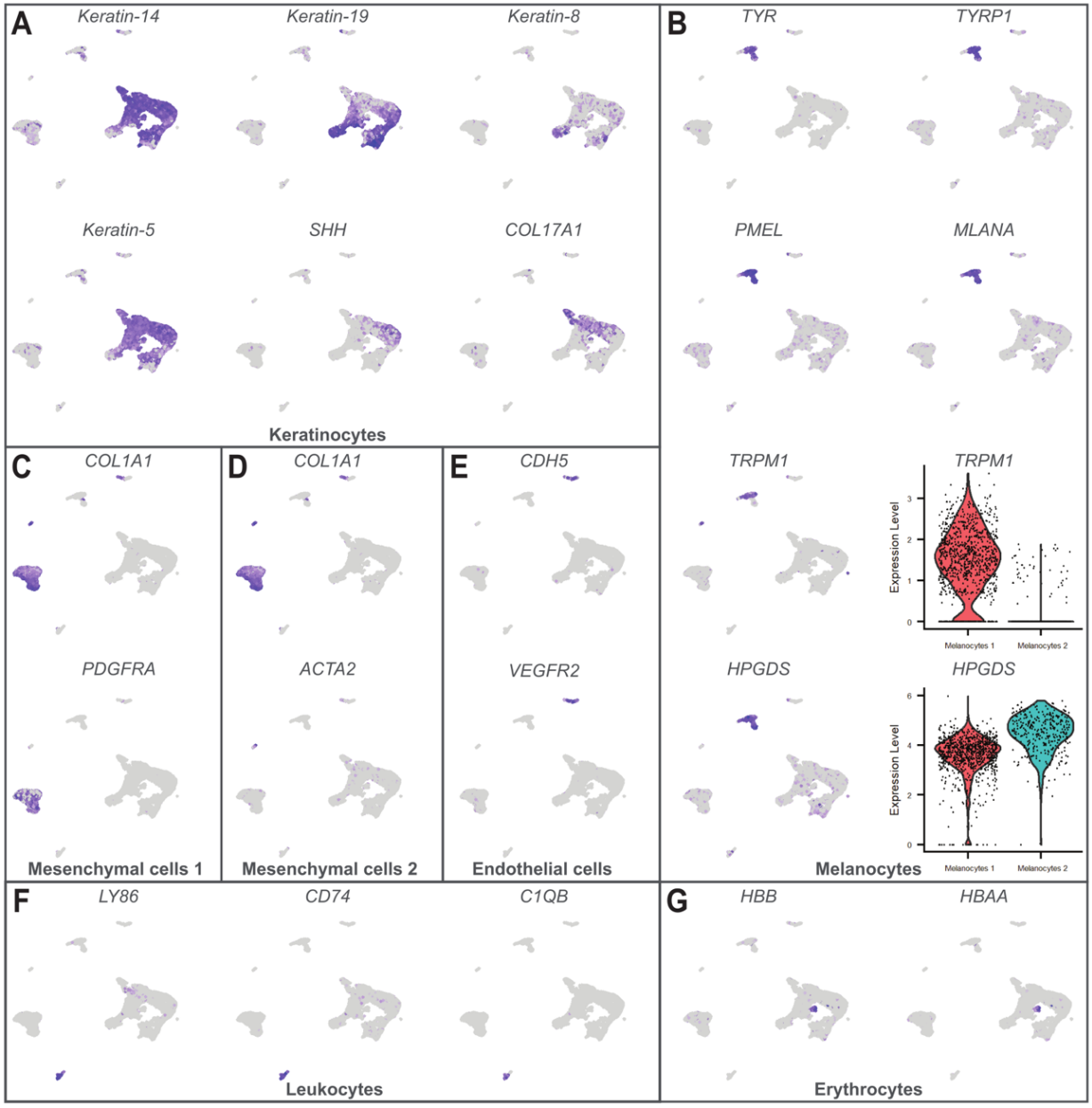

Figure S14. **Expression heat maps of selected genes supporting the single-cell RNA sequencing (scRNA-seq) cluster annotation for the mallard duck**. UMAP projections based on 20,991 cells (i.e., four scRNA-seq libraries merged). **(A)** Keratinocytes: *Keratin-14* and *Keratin*-19 (type I), *Keratin-8* and *Keratin*-5 (type II), *SHH* (marker for marginal plate cells), *COL17A1* (marker for basal keratinocytes); **(B)** Melanocytes: *TYR* (required for the conversion of tyrosine to melanin), *TYRP1* (involved in eumelanin synthesis and pigment stabilization), *PMEL* (essential for melanosome formation and melanin deposition), *MLANA* (involved in melanosome biogenesis), *TRPM1* (involved in melanocyte signaling; marker for Melanocytes 1), *HPGDS* (glutathione S-transferase; enriched in Melanocytes 2; see Methods). The violin plots reports log-normalized expression for Melanocytes 1 and 2; **(C)** Mesenchymal cells 1: *COL1A1* (fibroblast marker), *PDGFRA* (fibroblast surface receptor for platelet-derived growth factors); **(D)** Mesenchymal cells 2: *COL1A1* (fibroblast marker), *ACTA2* (myofibroblast marker); **(E)** Endothelial cells: *CDH5* (plays a role in endothelial adherens junctions), *VEGFR2* (receptors for endothelial cell growth factor); **(F)** Leukocytes 1: *LY86* (lymphocyte antigen), *CD74* (regulates antigen presentation for immune response), *C1QB* (component of the serum complement system); **(G)** Erythrocytes: *HBB* (hemoglobin subunit beta), *HBAA* (hemoglobin subunit alpha 1). Log-normalized expression scale ranges from gray (no expression) to dark blue (maximum expression).

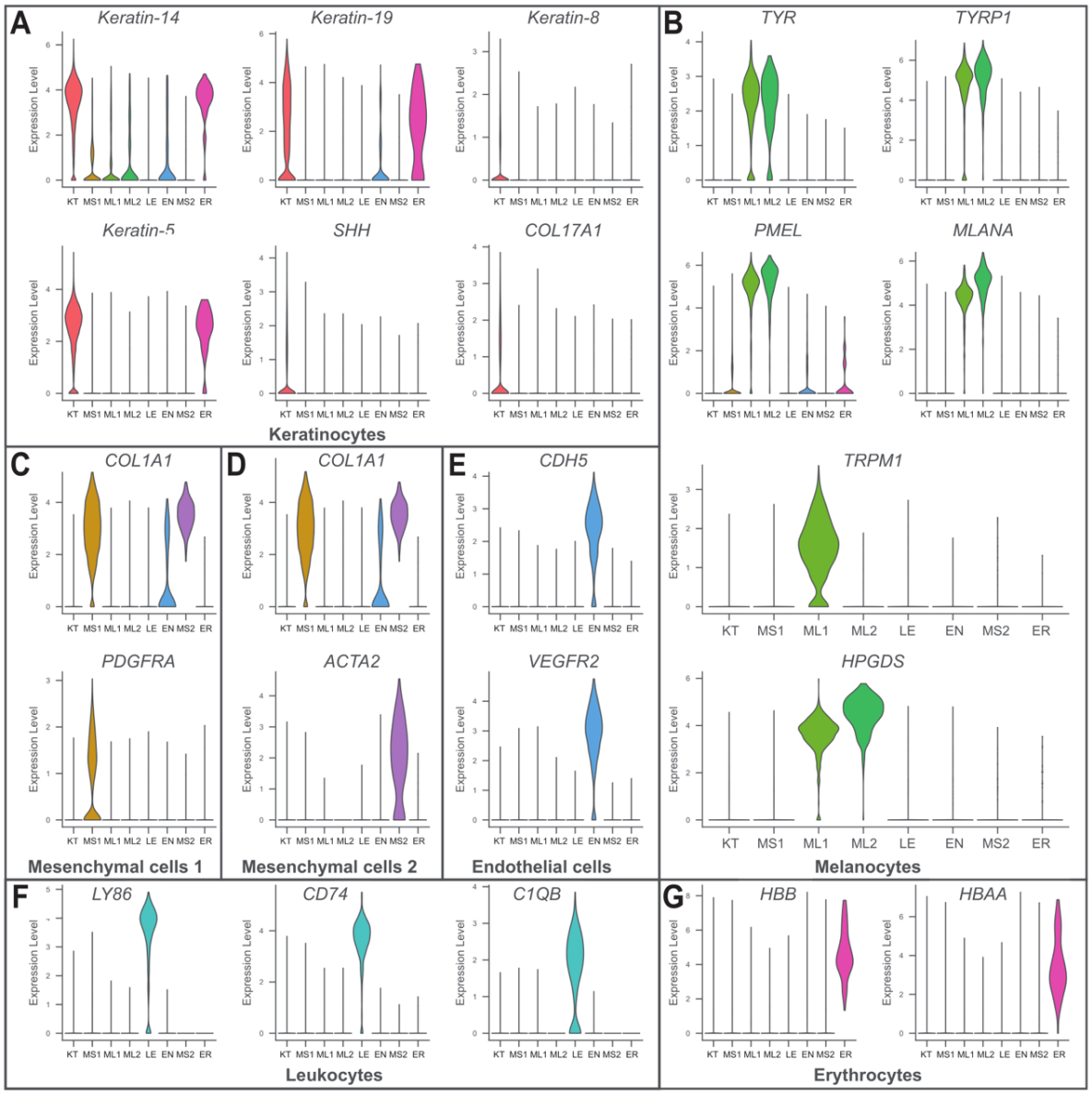

Figure S15. **Expression violin plots of selected genes supporting the single-cell RNA sequencing (scRNA-seq) cluster annotation for the mallard duck**. Plots based on 20,991 cells (i.e., four scRNA-seq libraries merged). **(A-G)** The marker genes are the same as in **fig. S14**. KT: Keratinocytes; MS1: Mesenchymal cells 1; MS2: Mesenchymal cells 2; ML1: Melanocytes 1; ML2: Melanocytes 2; EN: Endothelial cells; LE: Leukocytes; ER: Erythrocytes. The distribution of the expression levels for each gene (log-normalized) across clusters is reported.

Figure S16. Gene ontology (GO) enrichment analyses of melanocyte differentially expressed genes (DEGs) between iridescent and non-iridescent barbules (considering the merged populations of melanocytes 1 and 2). (A) Common emerald dove. **(B)** Mallard duck. Enriched GO terms with at least two represented genes and with *P*-value ≤ 0.1 (Fisher's exact test) are reported (see **Data S5 and S6** for further details). The bars represent the number of genes within each GO term: cellular component (orange), biological process (blue), and molecular function (green).

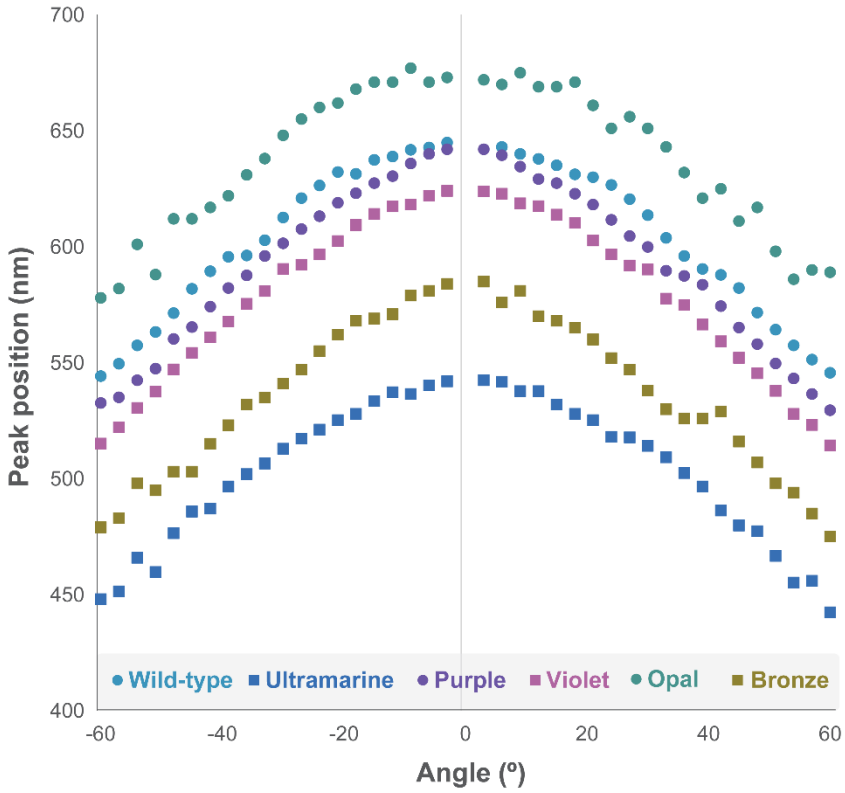

Figure S17. Angle-dependent normalization comparison. Measurement of the angle-dependent reflectance peak wavelength for area 3 (A3) of the eyespot for mutants exhibiting iridescence across incidence angles from –60º to 60º in 3º increments (excluding 0º). Cameo and Charcoal were excluded due to the absence of reflectance. Peak height was estimated from raw reflectance measures normalized with 200-point smoothing. This figure shows that peak positions are symmetrical between positive and negative angle measurements, allowing inferences using only one group of values.

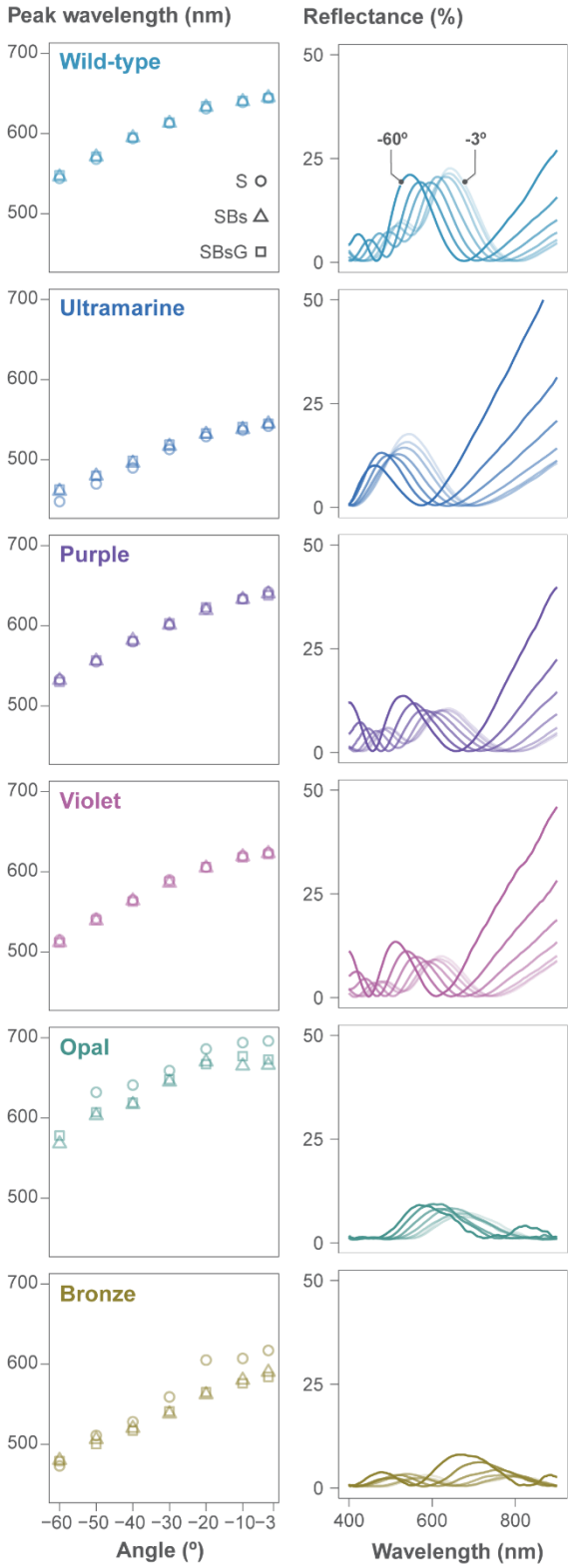

Figure S18. Normalized angle-dependent reflectance measurements for area 3 (A3) of the eyespot. Panels on the left represent peak wavelength for mutants exhibiting iridescence across incidence angles from -60º to -3º for three normalization strategies: 200-point smoothing (S, circle); 200-point smoothing and baseline (spline) subtraction (SBs, triangle); and 200-point smoothing and baseline subtraction with Gaussian fit (SBsG, square). Cameo and Charcoal were excluded due to the absence of reflectance. Panels on the right show the measurement of the angle-dependent reflectance considering SBsG normalization with increasing transparency from -60 to -3º. This figure shows that data transformations do not substantially affect the peak wavelength identified across multiangle measurements.